HOKKAIDO UNIVERSITY

Title	Near-Field Coseismic Ionospheric Disturbances of Earthquakes In and Around Indonesia
Author(s)	Mokhamad Nur, Cahyadi
Degree Grantor	北海道大学
Degree Name	博士(理学)
Dissertation Number	甲第11379号
Issue Date	2014-03-25
DOI	https://doi.org/10.14943/doctoral.k11379
Doc URL	https://hdl.handle.net/2115/55622
Type	doctoral thesis
File Information	Mokhamad_Nur_Cahyadi.pdf

Hokkaido University Collection of Scholarly and Academic Papers : HUSCAP

Near-Field Coseismic Ionospheric Disturbances of Earthquakes In and Around Indonesia

By

Mokhamad Nur Cahyadi

Submitted for The Degree of Doctor of Philosophy

Dept. Natural History Sciences,

Graduate School of Science, Hokkaido University

February, 2014

Table of content

Abstract ..... **iv**

Acknowledgment ..... **vi**

Chapter 1 Introduction **1**

1.1 Global Positioning System for Monitoring Total Electron Content (TEC) 1

1.2 Previous research in Ionospheric Disturbances 2

1.2.1 Why Near Field CID ? 2

1.2.2 CID of the Indonesian Earthquakes 3

1.3 Outline of the Study 6

Chapter 2 Data Processing **8**

2.1 GPS Data 8

2.2 Coseismic Ionospheric Disturbances (CID) 10

2.3 Long-term Preseismic Ionospheric Disturbances 13

2.4 Sub-Ionospheric Point (SIP) and Ionospheric Pierce Point (IPP) 14

2.5 Calculating GIM 15

2.6 Calculating the Propagation Speed of the Disturbances 16

2.7 Black Tukey Method 17

2.8 DST Index 17

2.9 Earthquake Mechanism 18

2.10 Okada's (1992) Model 19

Chapter 3 Ionospheric disturbances of the 2007 Bengkulu and the 2005 Nias earthquakes, Sumatra, observed with a regional GPS network **20**

3.1 Introduction 21

3.2 TEC Changes in the 2007 Bengkulu Earthquake 23

3.2.1CID amplitudes and waveforms 23

3.2.2 Propagation speeds 28

3.2.3 Pre-seismic Ionospheric Anomalies 29

3.2.3.1 Long-term anomalies 29

3.2.3.2 Short-term anomalies 33

3.2.3.3 Comparison of short-term preseismic TEC changes with other earthquakes 36

3.2.4 CID of the largest aftershock 42

3.3 TEC changes in the 2005 Nias Earthquake 44

Chapter 4 Coseismic Ionospheric Disturbance of the 2012 North Sumatra Earthquakes, Large Intra-Plate Strike-Slip events **46**

4.1 Introduction 47

4.2 TEC Changes before and after the 2012 North Sumatra Earthquake 48

4.3 Near Field CID of The 2012 North Sumatra Earthquake 51

4.3.1 Coseismic vertical crustal movement 51

4.3.2 Propagation Speed 52

4.3.3 Resonant Oscillations 53

4.3.4 Directivity of CID 55

4.4 Comparison With Other Earthquakes 57

4.4.1 Comparison of short-term preseismic TEC changes with other earthquakes 57

4.4.2 Geometry Problem 59

4.4.3 Earthquake magnitudes and CID amplitudes 64

4.4.5 Preseismic TEC Anomalies 70

Chapter 5 Recommendation and Conclusion **75**

5.1 Conclusion 75

5.1.1 Ionospheric disturbances of the 2007 Bengkulu and the 2005 Nias earthquakes, Sumatra, observed with a regional GPS network 75

5.1.2 Coseismic ionospheric disturbance of the 2012 North Sumatra earthquakes, large intra-plate strike-slip events 77

5.2 Recommendation: Early Warning System for earthquake and tsunami 77

Bibliography **79**

ABSTRACT

Coseismic ionospheric disturbances (CIDs) appear shortly after relatively large earthquakes as a result of ionospheric irregularity caused by various atmospheric waves excited by the earthquakes. Near-field CIDs appearing approximately 10 minutes after earthquakes are caused by acoustic waves generated directly by coseismic vertical movements of the crust or the sea surface, and they propagate as fast as ~1 km/second over the distance of hundreds of kilometres. In this research, I focus near-field CID in and around Indonesia, especially in the 2005 Nias, 2007 Bengkulu, and 2012 North Sumatra earthquakes.

I first studied ionospheric disturbances associated with the two large thrust earthquakes in Sumatra, namely, the 2007 Bengkulu and the 2005 Nias earthquakes, by measuring the total electron contents (TEC) using a regional network of global positioning system (GPS) receivers. We mainly study the CID of the Bengkulu earthquake (M_w 8.5). They appeared 11–16 min after the earthquake and propagated northward as fast as ~0.7 km/s, consistent with the sound speed at the ionospheric F layer. Resonant oscillation of TEC with a frequency of ~5 mHz continued for at least 30 min after the earthquake. The largest aftershock (M_w 7.9) also showed clear CIDs similar to the main shock. A CID propagating with the Rayleigh wave velocity was not observed, possibly because the station distribution did not favor the radiation pattern of the surface waves.

This earthquake, which occurred during a period of quiet geomagnetic activity, also showed clear preseismic TEC anomalies similar to those before the 2011 Tohoku-Oki earthquake. The positive and negative anomalies started 30–60 min before the earthquake to the north and the south of the fault region, respectively. On the other hand, we did not find any long-term TEC anomalies within 4–5 days before the earthquake. Co- and preseismic

ionospheric anomalies of the 2005 Nias earthquake (M_w 8.6) were, however, masked by strong plasma bubble signatures, and we could not even discuss the presence or absence of CIDs and preseismic TEC changes for this earthquake.

I next studied ionospheric responses to the 2012 April 11 M_w8.6 North Sumatra earthquake using the similar approach. This earthquake ruptured the oceanic lithosphere off the Indian Ocean coast of North Sumatra, and is known as the largest strike-slip earthquake ever recorded. CID of a few TEC units propagated northward with a speed of acoustic waves. Resonant atmospheric oscillation with a frequency ~4 mHz have been found as monochromatic oscillation of TEC lasting for an hour after the main shock and the largest aftershock.

I then compared CID amplitudes of 21 earthquakes world-wide with moment magnitudes (M_w) 6.6-9.2. They roughly obeyed a law such that CID amplitude increases by two orders of magnitude for the M_w increase of three. The 2012 North Sumatra earthquakes slightly deviated negatively from the trend possibly reflecting their strike-slip mechanisms, *i.e.* small vertical crustal movements for their magnitudes. We found TEC enhancement starting ~40-50 minutes before the main shock and the largest aftershock similar to those found before earthquakes with M_w of 8.5 or larger, including the 2007 Bengkulu earthquake.

Acknowledgment

In the name of Allah, God, the greatest one,

First of all, I would like to express my gratitude for my supervisor, Professor Kosuke Heki for all support and help. First time when I contacted him around 3 years ago, and this is very good chance for me, can be supervised by him. He supported me very much and guides me in the atmospheric disturbances very well. One of the most important that I feel in his supervising, he gave me many chance to attend conference meeting, so I can interact with many scientist from different countries and subject study. Because of atmospheric study is not my background, I have many question about this topic in the first time, and Professor Heki answer my question with very patience.

I also would like to thank to Prof. Toru Mogi, Prof. Junji Koyama, Prof. Makoto Murakami, Prof. Kiyoshi Yomogida, Prof. Masato Furuya, Dr. Kazunori Yoshizawa and Dr. Yuta Mitsui for their constructive comments. For all of Natural History Science Department Laboratory, many thank for all of your support, also for DIKTI Scholarship program from Indonesian Government, EOS Singapore and Indonesian Institute of Sciences.

My family, father and mother, thank you very much for praying in the night, and also for my wife, many thanks for supporting during my study, then for my children, be ambitious guys

Chapter 1

Introduction

1.1 Global Positioning System for Monitoring Total Electron Content (TEC)

The geodetic observation technology is progressing continuously. In the past, people characterized objects or phenomena on earth by direct observation and measurements. Currently, artificial geodetic satellites are launched and enable us to observe the earth from space. Such space geodetic observation now focuses on lunar and planetary studies, too.

The artificial satellite system for navigation called Global Positioning System (GPS) was launched for the first time originally for military purposes in the early 1980s by the United States Department of Defense. Later on, other countries also launched similar satellite systems e. g. GLONASS by Russia, Galileo by European Union, and Compass (Beidou) by China. These satellite navigation systems are known as Global Navigation Satellite System (GNSS). In this study, I use only GPS.

GPS was launched for navigation, but is useful also for earth observation in general, e.g. crustal deformation and atmospheric studies. Recently, GPS also offered alternative method to analyze temporal and spatial behavior of ionosphere *(Heki and Ping,* 2005*; Kutiev et al,*2007*).* Electromagnetic waves transmitted by GPS satellites are delayed when they travel through ionosphere. This time delay could be used to deduce the variation in

ionosphere, through the quantity known as Total Electron Content (TEC).

GPS-TEC technique has been used to study upper atmospheric physics. Such targets included : large and medium scale travelling ionospheric disturbance (LSTID and MSTID), solar flares, plasma bubbles, ionospheric hole formation by missile launches. In my study, I use this technique to study disturbances caused by earthquakes.

1.2 Previous research in Ionospheric Disturbances

Ionospheric disturbances are recorded in ionospheric TEC, and the change in TEC is easily derived by monitoring the change in the phase differences of the two L band carrier waves from GPS satellites. In addition to the ionospheric disturbances of solar-terrestrial origin such as LSTID and MSTID, past GPS-TEC studies have revealed various kinds of disturbances excited by phenomena in the solid earth, e.g. volcanic eruption (*Heki*,2006), launches of ballistic missiles (*Ozeki and Heki*, 2010), mine blasts (*Calais et al.*, 1998), and so on.

Among others, many studies have been done for Coseismic ionospheric disturbances (CID), the variation of the ionospheric electron density induced by acoustic and gravity waves excited by coseismic crustal movements of large earthquakes (e.g. *Calais and Minster*, 1998; *Heki and Ping*,2005; *Astafyeva et al*, 2009; *Afraimovich et al*,2011; *Tsugawa et al.*, 2011). Ionospheric disturbances by volcanic eruptions are caused by acoustic wave excited in explosive eruptions that reached the thermosphere. Heki (2006) estimated that the energy of volcanic explosion from the amplitudes of the ionospheric disturbances caused by the eruption of Mount Asama in September 2004.

1.2.1 Why Near-Field CID?

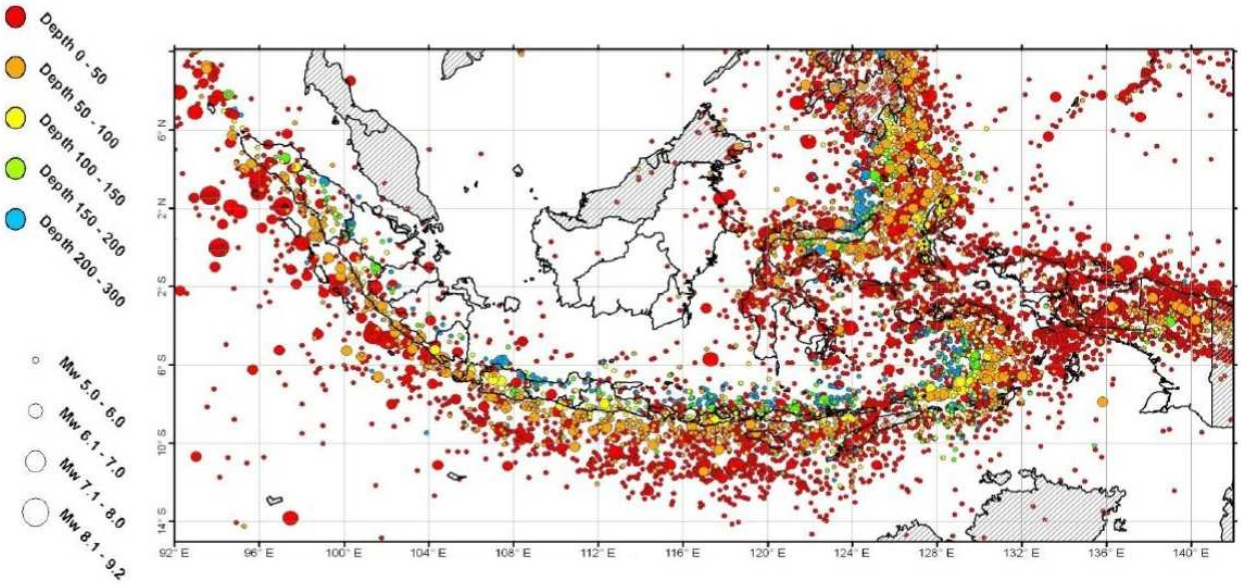
CID could be observed both near the epicenter and far from the epicenter. They have

somewhat different characteristics in velocity, duration, periods, and waveforms. The near-field (short distance) CID is caused by direct acoustic wave excited by coseismic vertical crustal movements. They usually appear 10-15 minutes after the earthquake, which is the time required for the acoustic wave to propagate from the surface to the ionosphere. Due to the close relationship between the near-field CID and earthquake magnitudes, CID could be used as a part of the early warning system of tsunami. In other words, it could be possible to determine the earthquake magnitudes using CID amplitudes well before the arrival of tsunami at the coast.

Amplitudes of near-field CIDs are influenced by many factors including the line-of-sight geometry, directivity, asymmetry, and earthquake mechanism. However, it is the moment magnitude (Mw) that has the largest influence on the amplitudes of near-field CIDs. In this research, I will try to clarify the empirical relationship between Mw and CID amplitudes by studying not only Indonesian large earthquakes but also various other earthquakes world-wide.

1.2.2 CID of the Indonesian earthquakes

Indonesia is situated in the ring of fire where a large number of earthquakes and volcanic eruptions frequently occur in or around islands, e.g. Sumatra, Java, Bali, Flores, and Timor.Indonesian earthquakes have wide range of Mw, which often reach or surpass 9.0. The earthquakes with Mw greater than 8.0 are of major interest not only for CID but also for preseismic ionospheric disturbance studies. Moreover, the country is located to the south of the magnetic equator, and it makes them valuable in the study of directivity asymmetry of the CID propagation.



(www.bosai.jp)

Figure 1.1 Distribution of Indonesian earthquakes with different moment magnitudes and depths. The earthquake epicenters are geographically located both on the northern and the southern hemispheres.

In this research, I focus on the near-field CID of two large inter-plate earthquakes near the Sumatra Island, i.e. the Bengkulu 2007 and Nias 2005 earthquakes. The 2005 Nias earthquake (M_w 8.6) (*Briggs et al.*, 2006) and the 2007 Bengkulu earthquake (M_w 8.5) (*Gusman et al.*, 2010) occurred as mega-thrust earthquakes in the Sunda arc, Sumatra. They are considered as large aftershocks of the 2004 great Sumatra-Andaman earthquake (M_w9.2) (*Banerjee et al.*, 2005), between the subducting Australian Plate and the overriding Sundaland Plates (*Simons et al.*, 2007).

The Nias earthquake occurred ~3 months after the main shock (16:09:36 UTC, 28 March 2005) on a fault segment in the south-eastern extension of the 2004 earthquake rupture area. It ruptured the plate boundary spanning ~400 km along the trench with fault slip exceeding 11 meters. Uplift reaching 3 meters occurred along the trench-parallel belts on the outer-arc islands (*Briggs et al.*, 2005). The Bengkulu earthquake (11:10:26 UTC, 12 Sept. 2007) occurred to the west of southern Sumatra ~3 years after the 2004 Sumatra-Andaman

earthquake. It ruptured the plate interface approximately 220-240 km in length and 60-70 km in width along the Sunda arc. About one half day later, a large aftershock of Mw 7.9 followed.

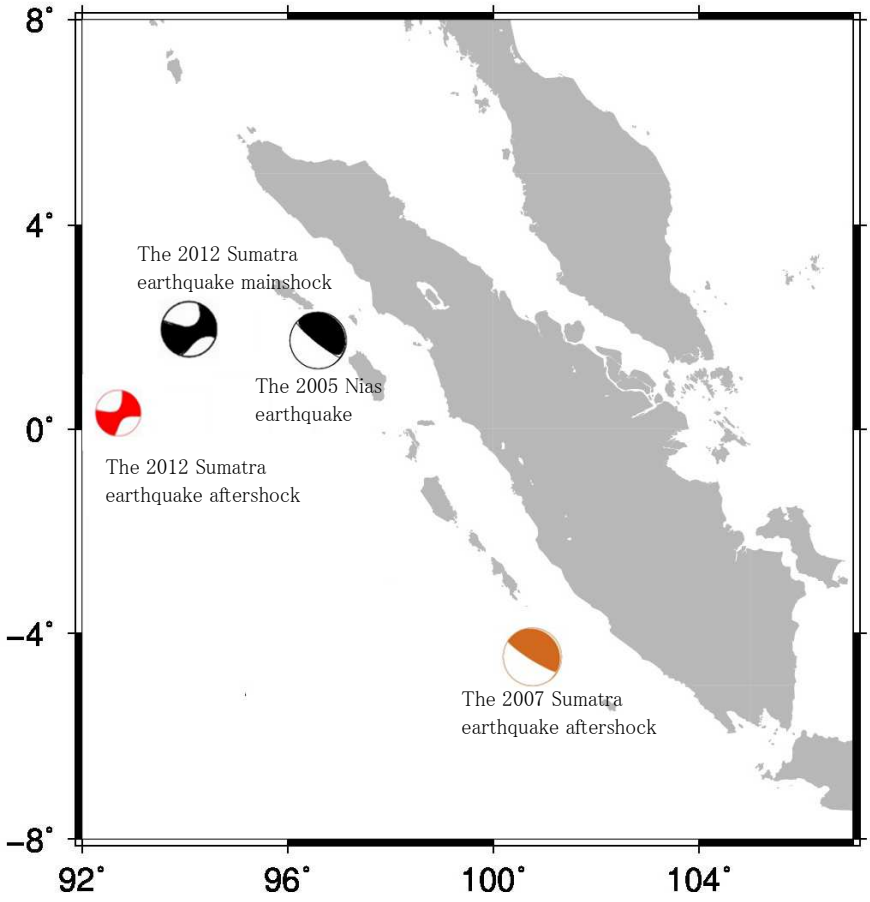


Figure 1.2.The focus of the research includes two megathrust earthquakes i.e. The 2005 Nias and 2007 Bengkulu earthquakes. I also study the two strike-slip earthquakes i.e. The 2012 Sumatra earthquake mainshock and its aftershock. CIDs of these earthquakes will be evaluated in details (waveform, amplitude, propagation speed, etc).

I also investigate the near-field CID of another large earthquake in Indonesia, i.e. the large intra-plate earthquakethat occurred on 11 April, 2012, and its largest aftershock. The Mw 8.6 main shock occurred ~400 km off the Indian Ocean coast of Northern Sumatra, Indonesia (2.31N, 93.06E, focal depth 23 km), at 8:38:37 UT (*Meng et al*, 2012). The largest aftershock (M_w 8.2) occurred ~2 hours after the mainshock (10:43:09 UT) nearby (0.77N,

92.45E, focal depth 16 km). The mainshock had a complex source process, i.e. ruptures of strike-slip mechanism occurred one after another during 160 seconds on four different sub-faults with a relatively slow rupture velocity (*Yue et al*., 2012).

This was the largest strike-slip earthquake ever recorded. Owing to relatively small vertical coseismic crustal movements for strike-slip earthquakes, tsunami height of this earthquake did not exceed one meter. In order to evaluate the CID amplitudes of these large strike-slip earthquakes, I will compare them with near-field CIDs of earthquakes with different focal mechanisms, such as reverse, normal fault earthquakes with Mw ranging from 6.6 to 9.2.

1.3 Outline of the Study

This thesis investigates near-field CID associated with earthquakes using GPS-TEC. The comprehensive analysis conducted in this research includes times series analysis, inference of propagation velocity using travel time diagram, long-lasting TEC oscillation, wave-front geometry and propagation directivity. I also try to elucidate empirical relationship between CID amplitudes and moment magnitudes. Finally, I look for pre-seismic ionospheric disturbances.

In Chapter 2,I give detailed description on the data processing. Physics behind CID and pre-ionospheric disturbances are also briefly discussed in this chapter. I will introduce several geophysical indices such as Disturbance Storm Time (DST) Index, and will explain the Okada's (1992) model used to calculate horizontal and vertical displacement by dislocation of a rectangular fault in a half space. Calculation of Sub-Ionospheric Point (SIP) and Ionospheric Pierce Point (IPP) will also be briefly explained.

Chapter 3 describes the Ionospheric disturbance in the 2007 Bengkulu earthquake and the 2005 Nias earthquake, Sumatra, Indonesia, observed by regional GPS network. I perform

comprehensive studies of co- and pre-seismic ionospheric disturbance of the 2007 Bengkulu earthquake in terms of monochromatic TEC oscillation, CID travel time diagram, comparison of CID amplitudes between the mainshock and the largest aftershock. Long-term and short-term pre-seismic ionospheric disturbances are also discussed in this section. I will also show that such co- and preseismic TEC anomaly studies could not be performed for the 2005 Nias earthquake because of severe plasma bubble activities.

Chapter 4 describes the co- and preseismic ionospheric disturbances of the two biggest strike-slip earthquake occurred off the coast of North Sumatra in April 2012. Other topics in this chapter include propagation velocity/directivity, TEC oscillation, and snap shots of preseismic TEC anomalies. In order to elucidate the relationship between moment magnitude and CID amplitude, we collected GPS-TEC data of near-field CID of 21 earthquakes which covered all of the three types of earthquake faultings, i.e. reverse, normal and strike-slip faulting. I will discuss the empirical relationship between the CID amplitudes and earthquake magnitudes.

In Chapter 5, I give conclusions of previous chapters, and propose several recommendations for a future tsunami early warning system based on CID observations.

Chapter 2

Data Processing

2.1 GPS Data

The GPS satellites located ~20,000 km above the earth's surface transmit microwave signals by two *L*-band carrier waves (~1.2 and ~1.5 GHz), and they come through the ionosphere before reaching ground receivers. For accurate positioning, we remove ionospheric delays through the generation of ionosphere-free linear combinations of the two carrier phases (L_3):

$$L_3=f_1^2/(f_1^2-f_2^2)L_1-f_2^2/(f_1^2-f_2^2)L_2 \qquad (2.1)$$

f_1, f_2 is the frequencies of L_1-band and L_2-band carrier wave signals, respectively. For ionospheric studies, the phase difference of the two frequencies (L_4) is often called the ionospheric linear combination.

The microwave signals undergo frequency-dependent delays in the ionosphere. By tracking the differences between the L_1 and L_2 phases (L_4), we could monitor the temporal changes of TEC along LOS (called slant TEC). TEC is usually expressed in TEC units (1 TEC unit corresponds to 10^{16} el/m^2). 1 TECU is defined as the total number of electrons integrated between two points, along a tube with 1 m^2 cross section. Ionospheric

linear combination is often further processed to obtain absolute TECs by removing ambiguities (and cycle –slips) and inter-frequency biases in phase data(e.g. *Sardón et al.*, 1994). However, the process is beyond the scope of this research, in which I focus on short-term relative changes in TEC. The variable used to calculate L_4 was obtained from Receiver Independent Exchange Format (RINEX) files of GPS (i.e. Rinex files). RINEX is the GPS observation data interchange format, and allows us to perform post-processing of the data. To calculate GPS satellite orbits, we have to transfer coordinate of the satellites in another RINEX files (Navigation data) to earth-fixed system. The coordinate is used further to calculate Sub-Ionospheric Point (SIP) trajectory. The concepts of the two carriers and ionospheric combinations, and IPP/SIP are explained in Figure 2.1.

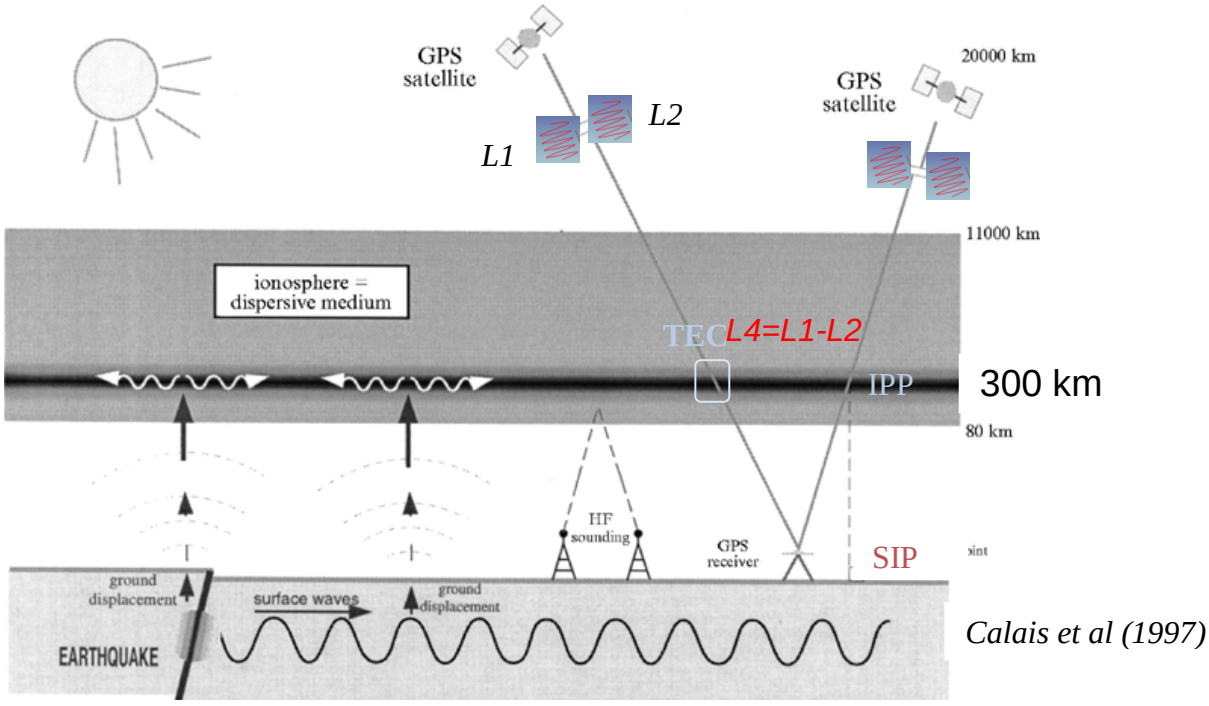


Figure 2.1 when the earthquake occurred, the ground displacement generate not only seismic wave but also atmospheric waves that propagate up to the F-layer of ionosphere. It causes disturbances in this layer. The line-of-sight (LOS) between GPS satellites and ground GPS receivers penetrate ionosphere (we often assume it as a thin layer in altitude 300 km above earth surface). GPS transmits L_1 and L_2 band as carrier wave and TEC is calculated as the difference between the L_1 and L_2 phases (or called by L_4). Intersection between LOS and ionosphere is called as Ionospheric Pierce Point (IPP), and the projection of IPP onto the ground is called as Sub-Ionospheric Point (SIP).

In order to obtain L_4, L_1 and L_2 are converted from radians to the length by multiplying the wavelength of each carrier. The difference between L_1 and L_2 is determined to obtain L_4. TEC is obtained from L_4 by multiplying with a certain factor.

$$\Delta L_4 = L_1 - L_2 \tag{2.2}$$

$$\Delta TEC = (1/40.308)\, f_1^2 f_2^2/(f_1^2 - f_1^2)\Delta L_4 \tag{2.3}$$

The raw RINEX data were downloaded from the data centers of SUGAR (Sumatra GPS Array) and IGS (International GNSS Service). The sampling interval of the SUGAR stations was 2 minutes, four times as long as the standard sampling interval (e.g. in IGS) of 30 seconds. Data from 22 and 14 SUGAR sites were available on the days when the 2007 Bengkulu and the 2005 Nias earthquakes occurred. In addition, we also use three 3 IGS stations in northern Sumatra (samp), Java (bako), Indonesia, and Singapore (ntus). To analyze the behaviour of TEC in the period without major earthquakes, we also downloaded GPS raw data of the biti station in the Nias Island which covered 4 month span (including the 2007 Bengkulu earthquake).The SUGAR data in 2012 employed shorter sampling interval (15 seconds) in most stations, suitable for CID studies.

2.1 Coseismic Ionospheric Disturbances (CID)

TEC shows apparent variations due to the motion of the satellite in the sky. It is also caused by diurnal variation of the solar zenith angle and long-term disturbances e.g. large-scale traveling ionospheric disturbances (LSTID). In order to eliminate such long-term variations and to isolate CID, high-pass filters are applied. In this research we employ polynomials up to sixth degree of time, and the residual value from these polynomials is used to study CID. On the other hand, due to longer time scale of preseismic TEC enhancement,

we employed the procedure devised by *Ozeki and Heki* (2010) and *Heki* (2011).There we can detect TEC anomalies with longer time scales (up to an hour) assuming that the temporal changes of vertical TEC obey cubic polynomials of time. An example of the TEC anomaly time series are given in Figure 2.2.

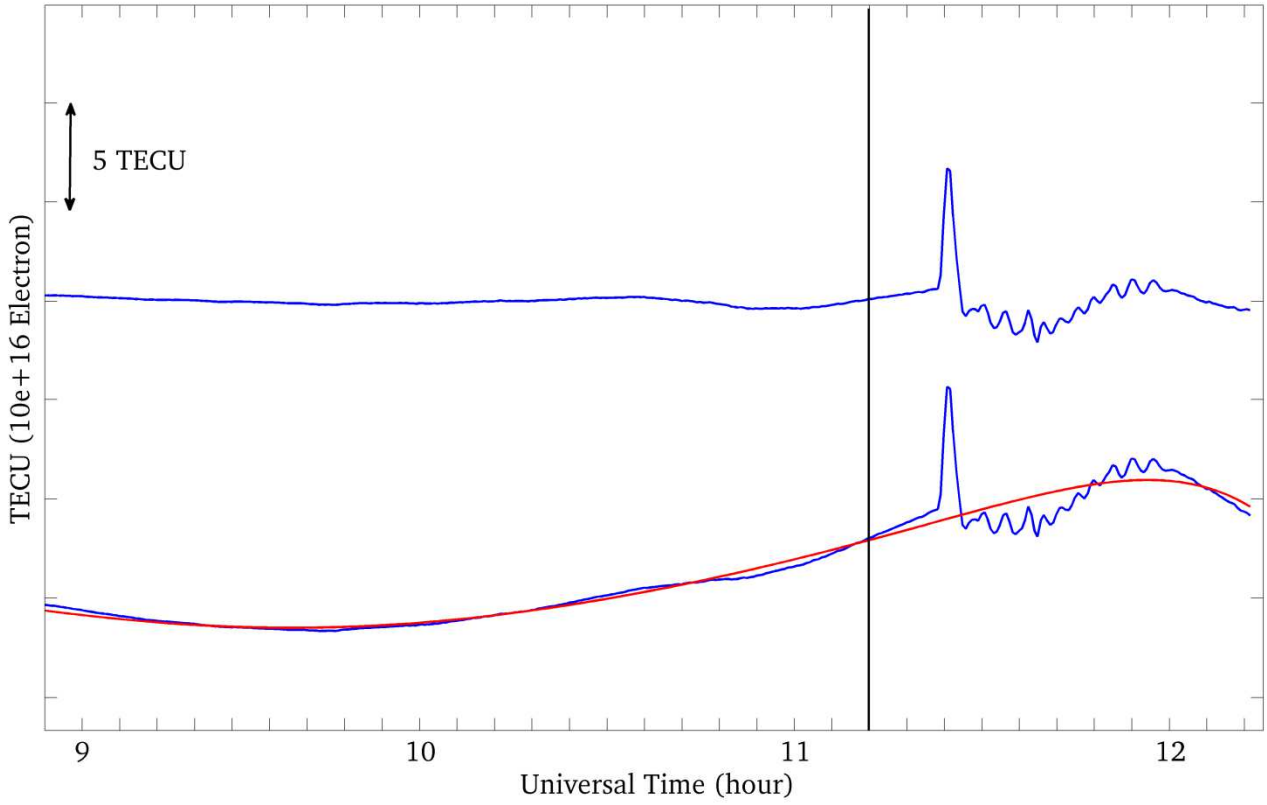


Figure 2.2 The Slant TEC changes before and after the 2007 Bengkulu earthquake measured from the samp station using Satellite 25, (bottom) Slant TEC variation (blue) modeled with a polynomial with degree up to 6 (red). The strong positive peak shows Coseismic Ionospheric Disturbances (CID) of the earthquake. (top) Slant TEC variation of the earthquake after subtracting the model.

-

Preseismic ionospheric disturbance is defined as the anomaly of TEC that occurs prior to a large earthquake. Electromagnetic precursors of earthquakes had been investigated by many researchers using different approaches. They include currents in the ground (*Uyeda and Kamogawa,* 2008), propagation anomaly of VLF (*Molchanov and Hayakawa, 1998*) and VHF (*Moriya et al.*, 2010) radio waves. Here I focus on precursory changes in TEC.

There are two different approaches for studies of preseismic TEC anomalies, namely long-term and short-term anomalies. As for long-term precursors, *Liu et al.*(2001) investigated the behaviour of GPS-TEC 4-5 days before earthquake, and found anomalies before many large earthquakes including the 2008 Wenchuan earthquake (*Liu et al.*,2010). Here I focus on the short-term preseismic ionospheric disturbances, and adopt the method used by *Ozeki and Heki* (2010) and *Heki* (2011).

To model background ionospheric changes, we use equation (2.4).

$$\text{Slant TEC}\ (t, \zeta) = \text{VTEC}\ (t)\ /\cos\zeta + d \tag{2.4}$$

The formula models the raw TEC with a function of time t, ζ is the angle between line-of-sight and the local zenith, d is the constant bias specific to individual satellite-station pairs. VTEC is determined by using least-squares adjustment. For a time span of a few hours, VTEC changes could be well modeled with a cubic function of time t.

$$\text{VTEC}(t) = at^3 + bt^2 + ct + d \tag{2.5}$$

The variables a,b,c,d, and e are to be estimated using the least-squares method. In order to avoid influences of earthquake-related disturbances, I excluded a certain time period to estimate the reference curve. The excluded time is from 40 minutes before the earthquake to 20 minutes after earthquake. This exclusion interval is adopted from *Heki and Enomoto* (2013), where they studied the behaviour of VTEC obtained by removing inter-frequency biases and integer ambiguities using external sources. Appearance of preseismic TEC enhancements of the 2011 Tohoku-oki earthquake was also supported by foEs at the Kokubunji ionosonde and geomagnetic declination data (*Heki and Enomoto,* 2013).

I used slightly different method to study the preseismic ionospheric disturbances of the Indonesian earthquakes because inter-frequency biases of the SUGAR stations are not available. So I plot the anomalies of slant TEC derived as the deviations from these reference curves. An example of preseismic anomalies is given in Figure 2.3.

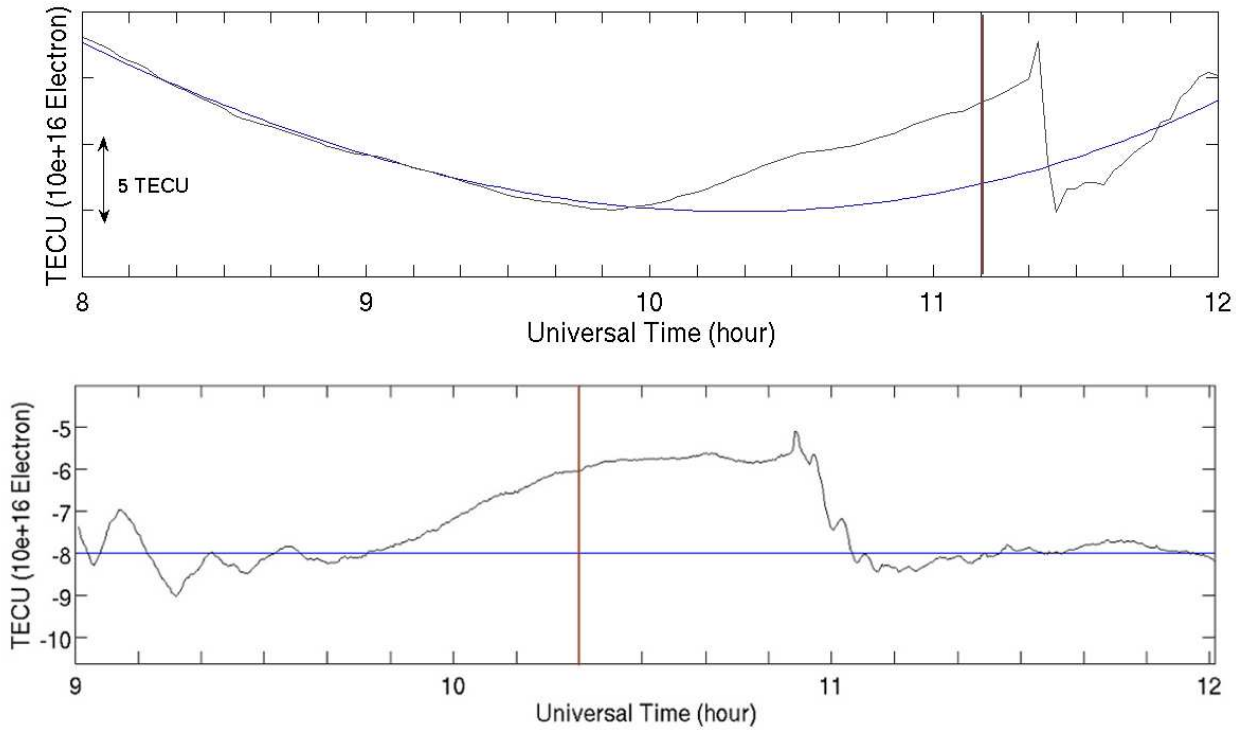


Figure 2.3 (Top) preseismic TEC changes before the 2007 Bengkulu earthquake (black) with its model polynomial of three (blue line). (bottom) the residual preseismic TEC changes before the 2012 Sumatra earthquake (black line) with its model polynomial of three (blue line). The vertical axis shows anomalies in the slant TEC.

2.3 Long-term Preseismic Ionospheric Disturbances

We also investigated long-term preseismic ionospheric disturbances in the 2007 Bengkulu earthquake in addition to the short-term preseismic TEC anomalies. *Liu et al.* (2001) and *Liu et al.* (2010) found that the TEC showed anomalous behaviours 4-5 days before the 1999 Chichi and 2008 Wenchuan earthquakes. On the other hand, *Yao et al.* (2012) did not find such long-term TEC anomalies before the 2010 Chile earthquake.

To detect anomalous behaviours of long-term TEC changes, the median *M* of every

successive 15 days period of the vertical TEC was calculated. In the next step, the deviation of the observed one on the 16^{th} day from the median was also calculated. The anomaly is considered to be significant when observed TEC is greater/less than UB/LB (defined in the next paragraph) and the geomagnetic activity is quiet. The UB (upper bound) and LB (lower bound) are defined as :

$$\text{LB}=M-1.5(M-\text{LQ}),\ \text{and UB}=M+1.5(\text{UQ}-M), \tag{2.6}$$

where LQ and UQ means the lower and upper quartiles, respectively.

2.4 Sub-Ionospheric Point (SIP) and Ionospheric Pierce Point (IPP)

In GPS-TEC studies, we often assume that ionosphere is an infinitesimal thin single layer at a fix altitude from the earth (we usually assume 300 km). Intersection of the line-of-sight of the satellite with this layer is called Ionospheric Pierce Point (IPP). Then the projection of IPP on the earth surface is called Sub-Ionospheric Point (SIP). The SIP trajectory is important to discuss spatial characteristic of the TEC anomalies.

SIPs are often over 1000 km away from GPS stations when the satellite elevation is small. We also calculate penetration angles of the line-of-sight vectors to the hypothetical thin ionosphere. Such angles are used to convert anomalies in slant TEC to those in vertical TEC. Figure 2.4 shows an example of SIP trajectories in the two cases, the 2007 Bengkulu and 2012 North Sumatra earthquakes.

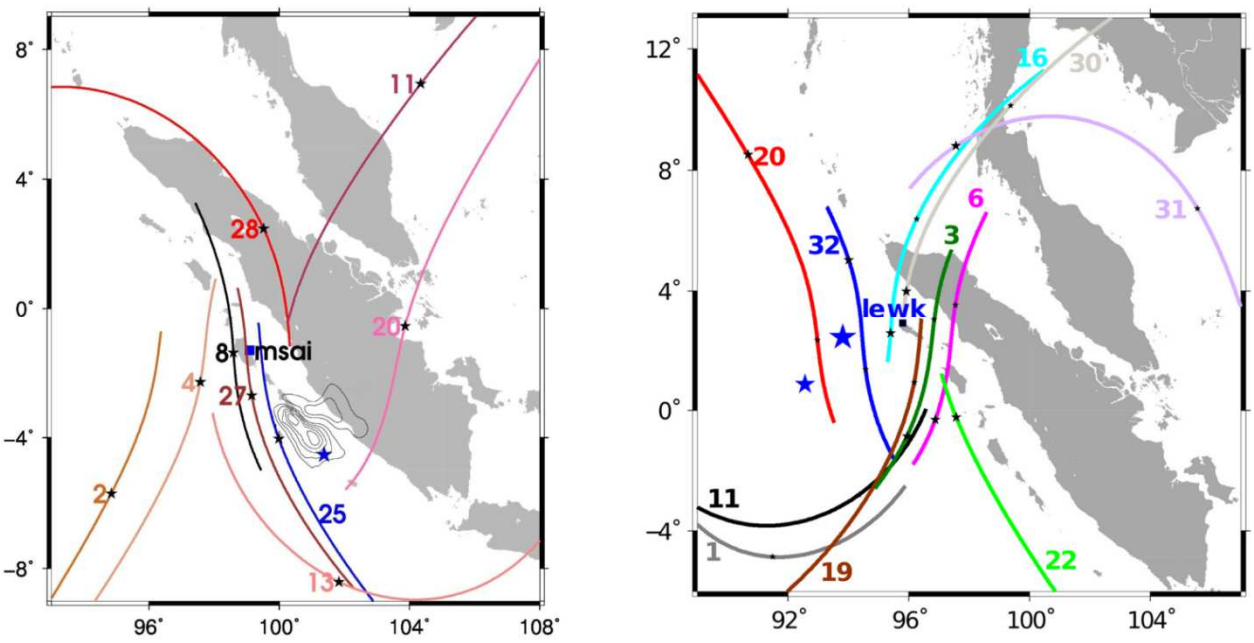


Figure 2.4. (Left) trajectory of SIP before and after the 2007 Bengkulu earthquake from the station msai. Small black stars are SIP at 11:10 and the contour shows the coseismic uplift (contour interval: 0.2 m) of this earthquake (*Gusman et al.*, 2010). The large blue star shows the epicenter. (Right) SIP trajectory before and after the 2012 North Sumatra earthquake from the station lewk.Two blue stars are the epicenters of the mainshock (large star) and the largest aftershock (small star). Numbers attached to the SIP trajectories show GPS satellite numbers.

2.5 Calculating GIM

Global Ionosphere Maps (GIM) are composed of vertical TEC values at grid points distributed worldwide. They are obtained from GPS/GLONASS data mainly from the IGS stations. The value of the VTEC was interpolated using spherical harmonics expanded up to degree and order 15. The spatial resolution of these maps is 2.5 degree in latitude and 5 degree in longitude, and their time resolution is 2 hours. The files of GIM are available from several analysis centers including CODE (Center for Orbit Determination in Europe) located at the University of Berne, Switzerland. They also provide FORTRAN programs to handle these files.

In this research, GIM is utilized mainly for normalizing CID amplitudes in order to study the scaling law, i.e. the relationship between earthquake moment magnitude and CID

amplitudes. Figure 2.5 shows an example of the distribution of vertical TEC obtained by CODE GIM.

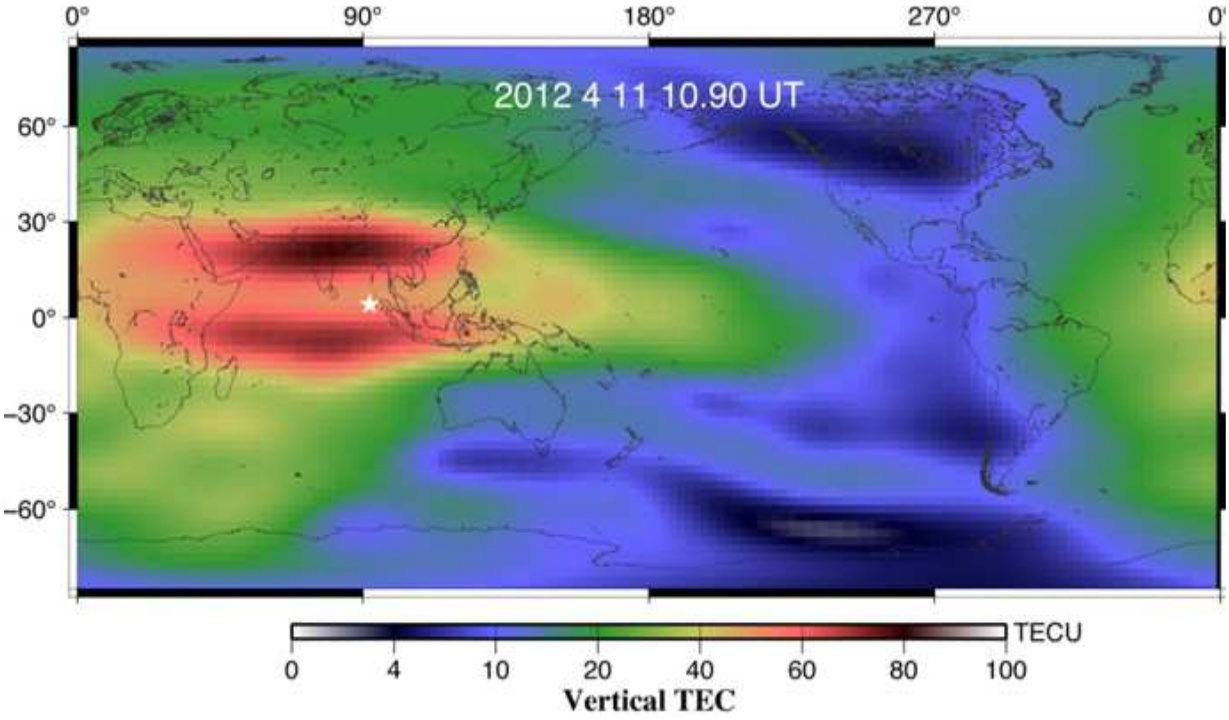


Figure 2.5.Distribution of vertical TEC worldwide derived from a Global Ionosphere Map (GIM).This GIM expresses the ionosphere at the time when the CID of the largest aftershock of the 2012 North Sumatra earthquake was observed. The white star shows its epicenter.

2.6 Calculating the propagation speed of the disturbances

In order to determine whether the coseismic TEC anomaly signals are caused by acoustic wave or internal gravity wave, we have to calculate their propagation speed using the diagram to correlate focal distance and time. The slope of the line connecting the appearances of CIDs corresponds to the velocity of the CID propagation. Here I performed least-squares adjustment to estimate the slope, using the following simple model, i.e.

$$y=at+b, \qquad (2.7)$$

where y is the distance of SIP (at the time when CID appeared) from the epicenter and t is the time after the earthquake occurrence. The value a is the velocity of the CID propagation.

2.7 Blackman-Tukey Method

Acoustic resonance in 3.7 mHz and 4.4 mHz is found in the Earth's background free oscillation (*Nishida et al.,* 2000), caused by the resonant coupling between the solid earth and the atmosphere. In order to calculate power spectral density of TEC oscillation, we obtained spectrograms using the Blackman-Tukey method. In this method, we first obtain the autocorrelation function of the time series, and then perform Fourier transformation of this function to obtain power spectral density.

In the Blackman-Tukey approach, power spectral density $P_X(f)$ is defined as

$$P_X(f) = |\sum_{k=0}^{M-1} w_k r_k e^{-2\pi i f k}|, \tag{2.8}$$

where r_k is the autocorrelation at time lag k, M is the maximum lag considered and window length, and w_k is the windowing function.

2.8 DST Index

The Dst (disturbance storm time) index represents the degree of geomagnetic activity, and is commonly used to quantify the condition of space weather. Occurrences of typical storms are indicated by Dst indices > 70 nT or <-50 nT (*Oh and Yi*, 2011). It is important to monitor geomagnetic activity with this index, in order to know if the observed TEC disturbances are related to earthquakes or non-seismic disturbances caused by geomagnetic activities. We can download these indices from the Omni website run by NASA(http://omniweb.gsfc.nasa.gov/form/dx1.html).

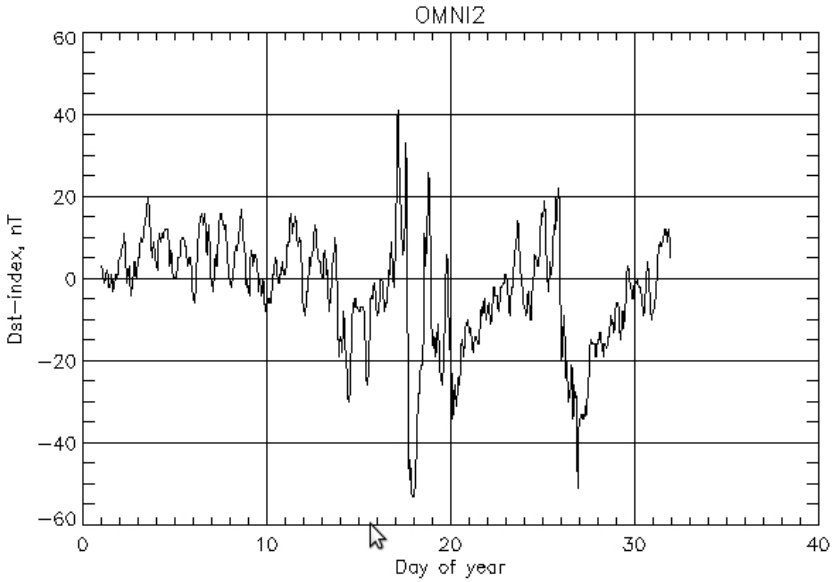


Figure 2.6. Dst index from January 1 to January 31, 2013. Magnetic storm can be found on days 17-18 and 27-28, when the Dst indices are≤-40 nT.

2.9 Earthquake Mechanism

In general, earthquake is caused by sudden movement of the rock along faults to release stress built up by the relative movements of the earth`s tectonic plates. When earthquake occurred, seismic waves are generated and propagate over long distances.

There are three types of faulting mechanisms of earthquakes. The first type is the normal faulting, in which the overriding side of the rock goes down relative to the other side.This occurs under tensile crustal stress. The second type is the reverse faulting. There, the overriding side is pushed up relative to the other side. This occurs under compressional crustal stress. The third is the strike-slip faulting. There, the rock moves almost horizontally in the direction of fault strike. This occurs when crustal stress is tensile in one direction and compressional in the direction perpendicular to it.

Here I study CIDs of the two big strike-slip earthquakes that occurred in 2012 April off the Northern Sumatra. I also study CIDs of large reverse fault earthquakes including the 2005 Nias and 2007 Bengkulu earthquakes, Indonesia.

(www.usgs.com)

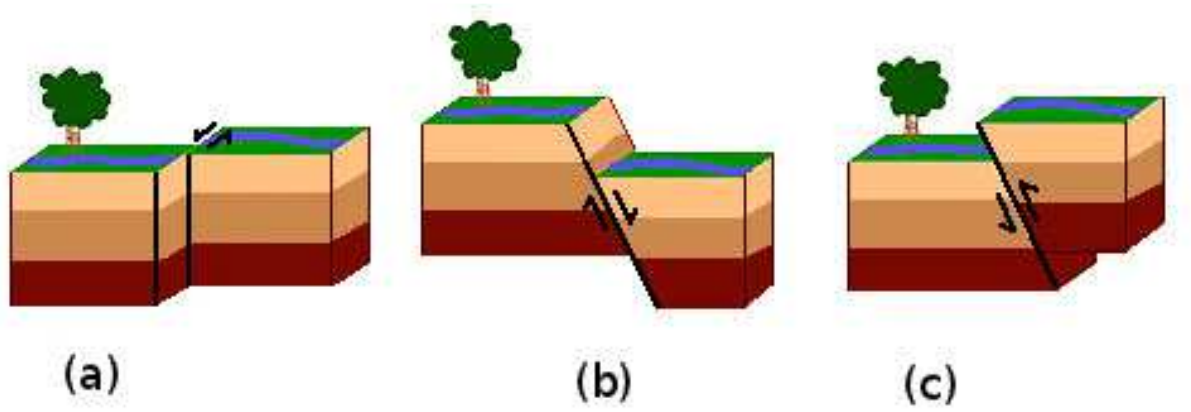


Figure 2.5. Three mechanisms of earthquake faulting, (a) strike-slip faulting, (b) normal faulting, and (c) reverse faulting. CIDs of earthquakes with these three mechanisms are compared in order to investigate dependence of amplitudes of CID on the faulting mechanisms.

2.10 Okada's (1992) model

To calculate the ground displacement caused by earthquakes, dike intrusions, *Okada* (1992) introduced a model to calculate surface deformation due to shear and tensile faulting in an elastic half-space. The FORTRAN program written by Dr. Y. Okada provides the Green's function to enable such calculations. Parameters needed for the calculation is the geometryof the rectangular fault,i.e. length, width, depth, strike and dip, and 3-component of the dislocation vector. The model outputs are the three components of the displacement vector as well as the strain tensor. Because *Okada* (1992) model gives analytical solution (and FORTRAN code) for surface deformation due to shear and tensile faulting, it is used world-wide to calculate coseismic ground deformation to be compared with GPS observations of station movements.

In this study, I used the *Okada* (1992) model to calculate coseismic vertical and horizontal displacements by the two strike-slip earthquakes in the 2012 North Sumatra earthquake: mainshock and the largest aftershock. The vertical displacements are especially important because they excite atmospheric waves and CID.

Chapter 3

Ionospheric disturbances of the 2007 Bengkulu and the 2005 Nias earthquakes, Sumatra, observed with a regional GPS network

The content of this chapter was published in *Journal Geophysical Research Space Physics*,

Cahyadi, M. N., and K. Heki (2013), Ionospheric disturbances of the 2007 Bengkulu and the 2005 Nias earthquakes,Sumatra, observed with a regional GPS network, *J. Geophys. Res.Space Physics*, **118**, 1777–1787, doi:10.1002/jgra.50208.

3.1 Introduction

There are many large earthquakes in Indonesia. The CID of the 2004 Sumatra-Andaman earthquake has been investigated in detail by *Heki et al.*(2006). However, the 2005 Nias and 2007 Bengkulu earthquakes have not been studied in terms of ionospheric disturbances yet. In fact, they are the two largest thrust earthquakes whose ionospheric disturbances have not been studied in spite of the availability of GPS data. Continuous GPS stations in Sumatra and smaller islands along the Sunda Trench have been operated as the SUGAR (Sumatra GPS Array) network, which is designed, constructed and operated by members of the Tectonics Observatory at Caltech and the Indonesian Institute of Sciences (LIPI). We also used some stations of the IGS (International GNSS Service) network. Here, we investigate CID associated with these earthquakes, and compare them with past earthquakes.

Acoustic waves are excited by vertical movements of the ground or the sea surface. They propagate upward and reach the F layer height of the ionosphere in ten minutes or so. There the waves make irregularities of electron density, which are detected as CID (*Heki and Ping*, 2005; *Rolland et al.*, 2011a). *Astafyeva et al.*(2009) identified two distinct propagation velocities of such acoustic waves after the Hokkaido-Toho-Oki earthquake of 4 October 1994, i.e. the slow component of ~1 km/second and the fast component of ~4 km/sec. They inferred that they were excited by coseismic vertical crustal movement and by the Rayleigh surface wave, respectively. In the Tokachi-Oki earthquake of 23 September 2003, *Heki and Ping* (2005) found north-south asymmetry, i.e. CIDs are clearly seen only on the southern side of the epicenter. They suggested that geomagnetic field is responsible for such directivity. It would be important if such velocities and directivity are also seen in the 2007 Bengkulu and 2005 Nias earthquakes.

Choosakul et al., (2009) found that the acoustic resonance characterized by the TEC

oscillation with periods of 3.7 and 4.5 minutes followed the CID of the 2004 Sumatra-Andaman earthquake, and lasted for hours. *Saito et al.*, (2011) and *Rolland et al.*, (2011b) also reported similar resonant oscillation after the 2011 Tohoku-Oki earthquake. In this earthquake, the GPS network also detected another component, i.e. the internal gravity wave propagating with a speed ~0.3 km/sec (*Tsugawa et al.*, 2011). Because of the large magnitudes of the 2007 Bengkulu and 2005 Nias earthquakes, we can expect to detect similar signals after these earthquakes.

Among various kinds of earthquake precursors reported so far (*Rikitake*, 1976), electromagnetic phenomena have been explored worldwide, e.g., electric currents in the ground (*Uyeda and Kamogawa*, 2008), a propagation anomaly of VLF (*Molchanov and Hayakawa*,1998) and VHF (*Moriya et al.*, 2010) radio waves, and satellite observations (*Němecet al.*, 2008). *Heki* (2011) suggested that mega-thrust earthquakes are immediately preceded by the enhancement of TEC by analyzing recent M9 class interplate thrust earthquakes, i.e. the 2004 Sumatra-Andaman and the 2008 Maule earthquakes, in addition to the 2011 Tohoku-Oki earthquake. The possible precursors reported by *Heki* (2011) have obvious temporal and spatial correlations with earthquakes and clear magnitude dependence, although physical processes have not been identified yet.

As the second focus of the present study, we examine if similar precursory TEC anomalies occurred before the 2007 Bengkulu and the 2005 Nias earthquakes. Apart from such short-term precursors, there have been reports of TEC anomalies in a longer term, 3-5 days before earthquakes (e.g. *Liu et al.*, 2001; 2009). We also briefly examine if this type of anomaly preceded the 2007 Bengkulu earthquake. Thus, this research presents the first comprehensive GPS-TEC case study treating both co- and preseismic ionospheric disturbances of specific mega-thrust earthquakes.

3.2. TEC Changes in the 2007 Bengkulu Earthquake

3.2.1. CID amplitudes and waveforms

As we described in Chapter 2,in order to investigate spatial characteristics of the disturbances, e.g. propagation speed of such disturbances, we calculate ionospheric piercing point (IPP) of line-of-sights assuming a thin layer of ionosphere at altitudes ~300 km. Then SIP,projections of IPP onto the ground, are derived. First we investigate the TEC responses to the Bengkulu earthquake 2007. In Figure 3.1, we show raw slant TEC time series 9-13 UT recorded by all the satellites visible from the station msai in the Sibelut Island. For the five satellites, 4, 8, 25, 27, and 28, clear CID appear after the earthquake with time lags of 11-16 minutes, time needed for acoustic waves to travel from the surface to the IPP. The slant TEC fluctuations have amplitudes of 0.4-1.5 TECU and periods of 4-5 minutes.

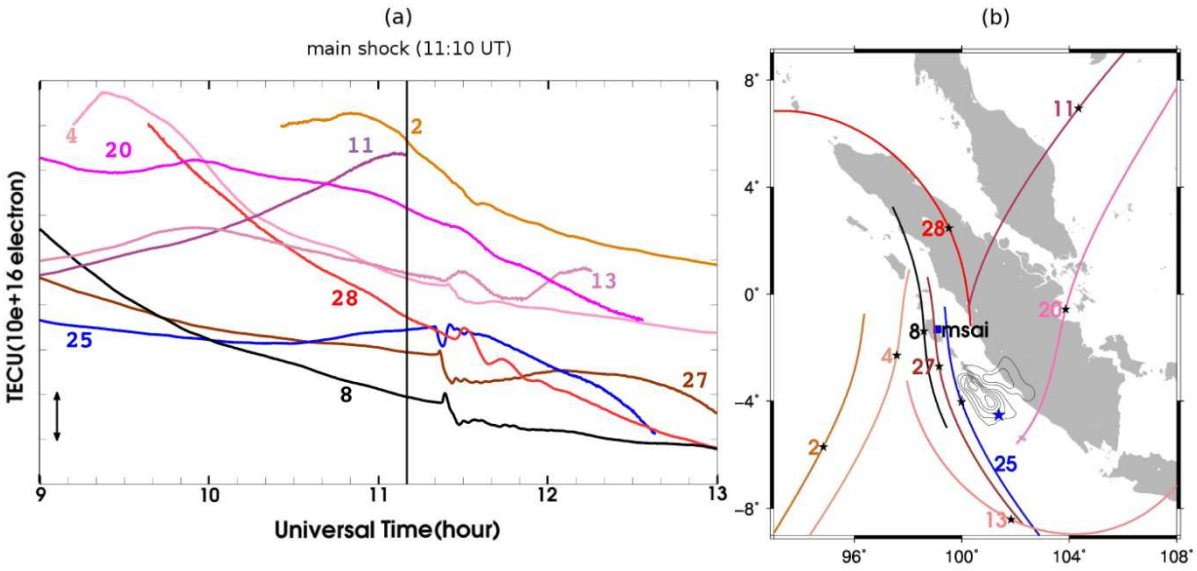


Figure 3.1 (a) Time series 9.00-13.00 UT of raw slant TEC changes observed at the msai station (position shown in b) with nine GPS satellites. The black vertical line indicates the occurrence of the 2007 Bengkulu earthquake (11:10 UT). CIDs are seen 11-16 minutes after the earthquake. (b) Trajectories of SIP for satellites shown in (a). On the trajectories, small black stars are SIP at 11:10 and the contour shows the coseismic uplift (contour interval: 0.2 m) of this earthquake (*Gusman et al*., 2010). The large blue star shows the epicenter.

Astafyeva and Heki (2009) compared the CID waveforms of the 2006 and 2007 large earthquakes that occurred with reverse and normal mechanisms, respectively, in the Kuril Islands. They found that a CID starts with positive (negative) changes, i.e. TEC increase (decrease), suggesting that compression (rarefaction) atmospheric pulse leads the acoustic wavefront in the 2006 (2007) earthquake. Acoustic waves lead by the rarefactions are unstable but might reach the ionosphere when the earthquake is large enough (the 2007 event exceeds M_w8). Figure 3.1 suggests that the CID of the 2007 Bengkulu earthquake started with a positive polarity, which is consistent with the reverse faulting mechanism of this earthquake. Satellite 25 appears to show a negative initial change, but this might be due to the low sampling rate, i.e. the narrow positive peak failed to be sampled (see also Fig.3.2c).

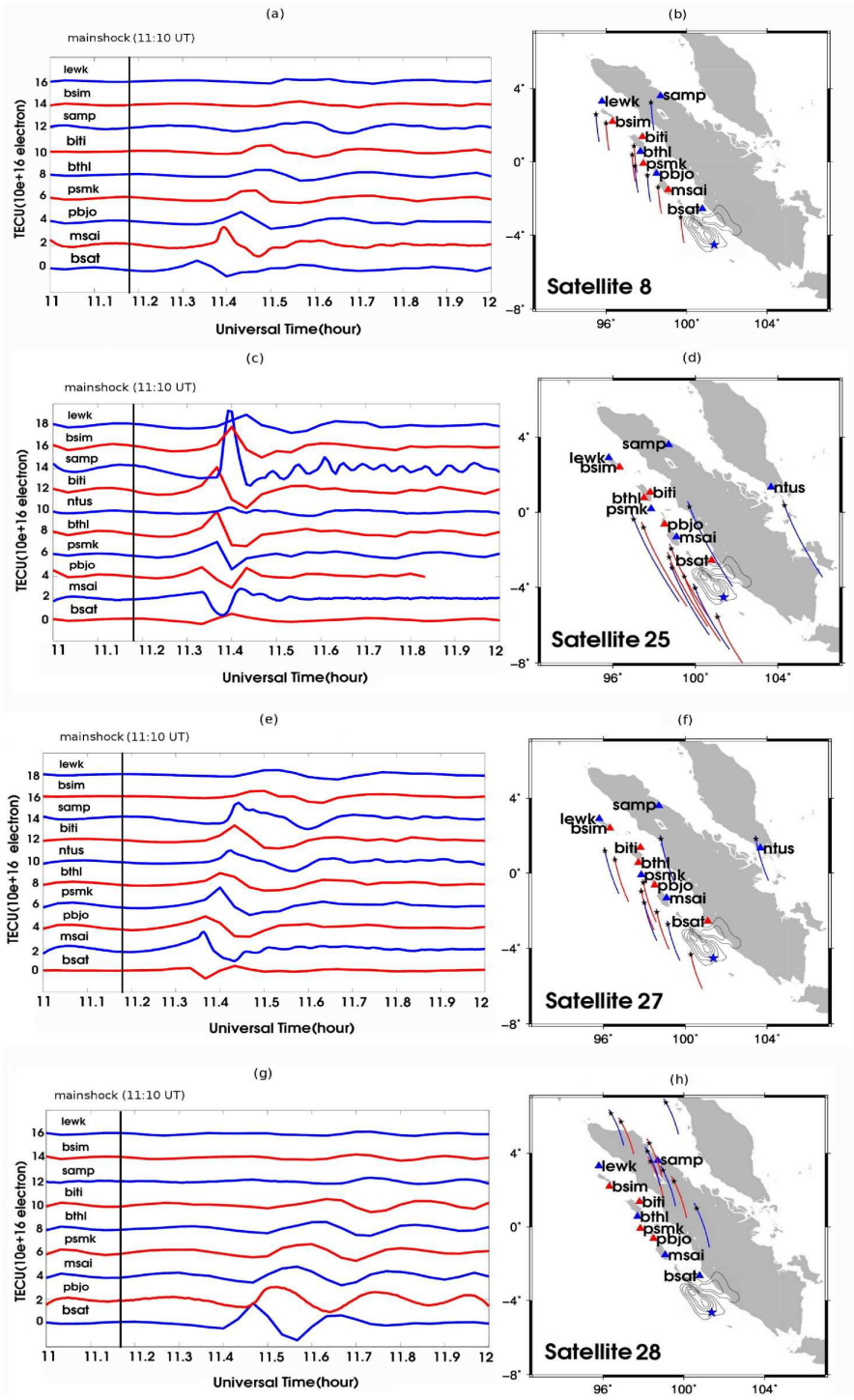


Figure 3.2 Time series 11.00-12.00 UT of slant TEC changes and their SIP trajectories by four satellites, i.e. satellites 8 (a, b), 25 (c, d), 27 (e, f), and 28 (g, h). The black vertical lines in the time series (a,c,e, and g) indicate the time of the 2007 Bengkulu earthquake. On the trajectories (b,d,f, and h), small black stars are SIP at 11:10 UT. The contour shows the uplift and the blue star shows the epicenter (see Figure 3.1 caption). The triangles are the GPS stations, and their colors (blue or red) coincide with those of the SIP track and TEC time series.

For satellites 8, 25, 27, and 28, slant TEC time series observed at 9-10 GPS stations are plotted in Figure 3.2. These time series were obtained as the residuals from the best-fit degree 6 polynomials used as the high pass filter. The disturbances are seen to start with positive anomalies in most cases. The satellites 25 and 27 were both in the southern sky during this time interval, moving from north to south. The disturbances by both of these satellites were similar in waveform, but the amplitudes that were seen in the satellite 25 were larger. As inferred from the propagation velocity (see the next section), the CID is of acoustic wave origin, and its wavefront tilts from the epicenter outward near the epicenter (see, e.g. Figure 2 of *Heki et al.* (2006)). The larger CID with satellite 25 would reflect shallower angles between the line-of-sight and the wave front.

Satellite 28 was in the northern sky, and CID amplitudes are considerably small in the stations to the north of the epicenter. In the geometry of the satellite 28, the line-of-sight penetrates the wavefront in a deep angle, and the positive and negative electron density anomalies tend to cancel each other. In Figure 3.2c (satellite 25), two stations, ntus and bsat, show signals significantly smaller than the others. The small signal at ntus simply reflects the long distance of its SIP from the source (Figure 3.2d). The small signal at bsat, closer to the source than other sites, would have come from the deep angle of the line-of-sight penetration with the front. The northward beam of the CID in the southern hemisphere (*Heki and Ping*, 2005) may have further reduced the signal at bsat.

As shown in Figure 3.2c, the satellite 25 shows the largest CID at the samp station, northern Sumatra. In addition to the line-of-sight and wave front geometry, this also reflects the fact that at samp, an IGS station, the sampling interval is 30 seconds, one fourth of other SUGAR stations. The SUGAR stations would have simply missed the highest peak of CID. In Figure 3.3a, we compare satellite 25-samp time series with the original sampling interval and those arbitrarily re-sampled with the 2 minutes interval. The latter peak is much lower (~3 TECU) than the former (~5 TECU).

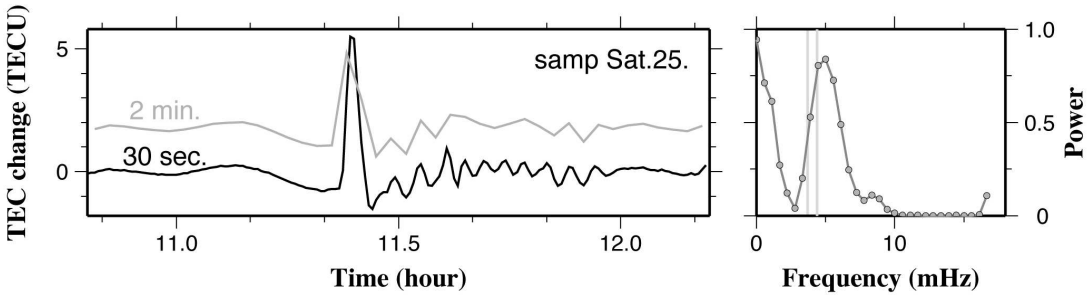


Figure 3.3. Comparison of the CID recorded at the samp station for satellite 25 in 2 minutes sampling (light grey) and 30 second sampling (black). Power spectrum of the time series (30 sec.) between 11.5 and 12.0 are shown to the right. The observed peak (~5 mHz) is close to one of the two atmospheric resonance frequencies indicated by vertical lines (3.7 and 4.4 mHz).

In Figure 3.3, samp station shows clear monochromatic oscillation of TEC lasting for half an hour. Spectral analysis (by the Blackman-Tukey method) suggests that its period is close to ~4.4 mHz, one of the atmospheric resonance frequency often observed after large earthquakes (*Choosakul et al.*, 2009; *Saito et al.*, 2011; *Rolland et al.*, 2011b). Figure 3.3 also shows that such oscillation becomes ambiguous with the lower sampling rate. Thus, it is recommended to use sampling intervals of 30 seconds or less for detailed studies of ionospheric disturbances by earthquakes.

3.2.2. Propagation speeds

Apparent velocity of CID was calculated from the arrival time differences at points of various distances from the center of crustal uplift. Travel time diagrams based on the data from the four satellites are shown in Figure 3.4. There the short-term slant TEC anomalies shown in Figure 3.2 are expressed in colors painted on curves showing the relationship between the travel time (horizontal axis) and focal distance (vertical axis). Slopes of the black lines connecting the peak positive TEC anomalies (red part) correspond to the apparent velocity of CID. The propagation velocity derived using all the four satellites with the least-squares method is 0.69 ±0.04 km/sec (1σ) (Figure 3.4).

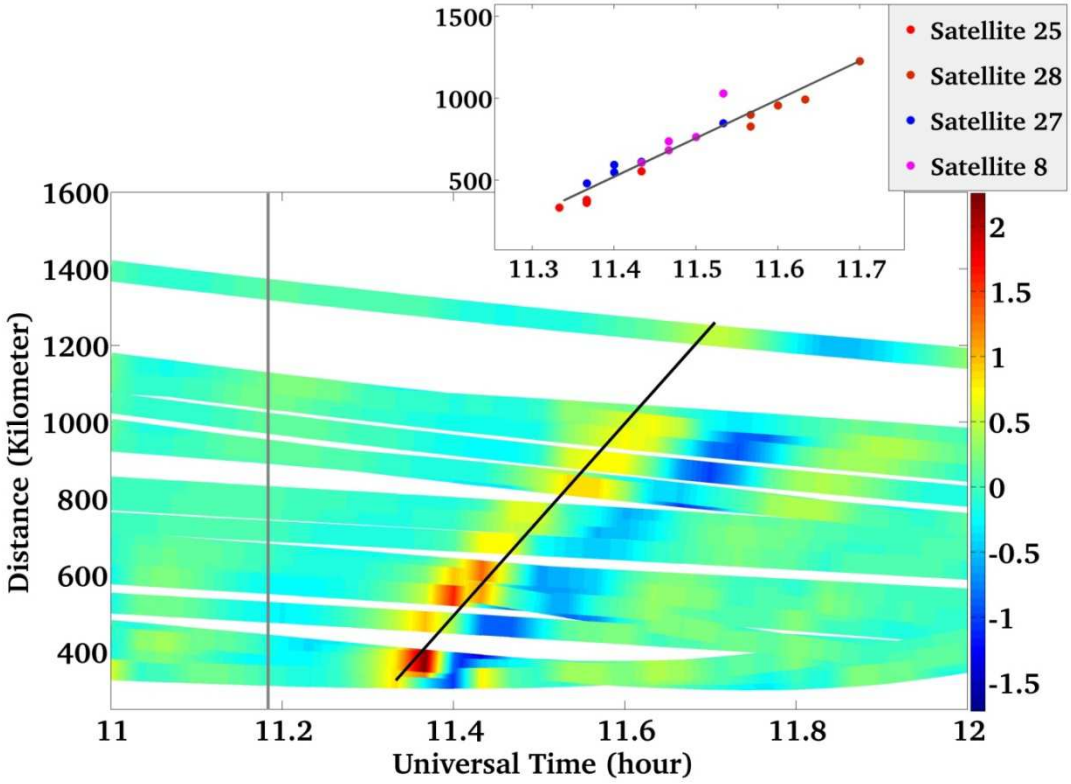


Figure 3.4.Travel-time diagram of the 2007 Bengkulu earthquake CID based on the data from satellites 8, 25, 27 and 28. Distances are measured from the center of the uplift region (contour map in Figure 3.1b) rather than the epicenter. The apparent velocity is 0.69 km/s with the 1σ error of ±0.04 km/sec. The grey vertical line indicates the occurrence of the earthquake (11:10 UT). The inset shows the arrival times of the maximum positive TEC anomalies for different satellites, for which linear regression has been performed.

Astafyeva et al. (2009) showed that CID has two distinct velocity components, i.e. the fast component propagating with the velocity of the Rayleigh surface wave (3-4 km/sec) and the slow component propagating with the sound velocity (0.6-1.0 km/sec). The velocity obtained in this study clearly corresponds to the latter. The GPS stations are distributed along the arc, i.e. in the direction corresponding to the node in the radiation pattern of the Rayleigh surface wave. The absence of the Rayleigh surface wave signatures would be due to their small amplitude coming from such geometric conditions. There is no clear gravity wave signature in Figure 3.4.

Heki and Ping (2005) demonstrated north-south asymmetry of the CID propagation, i.e. a CID hardly propagates northward because geomagnetism allows only oscillation of ionospheric electrons in the field-aligned direction in the F layer. This would reverse in the southern hemisphere, i.e. southward CID could be much smaller than northward CID in the 2007 Bengkulu earthquake. Unfortunately, we could not confirm this adequately because most of the SUGAR stations are located to the north of the fault. We just mention here that there is one station mlkn, on the Enggano Island, south of the epicenter, and it showed much smaller CID amplitude than the stations to the north did (not shown in Figure 3.2). The propagation directivity will be discussed again using the CID data of the 2012 North Sumatra earthquake in the next chapter.

3.2.3. Pre-seismic Ionospheric Anomalies

3.2.3.1. Long-term anomalies

It has been suggested that the amplitudes of diurnal variations of TEC significantly decreased 3-4 days before the 1999 Chi-chi (Taiwan) earthquake (*Liu et al.,* 2001) and 4-6 days before the 2008 Wenchuan (China) earthquake (*Liu et al.*,2009). Based on statistical analyses, *Le et al.* (2010) suggested that such preseismic anomalies tend to appear 1-4 days

before earthquakes with higher probability before larger and shallower earthquakes. On the other hand, *Dautermann et al.*(2007) analyzed data 2003-2004 in southern California, and did not find statistically significant correlation between TEC anomalies and earthquake occurrences.

Here we estimated the hourly vertical TEC over one-month period including the 2007 Bengkulu earthquake using the GPS-TEC data at the station biti, the Nias Island, following the method of *Astafyeva and Heki* (2011). We did not use the Global Ionospheric Model (GIM) because its spatial resolution is not sufficiently high (*Mannucci et al.*, 1998). We show the results over 18 days in Figure 3.6. Positive and negative anomalies exceeding natural variability were detected using a method similar to the one used in past studies (i.e. deviations larger than 1.5 times of the quartile from the median of the last 15 days are judged as anomalous). Diurnal variations are fairly regular. Occasional positive TEC anomalies occur (e.g. days 245, 246, and 250) shortly after geomagnetic disturbances shown as the Dst (Disturbance storm time) indices (see Figure 3.5 for the indices in a larger time window). This index shows the averaged change of the horizontal component of geomagnetic field at multiple magnetometers near the magnetic equator.

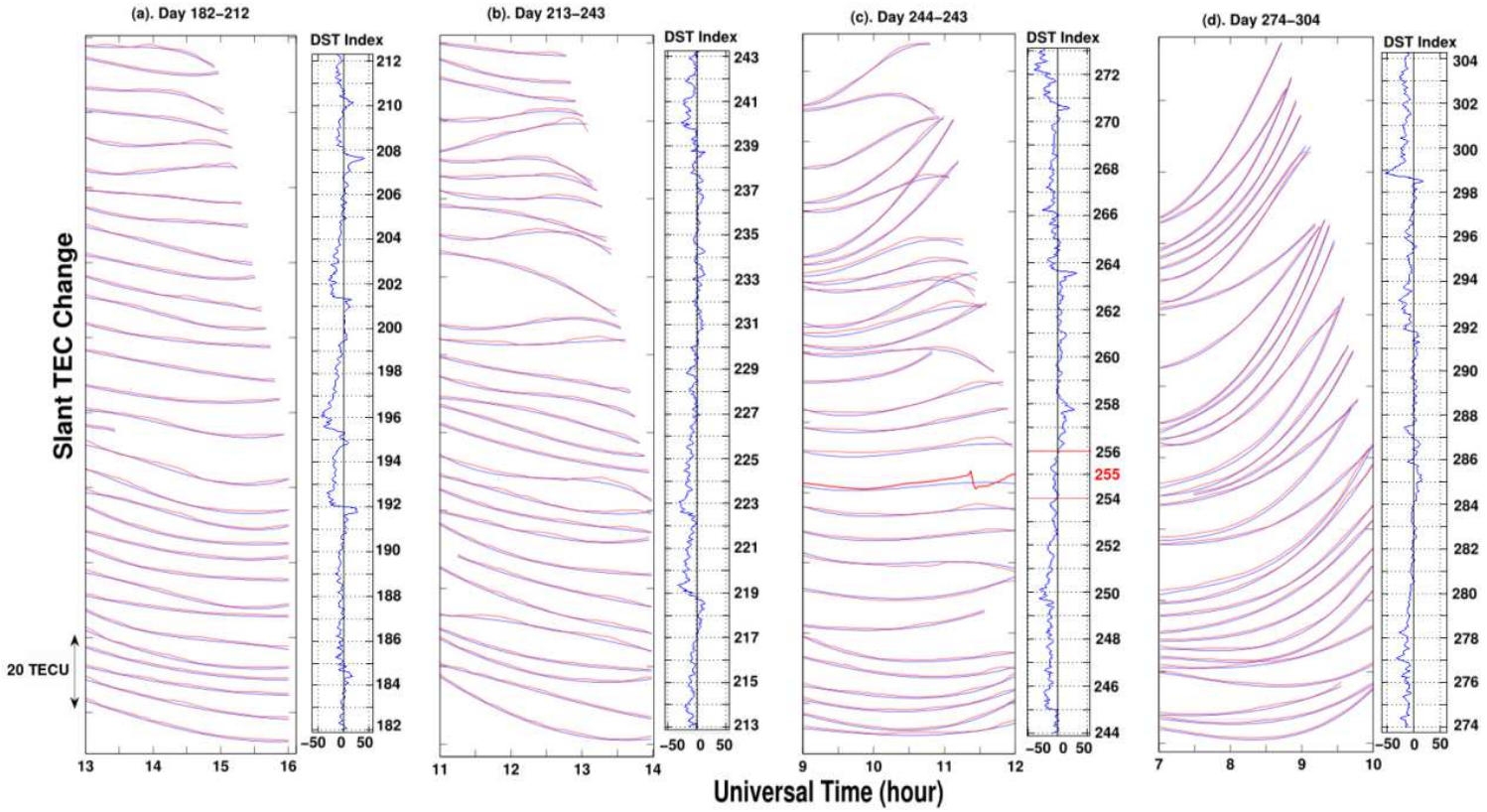


Figure 3.5 4 months of slant TEC time series over 3 hours periods observed at biti with the satellite 25 (shown in Figure 3.6a,b). (a), (b), (c), and (d) approximately correspond to July, August, September, and October, respectively. The data shown with the bold red curve indicates the data on the earthquake day(day 255). The time window is moved backwards two hours per month because the GPS orbital period is a half sidereal day (i.e. appearance of the satellite 25 becomes earlier by ~4 minutes per day). Thinner curves show models in which VTEC changes are approximated with cubic functions of time (the whole five hours periods shown in the figure are used to derive the models). The Dst (disturbance space-time) indices (average disturbance of the north component of geomagnetic fields) over the same period are also shown.

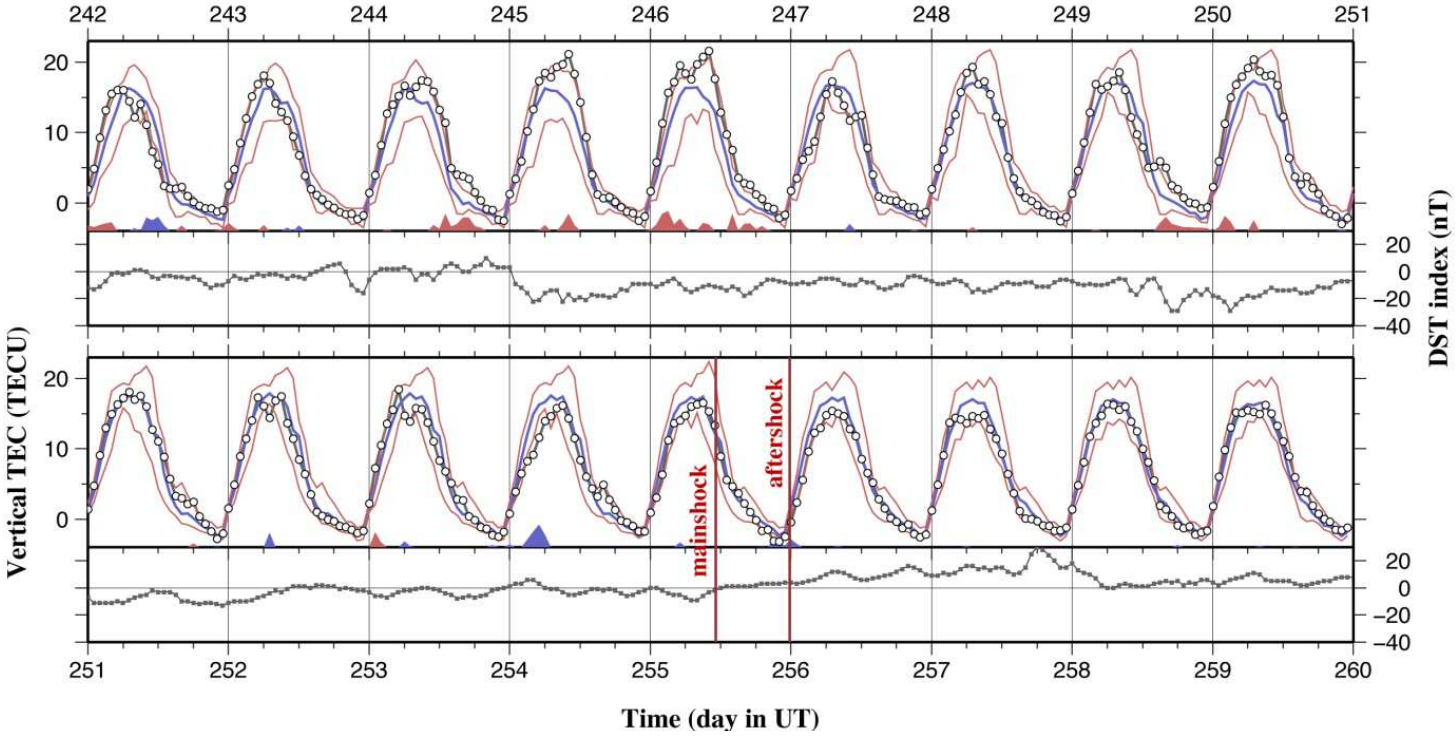


Figure 3.6. Time series of absolute vertical TEC (open circles connected with black lines) at the biti GPS station in the Nias Island, over 15 days including the 2007 September 12 Bengkulu earthquake (day of the year 255 in UT, thick vertical line). Thick black curve shows the median of the preceding 15 days with upper and lower bounds of natural variability (taken 1.5 times as far from median as quartiles) shown by thinner curves. Red and blue shades at the bottom show the amount of positive and negative anomalies (amount above/below the upper/lower bounds of natural variability). There are positive anomalies in days 245-246, and days 249-250, and they are possibly related to geomagnetic disturbances on the day 245 and 249, respectively, as seen in the Dst indices.

During 1-4 days before the main shock (days 251-254), TEC mostly remains normal with just a short and small negative anomaly on the previous day. The same situation is found for the 2010 M_w 8.8 Chile (Maule) earthquake. *Yao et al.* (2012) reported that no significant long-term TEC anomalies preceded the 2010 Maule earthquake. According to the statistical study (*Le et al.*, 2010), larger earthquakes tend to be preceded by clearer long-term TEC anomalies. Hence, the absence of the clear long-term TEC precursors before the 2007 Bengkulu and the

2010 Maule earthquakes raises a serious question about the existence of such long-term anomalies.

3.2.3.2. Short-term anomalies

Heki (2011) showed that positive TEC anomalies started about 40 minutes before the 2011 Tohoku-Oki earthquake, and suggested that similar anomaly preceded the other two M9 class mega-thrust earthquakes, i.e. the 2004 Sumatra Andaman and the 2010 Maule earthquakes. Although the 2007 Bengkulu earthquake is somewhat smaller in magnitude, it is worth studying if similar TEC anomaly occurred prior to the earthquake.

In Figure 3.7, we show raw slant TEC time series over four hours period before and after the earthquake at seven GPS stations for satellites 25, 27 and 8. We derived reference curves following *Ozeki and Heki* (2010) and *Heki* (2011), i.e. modelling the vertical TEC as a cubic polynomial of time. We excluded the time interval 10.0-11.4 UT, which are possibly influenced by CID and preseismic anomalies, in estimating the models. Preseismic ionospheric anomalies, similar to those reported in *Heki* (2011), seem to exist. Their onset time varies from~30 minutes (lnng in Figure 3.7c) to ~60 minutes (biti in Figure 3.7a) before the earthquake. The anomalies are dominated by increases in TEC, with smaller amounts of decrease seen in southern stations. The largest increase is 1-2 TECU in vertical TEC, which is about 10 percent of the background value (Figure 3.6).

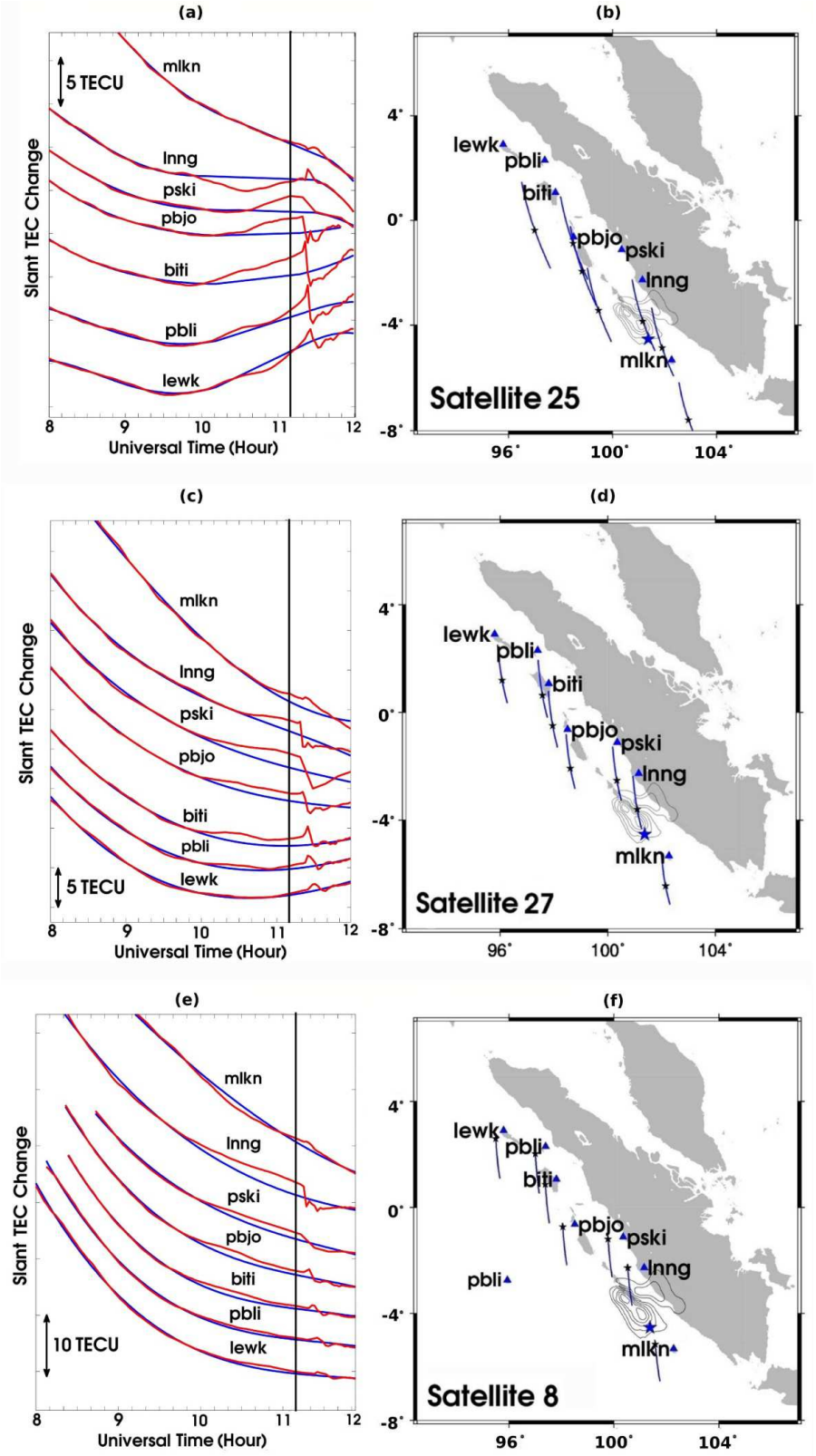


Figure 3.7. Slant TEC change time series taken at seven GPS stations with the satellites 25 (a,b),27 (c,d),and 8 (e,f). Temporary positive TEC anomalies started 60-30 minutes before the earthquake and disappeared after the CID passages. Vertical gray lines are the 2007 Bengkulu earthquake occurrence time (11:10UT). Black smooth curves are the models derived assuming vertical TEC changes as cubic polynomials of time (10.0-11.4 is excluded in

estimating the model curves), and anomalies shown in Figure 3.7 are defined as the departure from the model curves. Shown on the map are the positions of the seven GPS stations (blue triangles) and their SIP trajectories 10.6–11.5 UT (the black stars indicate 11:10). Contours of the coseismic uplift are the same as Figure 3.1.

The enhanced TEC anomalies recover after CID, and this can be understood as the combined result of physical and/or chemical processes, i.e. the mixing of ionosphere by acoustic waves and recombination of ions transported downward (*Saito et al.*, 2011; *Kakinami et al.*, 2012; *Shinagawa et al.*, 2013). In order to see its influence, we changed the end of the exclusion intervals to 12.4 UT (i.e. one hour later than the nominal interval), and found that the results are robust against such changes. Figure 3.8 indicates snapshots of geographical distribution of TEC anomalies at three epochs, 1 hour, 20 minutes, and 1 minute before the earthquake. The anomalies appear to have started ~60 minutes before the earthquake and to have expanded on the northern side of the fault. Negative TEC anomalies are seen on the southern side of the fault.

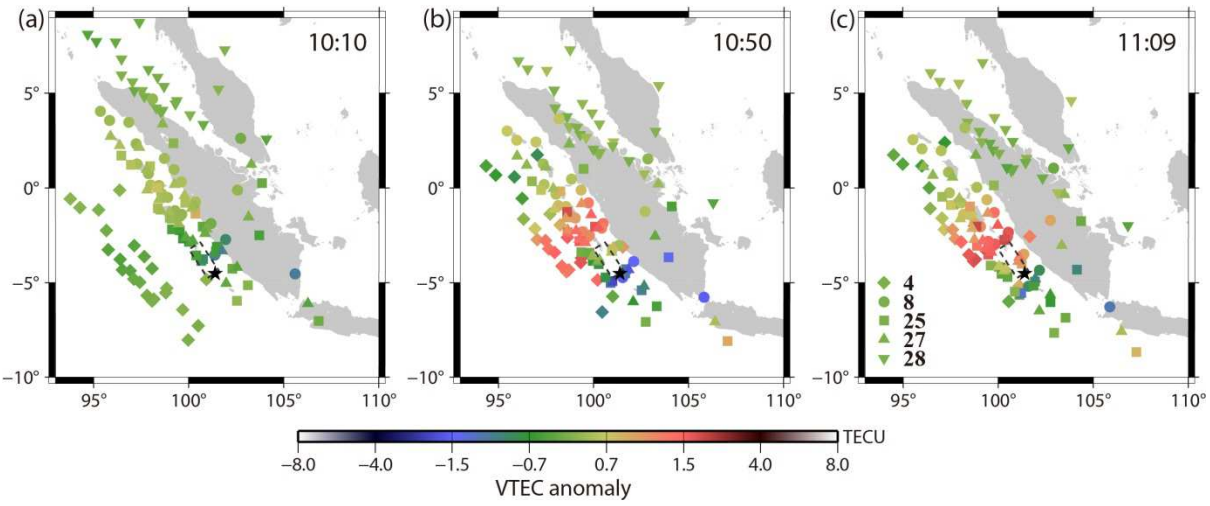


Figure 3.8. Vertical TEC anomalies at three time epochs, (a) 1 h, (b) 20 min, and (c) 1 min before the earthquake, observed at GPS stations with satellites 4, 8, 25, 27, and 28. Positive anomalies (red color) develop around the northern end of the ruptured fault (broken square) area while negative anomalies (blue color) are seen around the southern end.

3.2.3.3. Comparison of short-term preseismic TEC changes with other earthquakes

Figure 3.9 compares preseismic TEC anomalies derived in this study (the lnng station, satellite 27) with those before three M9 class mega-thrust earthquakes and the 1994 Hokkaido-Toho-Oki earthquake (M_w 8.3) reported in *Heki* (2011). The amplitude of the anomaly of the 2007 Bengkulu earthquake is a little larger than the 2010 Maule earthquake, and smaller than the 2011 Tohoku-Oki earthquake. It does not significantly deviate from the overall trend shown in the inset.

Because of limited availability of GPS data, parameters other than earthquake magnitudes are non-uniform, e.g. background TEC and distance from the fault. However, these factors are not as important as the magnitude considering that the 1.0 difference in M_w signifies the difference of a factor of 30 in the released energy (the horizontal axis of the Fig. 3.9 inset spans over three orders of magnitudes in seismic energy). In contrast, background TEC and distances from faults do not vary that much (say, by a factor within 2 or 3) in the cases of Figure 3.9.

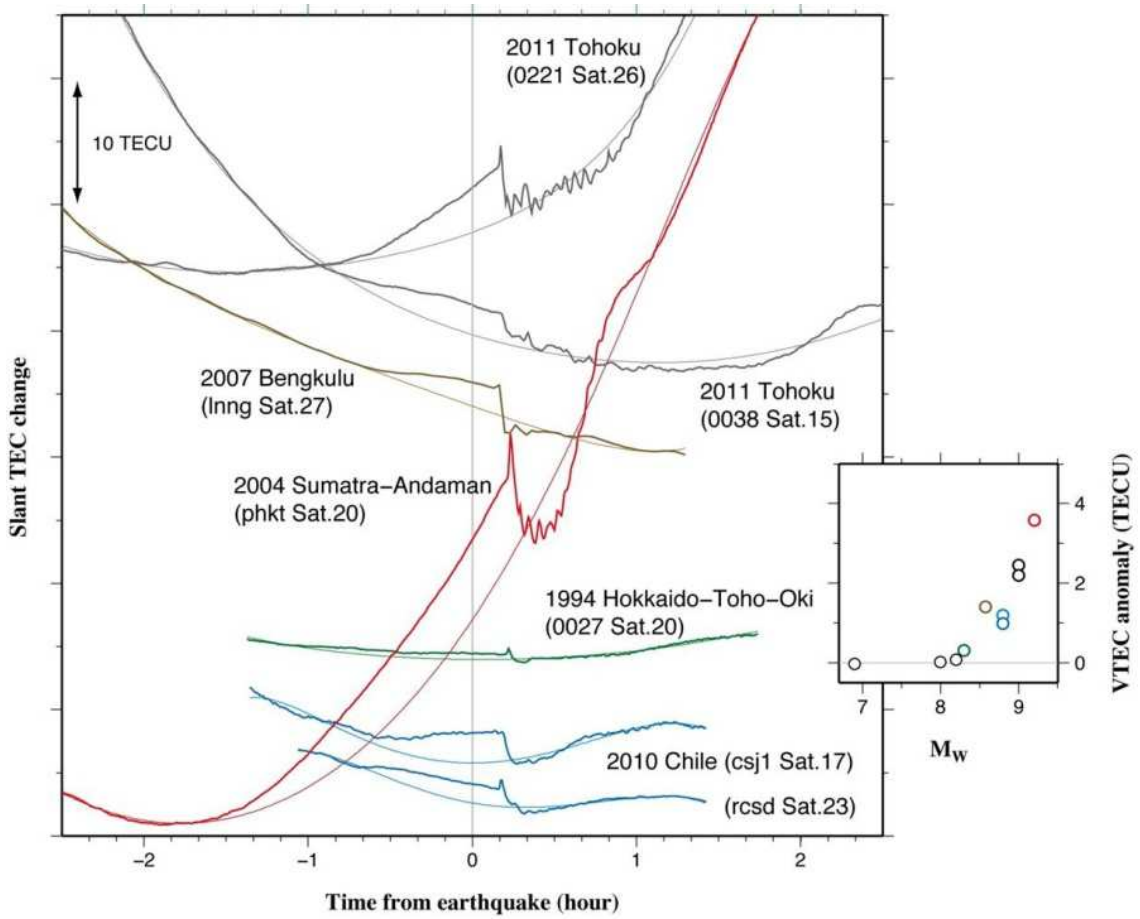


Figure 3.9. Preseismic TEC anomalies of the 2007 Bengkulu earthquake (brown) compared with other large earthquakes reported by Heki (2011). The inset shows the dependence of the vertical TEC anomaly at the time of the earthquake occurrences on the moment magnitudes of the earthquakes (colors correspond to those of the TEC change curves).

There are no widely accepted models for such preseismic TEC anomalies. *Kuo et al.* (2011) suggested rock current as seen in laboratory experiments for stressed rocks (*Freund*, 2000) could change daytime TEC by 2-25 percent. Concentration of such positive electric charges on the surface preceding the fault rupture might be a possibility. Recently, *Enomoto* (2012) proposed that the coupled interaction of earthquake nucleation with deep earth gases might be responsible for the preseismic anomaly in TEC.

Next we discuss how often such TEC anomalies occur during days without earthquakes. In Figure 3.5, I plot the raw TEC changes and the best-fit cubic polynomials for the same combination of the GPS satellite (Sat.25) and the station (biti) over the 4 months period including the earthquake. We also show the Dst indices during this period to see geomagnetic

activity. During periods of high geomagnetic activity, TEC often shows transient enhancements apparently similar to those seen in Figure 3.6 (*Kil et al.,* 2011; *Migoya-Oru´e et al.,* 2009; *Ngwira et al.,* 2012). Occurrences of typical geomagnetic storms are indicated by Dst indices >70 nT or < -50 nT (*Oh and Yi*, 2011). The time series of this index show only small scale disturbances around the earthquake day (day 255), and the TEC changes were moderate within a few days of the earthquake.

The exception is the earthquake day, the only day out of the studied period when the TEC deviated by more than 3σ from the model. Figure 3.10 shows the rms (root-mean-squares) from individual curves obtained as the residuals from the models. The residuals of individual days show a normal distribution and the largest rms (0.84 TECU) corresponds to the earthquake day.

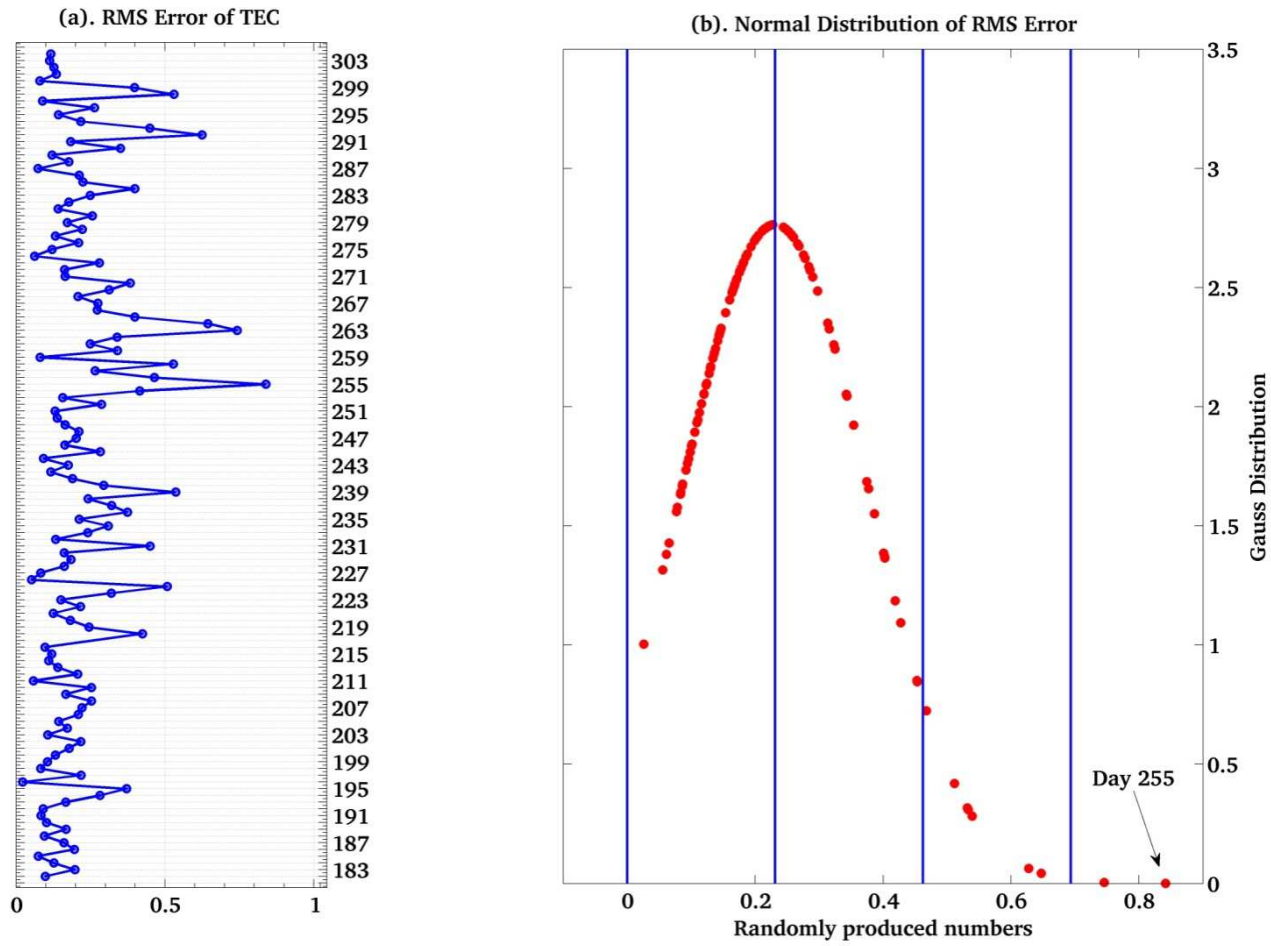


Figure 3.10(a) rms of the difference between models and observations for the 4 months of slant TEC time series shown in Figure not Fig.3.5. The day 255 has the largest value of rms. (b) Normal distribution of the error indicates that the rms on the day 255 exceeds 4.

We cannot completely rule out the possibility that space weather activity caused the anomaly on the earthquake day. Quiet geomagnetic conditions only mean that such probability is less than the case of earthquakes during geomagnetic storms (e.g. 2011 Tohoku-Oki earthquake). In fact, about -3 nT of change in the *z* component of the interplanetary magnetic field (B_z) occurred on the day of the 2007 Bengkulu earthquake, which might have moved the F region plasma and changed TEC.

In Fig. 3.11, we plotted TEC changes in the same time window from six GPS stations with similar longitudes but different latitudes. They remain calm except the CID signature of satellite 17 in the Christmas Island (XMIS), south of Sumatra, and severe scintillation

signatures in an Antarctic station (CAS1). We repeated the same for six stations with similar latitudes (Fig. 3.12), and found that there were no significant disturbances during the studied time window (at COCO the satellite 17 with the northern most SIP possibly shows the preseismic TEC enhancement). Hence we consider it rather unlikely that the observed preseismic changes are of space weather origin.

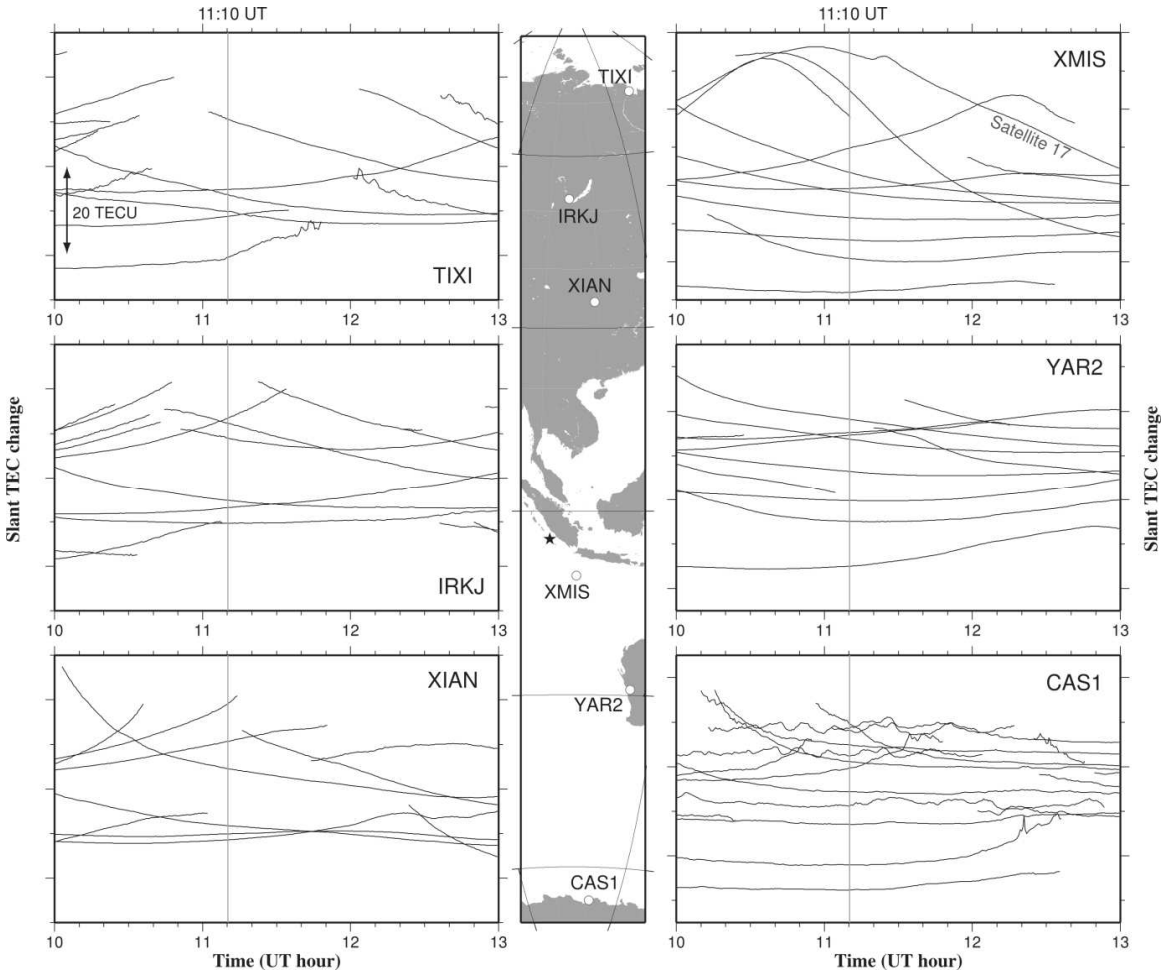


Figure 3.11. Time series 10.00-13.00 UT of raw slant TEC changes observed at the six IGS stations (positions are shown in the center), i.e. TIXI (Russian Arctic), IRKJ (Siberia, Russia), XIAN (China) in the left column, and XMIS (Christmas Island), YAR2 (Western Australia), CAS1 (Casey, Antarctica) in the right column. The gray vertical lines in the time series indicate the occurrence of the 2007 Bengkulu earthquake. The stations were chosen from various latitude zones based on the similarity in longitudes to the earthquake epicenter (black star). Satellite number 17 at XMIS, whose IPP is close to the epicenter, shows a CID signature ~15 minutes after the earthquake. Other stations have no irregularity of TEC except at CAS1 station which shows strong scintillations peculiar to the polar region.

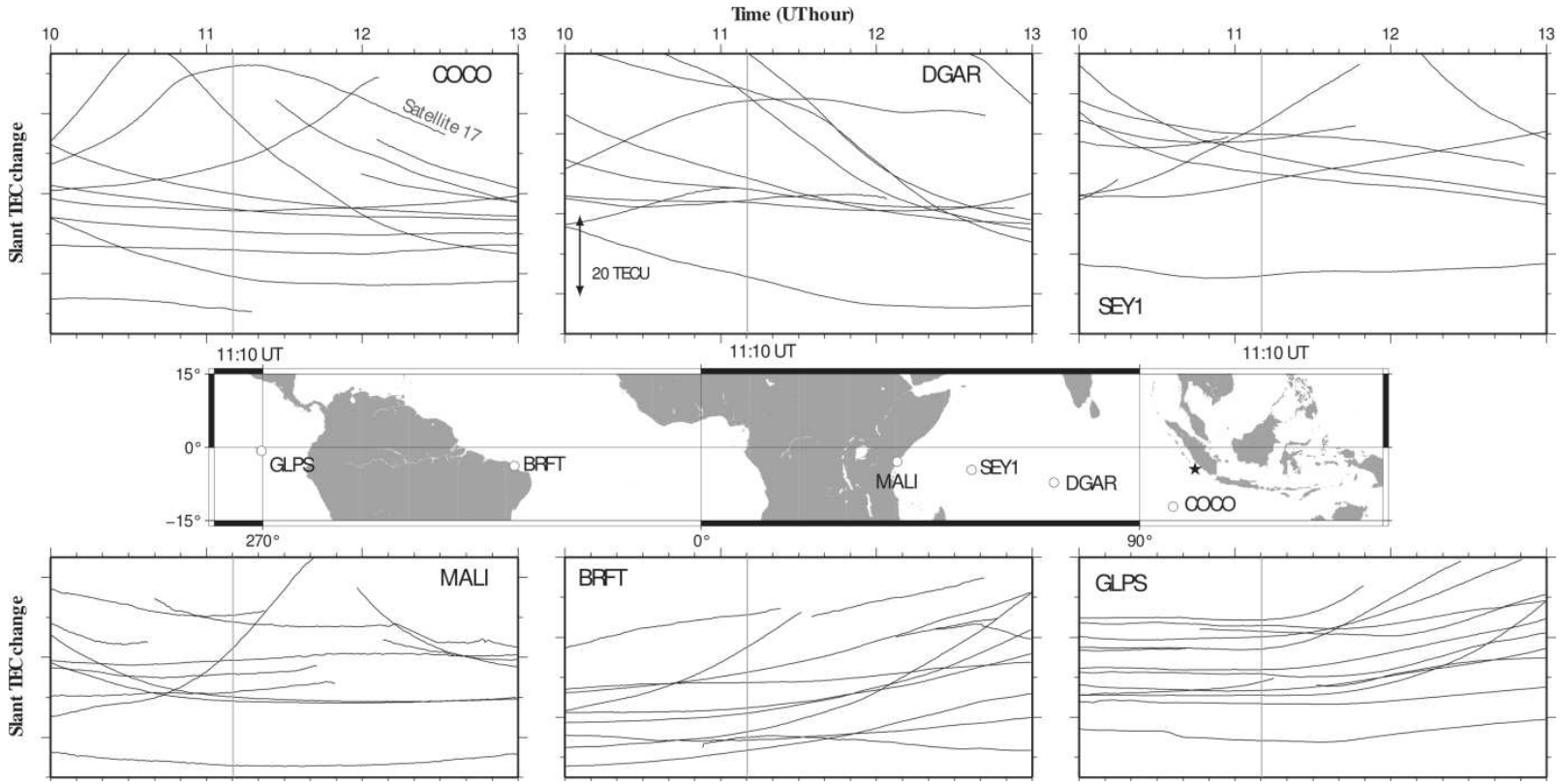


Figure 3.12. Time series 10.00-13.00 UT of raw slant TEC changes observed at the six IGS stations (positions are shown in the center), i.e. TIXI (Russian Arctic), IRKJ (Siberia, Russia), XIAN (China) in the left column, and XMIS (Christmas Island), YAR2 (Western Australia), CAS1 (Casey, Antarctica) in the right column. The gray vertical lines in the time series indicate the occurrence of the 2007 Bengkulu earthquake. The stations were chosen from various latitude zones based on the similarity in longitudes to the earthquake epicenter (black star). Satellite number 17 at XMIS, whose IPP is close to the epicenter, shows a CID signature ~15 minutes after the earthquake. Other stations have no irregularity of TEC except at CAS1 station which shows strong scintillations peculiar to the polar region.

What we should do in the future would be to study as many cases (i.e. mega-thrust earthquakes with available GPS data) as possible. If such anomaly occurred only before a part of these earthquakes (i.e. if some earthquakes are not preceded by short-term TEC anomalies), space weather may have caused them. On the other hand, if such an anomaly preceded every mega-thrust earthquake, it would be unlikely that space weather is responsible for every case.

3.2.4. CID of the largest aftershock

Next we analyze the CIDs of the largest aftershock (M_w7.9) of the 2007 Bengkulu earthquake. It occurred later on the same day (2007/09/12 at 23:49:04 UTC) at the epicenter shown in Figure 3.13. The high-pass filtered (using degree-7 polynomials) slant TEC time series with satellite 21 observed at the samp station are compared with the similar time series at the same site for the main shock (satellite 25) in Figure 3.9a. The CID appeared~10 minutes after this aftershock and was followed by small-amplitude TEC oscillations similar to the mainshock case.

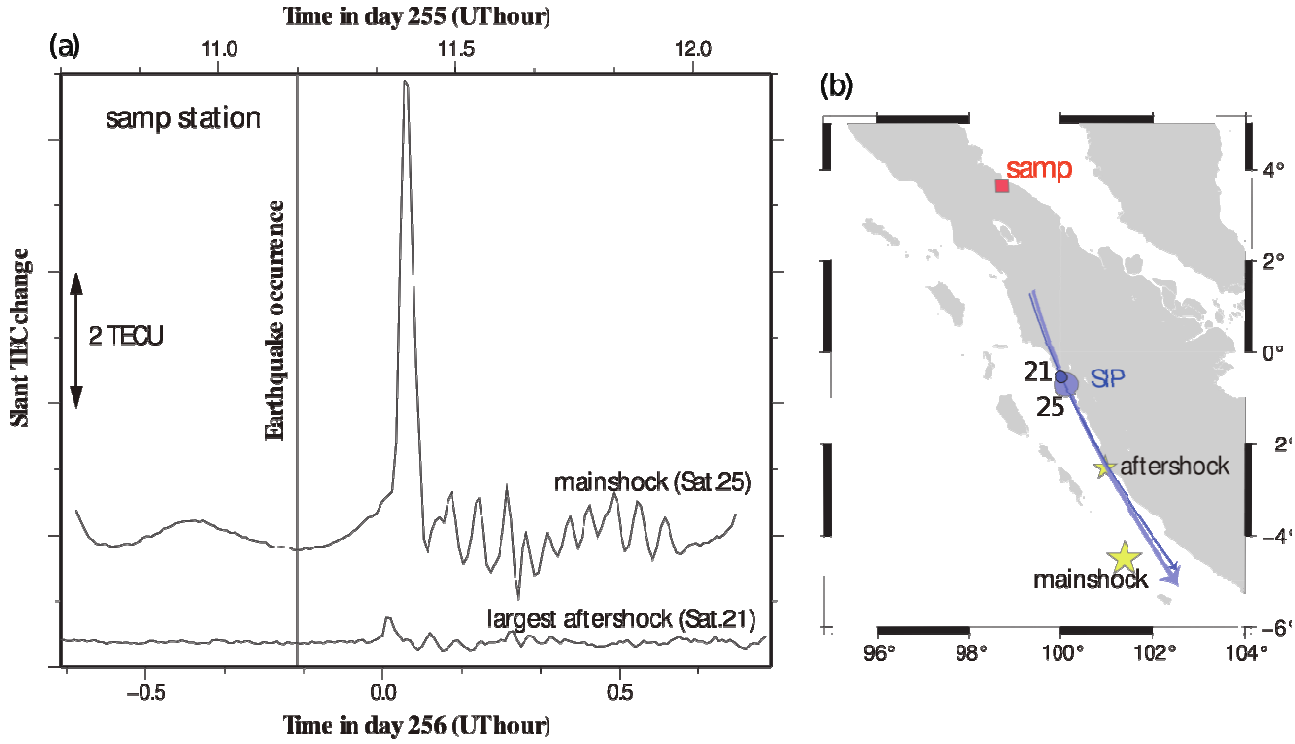


Figure 3.13. (a) Comparison of CIDs between the mainshock (by satellite 25) and the largest aftershock (by satellite 21) at samp station. The tracks of SIP for these satellites are shown in (b). The blue circles indicate the positions at the time of CID arrivals; they are very close to each other. The yellow stars show the epicenters. The difference between the CID amplitudes of the two earthquakes reflects those in magnitudes and the background TEC.

Because of the similarity in the geometry of the station, satellites and epicenters and in the focal mechanisms, they offer a rare opportunity to compare CID amplitudes between the two earthquakes. The mainshock has the peak CID amplitude of ~7 TECU while that of the aftershock is only ~0.3 TECU. Such a large difference cannot be explained only by the difference in magnitude (seismic moment of the aftershock is ~1/10 of the main shock), and would be due also to the difference in the background TEC (~13 TECU for the mainshock and < 2 TECU for the aftershock, see Figure 3.5). Since M_w7.9 is not large enough to show preseismic TEC anomalies (Figure 3.8 inset), we will not discuss them.

3.3. TEC changes in the 2005 Nias Earthquake

Night time ionosphere in equatorial regions often shows strong irregularities due to localized plasma density depletion known as plasma bubbles (*Chu et al.*, 2005; *Li et al.*, 2009). Plasma bubbles often occur after sunset triggered by Rayleigh–Taylor instability, and the probability of their occurrence becomes higher in spring and fall (around equinox) and during periods of high solar activity (*Nishioka et al.,* 2008). Their typical dimension is a few tens of kilometres in the EW direction and extends for thousands of kilometres in the NS direction along the geomagnetic field.

The 2005 March 28 Nias earthquake (M_w8.6) was a little larger than the 2007 Bengkulu earthquake (M_w8.5). However, it occurred in the night time (23:09 in local time), one week after the vernal equinox, and before solar cycle 23 ended. These points suggest high probability of plasma bubble occurrences. Figure3.10a shows the raw slant TEC behavior 11-21 UT on the day of the 2005 Nias earthquake observed at the lewk station, the Simeulue Island (Figure 3.14b). There we can see lots of quick decreases and increases, indicating the intersection of the line-of-sight measurements with plasma bubbles. Figure 3.10c compares the TEC changes during the same 3-hours periods over five consecutive days before and after the 2005 Nias earthquake. It is interesting to see that they occurred not only on the day of the earthquake (day 087) but also on the days before (day 086) and after (day 088) the earthquake. This suggests that the observed plasma bubbles are not related to the earthquake, but represent the normal behaviours of equatorial ionosphere in this time and season.

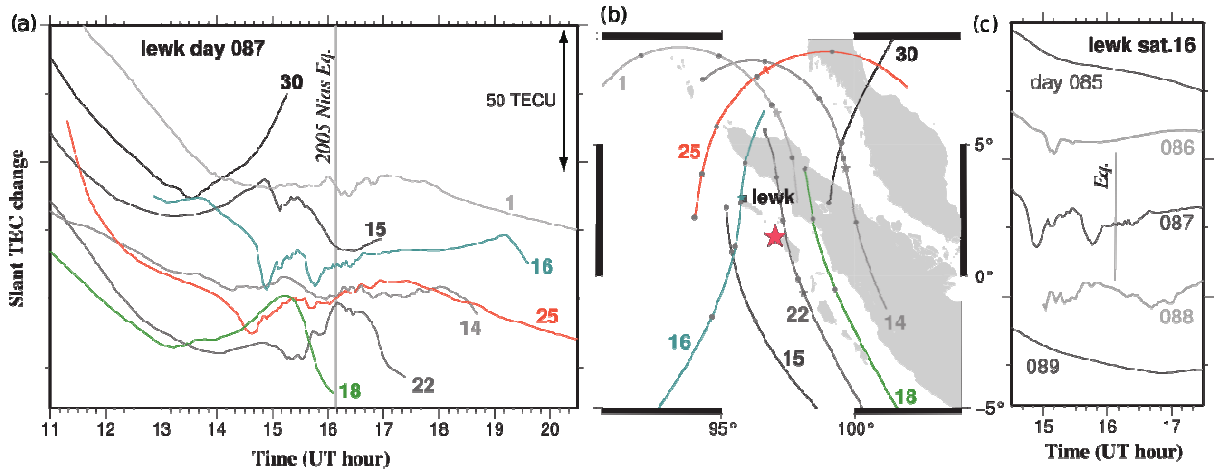


Figure 3.14. (a) Time series 11-21 UT of slant TEC changes observed at the lewk station. The plasma bubble signatures are severe around the black vertical line indicating the occurrence of the 2005 Nias earthquake (day 087, 16:09 UT). (b) Trajectories of SIP seen from the lewk station for the satellites shown in (a). On the trajectories, small black stars are SIP at 16:09 UT. The large red star denotes the epicenter. In (c) are shown slant TEC changes over five consecutive days (days 085-089) obtained with satellite 16 from the lewk station. There the vertical axis is same as (a).

Because plasma bubbles cause rapid changes in TEC much larger in amplitudes (tens of TECU) than earthquake-generated signals (a few TECU), neither coseismic nor preseismic ionospheric disturbances can be recognized clearly. It is interesting to see that plasma bubble did not occur two days before (day 085) and after (day 089) the earthquake. TEC data immediately before and after the 2005 Nias earthquake are not suitable for any analyses of disturbances related to the earthquake.

Chapter 4

Coseismic ionospheric disturbance of the 2012 North Sumatra earthquakes, large intra-plate strike-slip events

(Cahyadi and Heki,*Geophysical Journal International*,Under Review)

4.1 Introduction

After the 2004 Sumatra-Andaman earthquake, two large earthquakes occurred near Sumatra, i.e. the 2005 Nias (M_w8.6) and the 2007 Bengkulu (M_w8.5) earthquakes. *Cahyadi and Heki* (2013) studied CIDs of the latter with GPS, but found that severe plasma bubble activities masked the CID of the former (see Chapter 3). They used GPS data from ~20 continuous GPS stations of the Sumatra GPS Array (SUGAR) operated by the Tectonics Observatory of Caltech and the Indonesian Institute of Sciences (LIPI) as describe on data processing chapter 2.1. In this research, I also use the SUGAR data together with those from several IGS (International GNSS Service) stations. Considering the unique focal mechanism of the 2012 North Sumatra earthquakes, it would be interesting to compare their CID with those of past earthquakes dominated by dip-slip faulting mechanisms.

On 11 April, 2012, an M_w 8.6 intra-plate earthquake occurred ~400 km off the Indian Ocean coast of Northern Sumatra, Indonesia (2.31N, 93.06E, focal depth 23 km), at 8:38:37 UT (*Meng et al.*,2012). The largest aftershock (M_w 8.2) occurred ~2 hours later (10:43:09 UT) ~200 km southwest of the main shock (0.77N, 92.45E, focal depth 16 km). The main shock had a complex source process, *i.e.* ruptures of strike-slip mechanism occurred one after another during 160 seconds on four different sub-faults with a relatively slow rupture velocity (*Yue et al.*, 2012). This was the largest strike-slip earthquake ever recorded. Owing to relatively small vertical coseismic crustal movements for strike-slip earthquakes, tsunami height of this earthquake did not exceed one meter.

In this research, I investigate the CID of this earthquake using the SUGAR data together with those from several IGS (International GNSS Service) stations. Considering the unique focal mechanism of the 2012 North Sumatra earthquakes, it would be interesting to compare their CID with those of past earthquakes dominated by dip-slip faulting mechanisms.

4.2 TEC changes before and after the 2012 North Sumatra earthquake

Figure 4.1a shows slant TEC changes observed at the Port Blair (pbri) station, in the Andaman Islands,~1000 km north of the epicenter, during 07:30-12:00 UT on April 11, 2012. Slant TEC shows U-shaped temporal changes due to the apparent movement of GPS satellites in the sky (and consequent changes of the penetration angles of LOS to the ionosphere). When *Cahyadi and Heki* (2013) studied CIDs of the 2007 Bengkulu earthquake, sampling intervals of the SUGAR stations (2 minutes) were not sufficiently short for studies of CID whose typical time scale is 4-5 minutes. In the 2012 data set, however, most stations employed the sampling interval short enough for such studies(15 seconds).

The coordinates of the ionospheric piercing points (IPP) of LOS were calculated assuming a thin ionosphere at altitude of 300 km, and the trajectories of their ground projections (sub-ionospheric points, SIP) are plotted on the map in Figure 4.1b. The SIPs of Satellites 3 and 6werearound the middle point between the epicenter and the site when the main shock occurred. In Figure 4.1a, CIDs are visible 10-15 minutes after the main shock even in the raw slant TEC plots for Satellites 3 and 6. The largest aftershock occurred ~2 hours later, and TEC with Satellite 11 shows a clear CID signature.

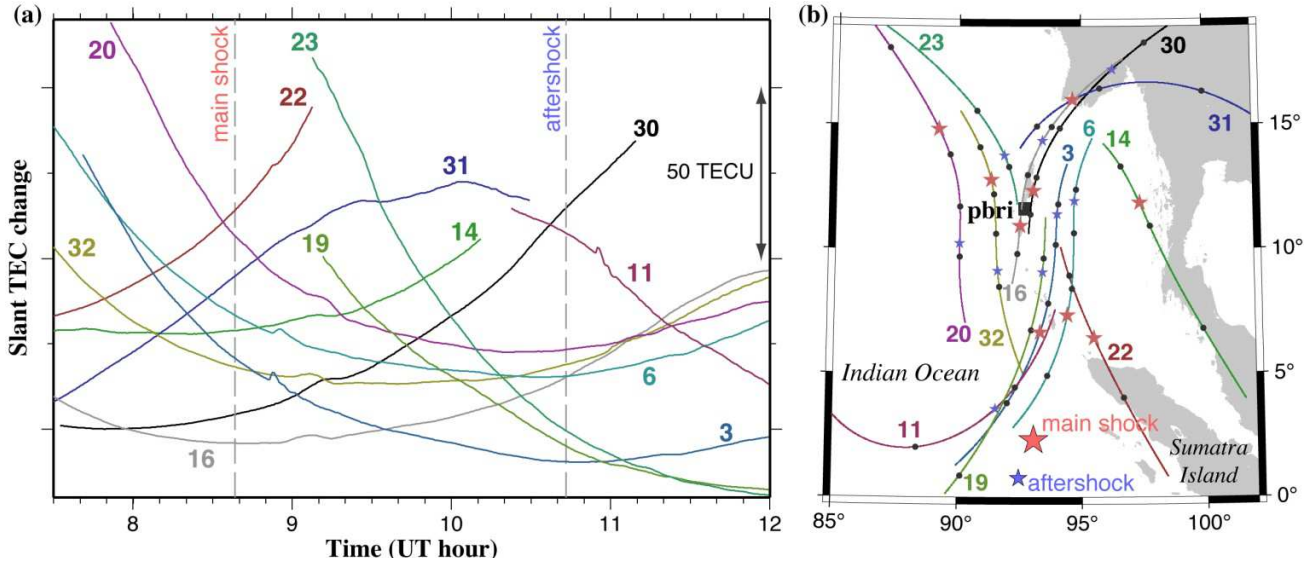


Figure 4.1. (a) Time series 07.30–12.00 UT of slant TEC changes observed at the pbri (Port Blair, the Andaman Islands) station (position shown in b) with twelve GPS satellites. Arbitrary biases are added to individual satellites. The two gray dashed vertical lines in (a) indicate the occurrence of the main shock and the largest aftershock of the 2012 North Sumatra earthquake (08:38 and 10:43 UT). CIDs are seen for some of the satellites ~10-15 minutes after the earthquakes. (b) Trajectories of SIP for GPS satellites with hourly time marks (small black dots). On the trajectories, I show SIP positions at 08:38 and 10:43 UT with red and blue stars, respectively. The large red and blue stars are the epicenters of the main shock and the largest aftershock, respectively.

Slant TEC time series include long period components coming mainly from the apparent motion of satellites (U-shaped changes), and partly from latitudinal difference of ionization and slow diurnal change of vertical TEC. I need to eliminate them with a high-pass filter. Here I estimated the best-fit polynomial with degree three for vertical TEC and subtracted its contributions from the raw data (*Ozeki and Heki*, 2010; *Heki*, 2011). I excluded 20 minutes period (from the earthquake until 20 minutes after the earthquake) to avoid parts affected by CIDs in the estimation of the polynomial coefficients. Anomalies of slant TEC shown in Figure 4.2a,c have been derived as the deviations from these reference curves. Accurate conversion from L4 (slant TEC plus biases) to vertical TEC by removing phase ambiguities and inter-frequency biases needs sophisticated algorithms (*e.g.*Sardón *et al.*, 1994).The simple method by *Ozeki and Heki* (2010) is employed here in order to model background TEC changes of a specific satellite with relatively small number of parameters, rather than to obtain accurate vertical TEC.

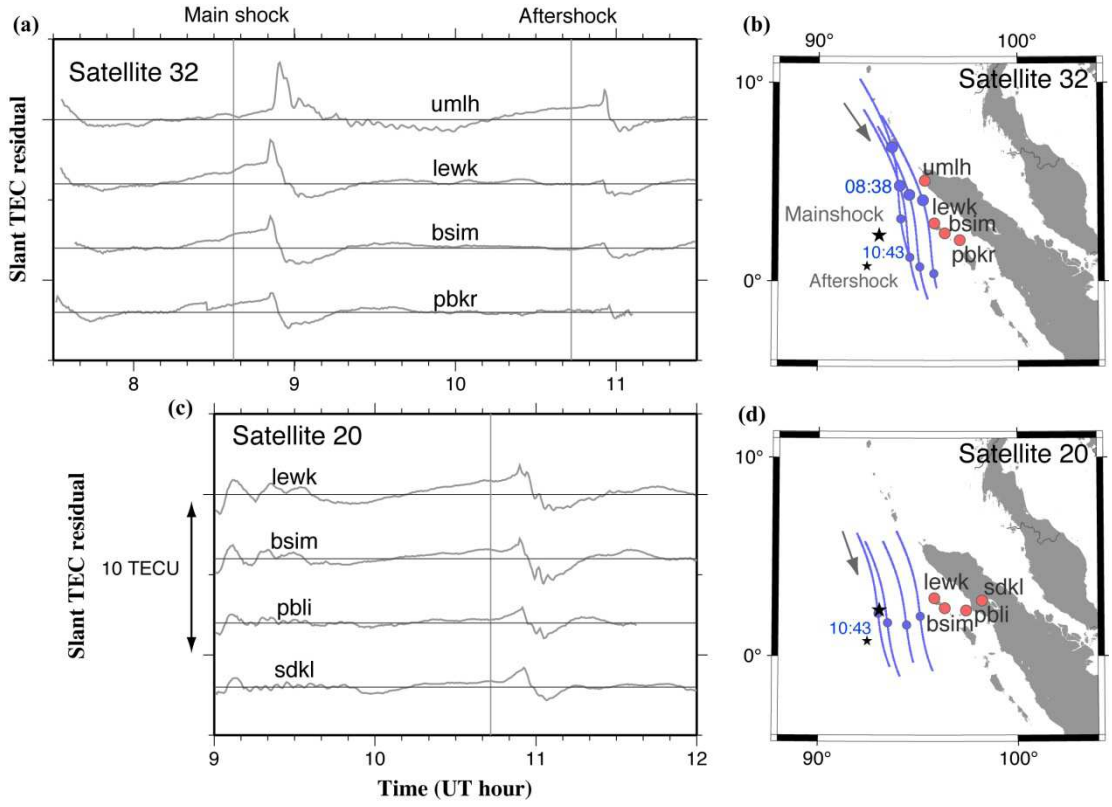


Figure 4.2. Slant TEC anomalies recorded at four GPS stations with Satellites 32 (a), and 20 (c). The scale for 10 TECU shown in (c) applies also for (a). Vertical gray lines are occurrence times of the main shock (08:38 UT) and the largest aftershock (10:43 UT) of the 2012 North Sumatra earthquake. Reference curves are derived by modeling vertical TEC changes with cubic polynomials of time, and residuals shown here are the differences from the reference curves. I excluded 20 minutes intervals after earthquakes (08:38-08:58 and 10.43-11:03) in deriving the reference curves. Trajectories of SIPs are shown in (b) and (d).Small and large blue circles on the trajectories are SIPs at 08:38 and 10:43 UT respectively.

Figure 4.2 highlights CID, *i.e.* N-shaped TEC disturbances appearing 10-15 minutes after the main shock with amplitudes of a few TECU. Another CID appeared again after the largest aftershock. These signatures are similar to the case of the 2007 Bengkulu earthquake in southern Sumatra (*Cahyadi and Heki*, 2013). These CIDs can be understood as the ionospheric response to propagating shock-acoustic waves (*Afraimovichet al*., 2001). For the ulmh station data with Satellite 32, TEC showed monochromatic oscillation after the N-shaped disturbances and returned to normal. In this research, I discuss the initial TEC disturbances and the monochromatic oscillation in Section 4.3.2 and 4.3.3. Stations shown in

Figure 4.2 have SIPs to the northeast of the epicenter. In Section 4.3.4, I show that the CIDs have propagated mainly northward from epicenters. Comparative studies of CID amplitudes of various earthquakes will be done in Section 4. I also examine the existence of preseismic TEC enhancement immediately before earthquakes, which will be discussed in Section 4.5.

4.3. Near-fieldCID ofthe 2012 NorthSumatraEarthquake

4.3.1 Coseismic vertical crustal movements

Near-field CIDs are excited by coseismic vertical crustal movements. Figure 4.3 shows coseismic vertical crustal movements calculated using fault parameters inferred seismologically. Actually, I used geometry and seismic moment of fault segments in Figure 4.4 of *Yue et al.*,(2012). I assumed uniform slips over individual fault segments, and calculated the slips from seismic moments using the rigidity of 50 GPa. I then used the Green's function for an elastic half space (*Okada*, 1992). The CIDs I found in this study would have been excited by vertical movement of the ocean floor (and hence sea surface) as shown in Figure 4.3. In the Figure 4.10, I show that even a pure strike-slip earthquake causes certain amount of vertical crustal movements (~1/5 of a dip-slip earthquake of the same magnitude).

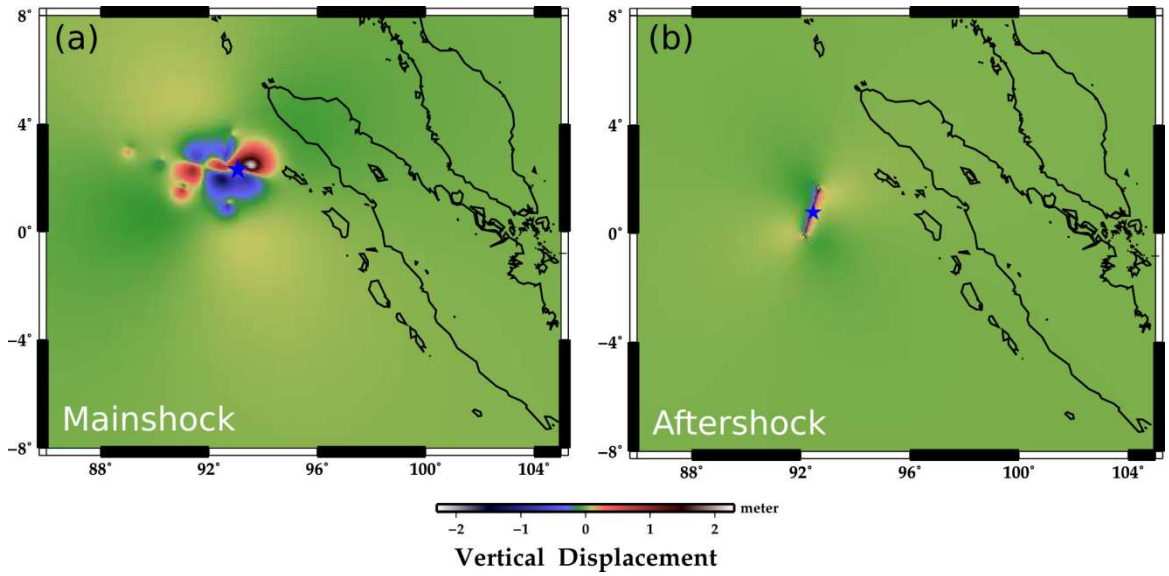


Figure 4.3. Vertical crustal movements of the main shock (a) and the largest aftershock (b) of the 2012 North Sumatra earthquake. Blue stars show the epicenters of the two earthquakes. They were calculated after Okada(1992), using the fault geometry taken from Figure 4 of Yue *et al.*,(2012). Average slips of the four fault segments were inferred from the seismic moments released from the fault segments given there. Although the earthquakes were dominated by the strike-slip mechanism, significant vertical movements occurred. Focal distances in the vertical axes of Figure 4 are measured from the centers of uplift in this figure.

4.3.2 Propagation speed

CIDs are caused by several different atmospheric waves. Ionosphere responses to acoustic waves appear first above epicenters 10-15 minutes after the main shock. The near-field CIDs caused by direct acoustic waves from epicenters propagate as fast as ~0.8-1.0 m/s, sound speed at the height of the ionospheric F region. *Astafyeva et al.*,(2009) found that CID of the 1994 Hokkaido-Toho-Oki earthquake has two separate components with different propagation speeds. The faster components (~4 km/s) are excited by the Rayleigh surface waves, and propagate farther than those by the direct acoustic waves owing to smaller geometric decay (*Rolland et al.*, 2011a). Earthquakes accompanying large tsunamis often show much slower components (~0.3 km/s) caused by internal gravity waves (*e.g.Tsugawa et al.*, 2011).

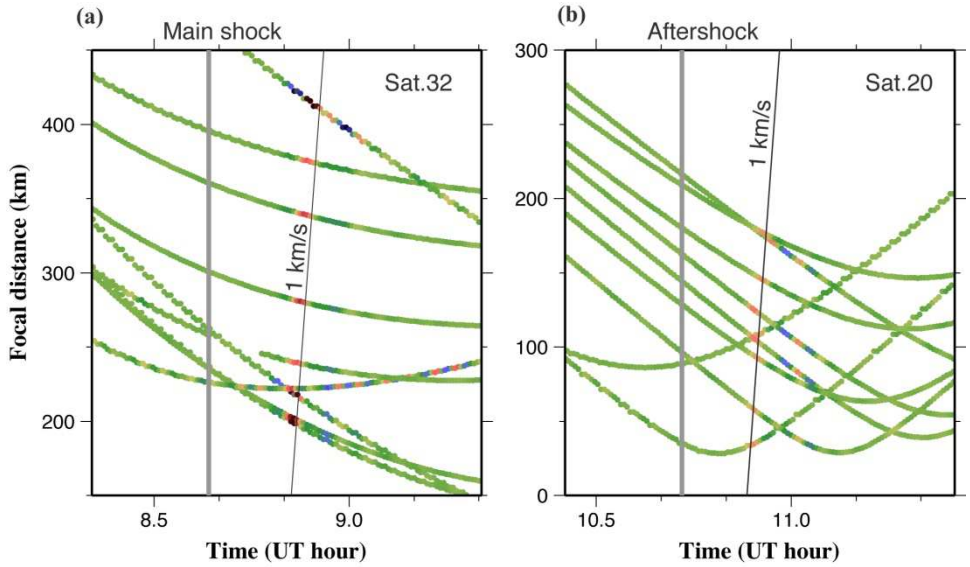


Figure 4.4.(a) Travel-time diagram of the CID after the 2012 North Sumatra earthquake (main shock) based on the Satellite 32 data. The CID peak (shown in red colors) detected by wavelet propagates with the apparent velocity of ~1 km/s (thin black line). Distances are measured from the center of the uplift (Fig.3a). The gray vertical line indicates the occurrence of the main shock (08:38 UT). (b) Travel-time diagrams of the largest aftershock CID based on the Satellites 20 data. Distances are measured from the center of uplift (Fig.3b). The gray vertical line indicates the occurrence of the aftershock (10:43 UT). Apparent speed is also ~1 km/s. In both cases, only stations with SIP to the north of the epicenter (i.e. with latitudes higher than the uplift centers) are plotted considering the directivity (Fig.6).

To study the propagation speeds of the CID seen in Figure 4.2, I plot the focal distance as a function of time and showed TEC changes with colors in Figure 4.4a (main shock) and 4.4b (the largest aftershock). To isolate oscillatory changes with periods of ~4 minutes from TEC time series, I used the wavelet analysis procedure following *Heki and Ping* (2005). The propagation speeds after both events were consistent with the sound speed in the F region, ~1 km/sec.

4.3.3 Resonant oscillations

Acoustic resonance in 3.7 mHz and 4.4 mHz is found in the Earth's background free oscillation (*Nishida et al.*, 2000), and these frequencies were identified in postseismic monochromatic TEC oscillation by GPS-TEC after the 2004 Sumatra-Andaman earthquake

(*Choosakul et al.*, 2009), the 2011 Tohoku-oki earthquake (*Saito et al.*, 2011; *Rolland et al.*, 2011b), and the 2007 Bengkulu earthquake (*Cahyadi and Heki*, 2013). I show spectrograms obtained by the Blackman-Tukey method using the TEC time series after the main shock and the largest aftershock in Figure 4.5. The observed peak frequencies were ~4 mHz. This is consistent with the atmospheric resonance frequencies, but relatively short time windows (1 hour in both cases) did not allow more detailed studies, *e.g.* which of the two frequencies is closer to the observations.

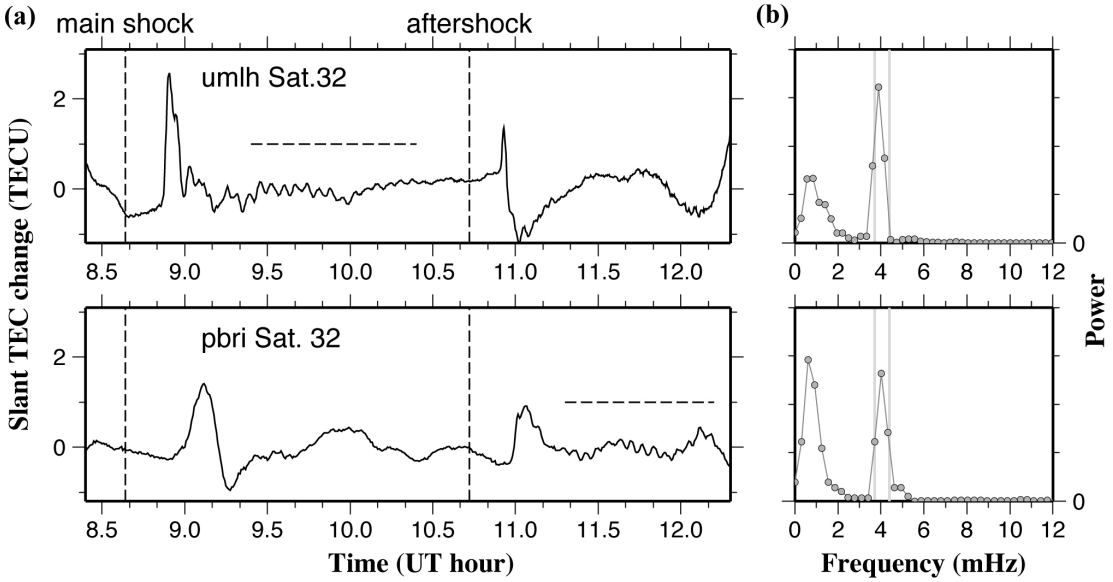


Figure 4.5. The TEC time series at umlh (Fig. 2b) and pbri (Fig.1b) with Satellite 32 show monochromatic oscillation lasting over an hour after the main shock and the largest aftershock, respectively (a). Their spectrograms (b) show peaks around4 mHz, close to the two atmospheric resonance frequencies3.7 mHz and 4.4 mHz shown as two vertical lines(*Nishida et al.*, 2000). Horizontal dashed lines in (a) show time windows for the spectral analyses.

The visibility of resonant oscillation with TEC would depend on several factors, *e.g.* areal extent of the occurrence of the oscillation and the incident angle of the LOS with the wavefront. The movement of the neutral atmosphere should also have components parallel with the ambient geomagnetic field in order that the electron may oscillate together

(*Rollandet al.*, 2011a). Hence, site-satellite pairs showing clear resonant oscillations in TEC need to satisfy all these conditions. Clear signature for the aftershock at pbri with Satellite 32 shows that the oscillation occurred at least ~500 km north of the epicenter. However, the oscillation signature was not detectable from pbri after the main shock, when the SIP was ~1000 km apart from the epicenter (Fig.4.1b).

4.3.4 Directivity of CID

Heki and Ping (2005) investigated the N-S asymmetry of CIDs of the 2003 Tokachi-oki earthquake, Japan, *i.e.* they propagated little toward the north, and attributed it to the geomagnetic field. If particle motions of neutral atmosphere in the F region are perpendicular to the magnetic field, electrons would not move together with neutral particles and the CID would be suppressed. In the mid-latitude region of the northern hemisphere, this happens to the north of the epicenter. Recently, *Rolland et al*. (2013) mapped the CID amplitudes and polarities around the epicenter of the 2011 Van earthquake, Turkey. Although *Heki and Ping* (2005) explained the directivity only in a qualitative manner, *Rolland et al.* (2013) succeeded in reproducing such N-S asymmetry with a realistic simulation.

Although the 2012 North Sumatra earthquakes occurred in the northern hemisphere in geographic latitude, their epicenters are located to the south of the magnetic equator. According to the international geomagnetic reference field (*IAGA 2010*), geomagnetic inclinations above the epicenters of the main shock and the largest aftershock are −14.2 and −17.8 degrees, respectively. Thus it should have the directivity opposite to the northern hemisphere, *i.e.* southward CID is to be suppressed. However, such northward directivity in the southern hemisphere has never been confirmed clearly with real GPS data.

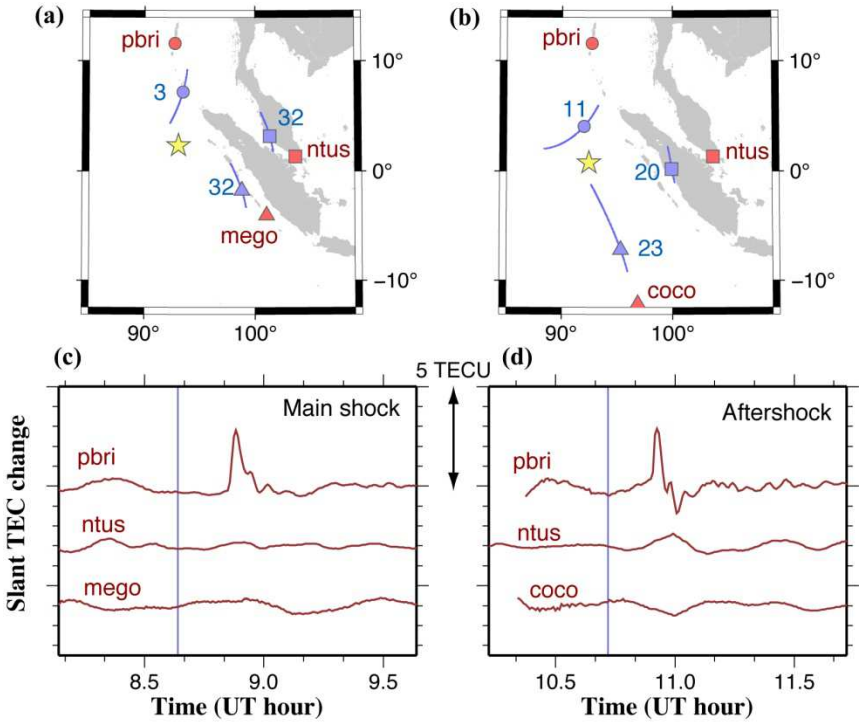


Figure. 4.6 Comparison of the CID of the main shock (a) and the largest aftershock (b) of the 2012 North Sumatra earthquake propagating toward three directions. Their TEC time series are shown in (c) and (d) for SIPs located to the north (top), east (middle) and south (bottom). I selected satellite-site pairs with geometries of the epicenter (yellow), SIP (blue), GPS station (red) favorable for CID detections (see Fig.4.7). Strong CIDs are seen only to the north of the epicenter. Numbers attached to the SIPs in (a, b) are satellite numbers.

Figure 4.6 compares TEC time series showing CIDs propagating northward, eastward, and southward, for the main shock (a, c) and the largest aftershock (b, d) of the 2012 North Sumatra earthquake. I used different satellites to realize shallow penetration angle of LOS to the acoustic wavefront (discussed in detail in Section 4.4.2). In both of the earthquakes, Figure 4.6 clearly shows that the strong CIDs are seen only to the north of the epicenter.

4.4. Comparison With Other Earthquakes

4.4.1. CIDs of 21 earthquakes of various focal mechanisms

Near-field CIDs are caused by acoustic waves excited at the surface by coseismic vertical crustal movements. A larger earthquake causes larger crustal deformation and a larger CID. If we know the relationship between them, we could infer earthquake magnitudes from CID amplitudes immediately after acoustic waves arrived at the F region (~10 minutes after the earthquake). In the 2011 Tohoku-oki earthquake, the largest tsunami height occurred >20 minutes later than the earthquake (see, *e.g.Mitsui and Heki*, 2013). In such a case, earthquake magnitudes inferred from CID amplitudes in an early stage may contribute to the disaster mitigation.

Here I collected 21 earthquakes with clear CIDs detected by GPS observations (*e.g.* GEONET in Japan, SUGAR, and IGS networks). Their moment magnitudes range from 6.6 to 9.2. The largest event is the 2004 Sumatra-Andaman earthquake. The smallest earthquake with successful CID detection is the 2007 M_w6.6 Chuetsu-oki earthquake, central Japan, and its TEC data are shown in the Figure 4.7. The 21 earthquakes include two normal fault earthquakes that occurred in the outer rise region of the trenches (2007 January central Kuril, and 2012 December Tohoku-oki), and two strike-slip earthquakes, i.e. the main shock and the largest aftershock of the 2012 North Sumatra earthquakes. The others are all reverse earthquakes.

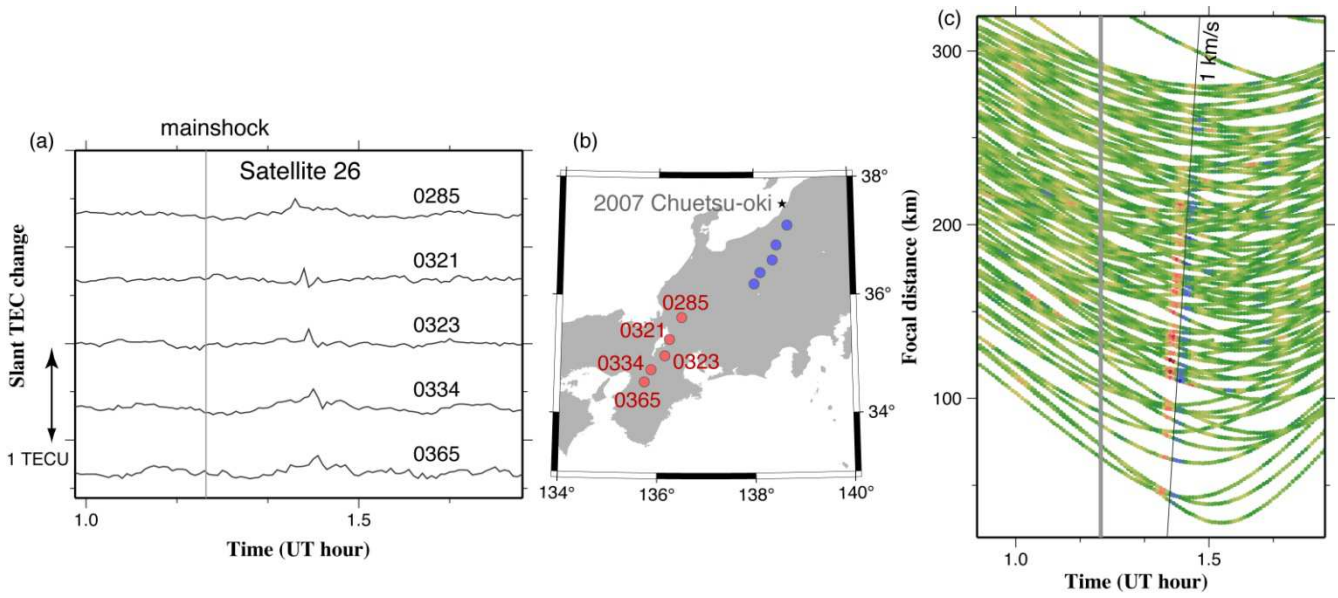


Figure 4.7. CID of the 2007 July 16 Chuetsu-oki earthquake (M_w6.6) observed with Satellite 26. This was the smallest earthquake whose CID clearly detected with GPS. Time series of TEC changes at five stations (a), positions of GPS stations and their SIPs (b), and travel time diagram drawn using the same wavelet analyses as in Figure 4.4 (c).

Some of the examples have been already reported in past literatures. They include the 2004 Sumatra-Andaman earthquake (*Heki et al.*, 2006), the 2011 Tohoku-oki earthquake (*e.g.*Astafyeva *et al.* 2011), the 2007 Bengkulu earthquake and its largest aftershock (*Cahyadi and Heki*, 2013), the 2006 and 2007 Central Kuril earthquakes (*Astafyeva and Heki*, 2009), the 2004 Hokkaido-Toho-oki earthquake (*Astafyeva et al.*, 2009), the 2003 Tokachi-oki earthquake (*Heki and Ping*, 2005), 2004 Kii-Hanto-oki foreshock (*Heki and Ping*, 2005), 2008 Wenchuan earthquake (*Afraimovich et al.*, 2010), 2009 New Zealand and 2006 Tonga earthquakes (*Astafyeva et al.*, 2013). Other examples are newly analyzed in this study. Their moment magnitudes are taken from the Harvard CMT solutions (www.globalcmt.org). The focal depth ranged from 55 km to 6 km (Figure 4.10c).

There are three types of earthquake faulting, i.e. normal, reverse, and strike-slip. The first two cause larger vertical crustal movements than the third. Hence, it is important to know both magnitude dependence and focal mechanism dependence of CID amplitudes. The 2012

North Sumatra earthquake was the largest strike-slip earthquakes ever recorded, and it is a good opportunity to discuss this point.

Astafyeva et al.(2013) also compiled 11 earthquakes with clear CID observations, and investigated the correlation between M_w and CID amplitudes. The three distinct differences of our study from *Astafyeva et al.*(2013) is that (1) I discuss all the three mechanism earthquake while they discussed only thrust (low-angle reverse) earthquakes, (2) number of earthquakes discussed is nearly twofold, and (3) I discuss CID amplitude relative to background vertical TEC while they discussed amplitudes of absolute TEC changes. The third point will be discussed in Section 4.3.

4.4.2. Geometry problem

In these 21 cases, I tried to select the pair of GPS satellite and station showing the largest CID amplitude. Due to the directivity, the SIP should be on the southern/northern side in earthquakes in the northern/southern hemisphere. As shown in the numerical simulation by *Rolland et al.* (2013), the directivity is not so sharp, *i.e.* CID amplitudes remain similar for the azimuths within ~20 degrees from the main beam direction. Figure 4.8 shows ideal geometry of SIPs, epicenters and GPS receivers. Although the zenith angle of LOS at IPP (z in Fig.4.8) governs the ratio between vertical and slant TEC values, it is the CID wavefront penetration angle (θ in Fig. 4.8) that controls the CID amplitude. To achieve small θ, the receiver should be (1) on the same side of the epicenter as the SIP, and (2) farther from the epicenter than SIP. Such geometry is important because it enables shallow LOS penetration with the CID wavefront.

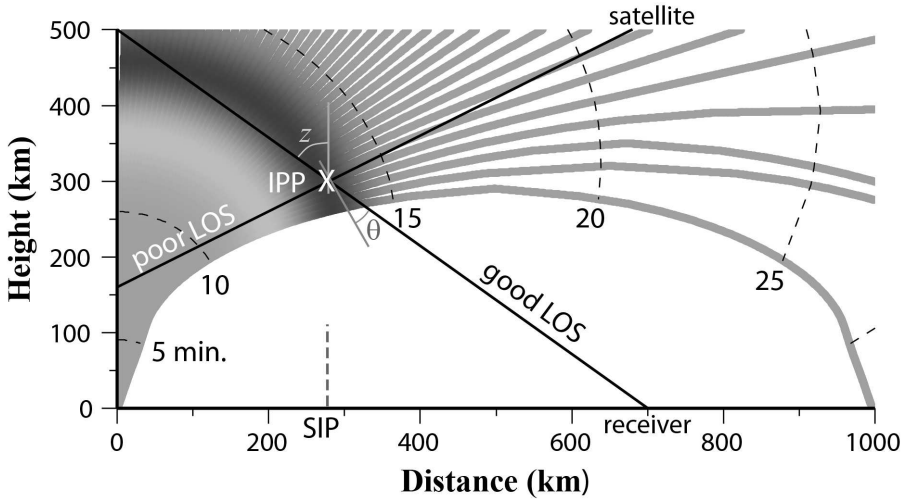


Figure 4.8. Ray tracing of atmospheric sound waves adopted from the Figure 7 of *Heki and Ping*(2005). Black and white wave fronts show the compression and rarefaction part of the wave at 12.5 minutes after the earthquake. A good LOS captures sharp waveform of the CID but poor LOS does not because it penetrates both black and white parts simultaneously. The SIP and GPS receiver lying on the same side of the epicenter result in small θ, the angle between the CID wavefront and the LOS, and clear CID observations. The zenith angle *z*, on the other hand, does not significantly influence the CID amplitudes. Equal-time contours are shown every 5 minutes with broken curves.

Actual geometry of epicenter, SIP, and GPS stations for the 20 cases are shown in Figure 4.9. This figure does not include the 2008 Wenchuan earthquake because the raw GPS data file of the luzh station, China, was not available. Figures in *Afraimovich et al.* (2010) suggest that its geometric condition was good, and I read the CID amplitude of this earthquake from Fig.S1c of *Astafyeva et al.*(2013).

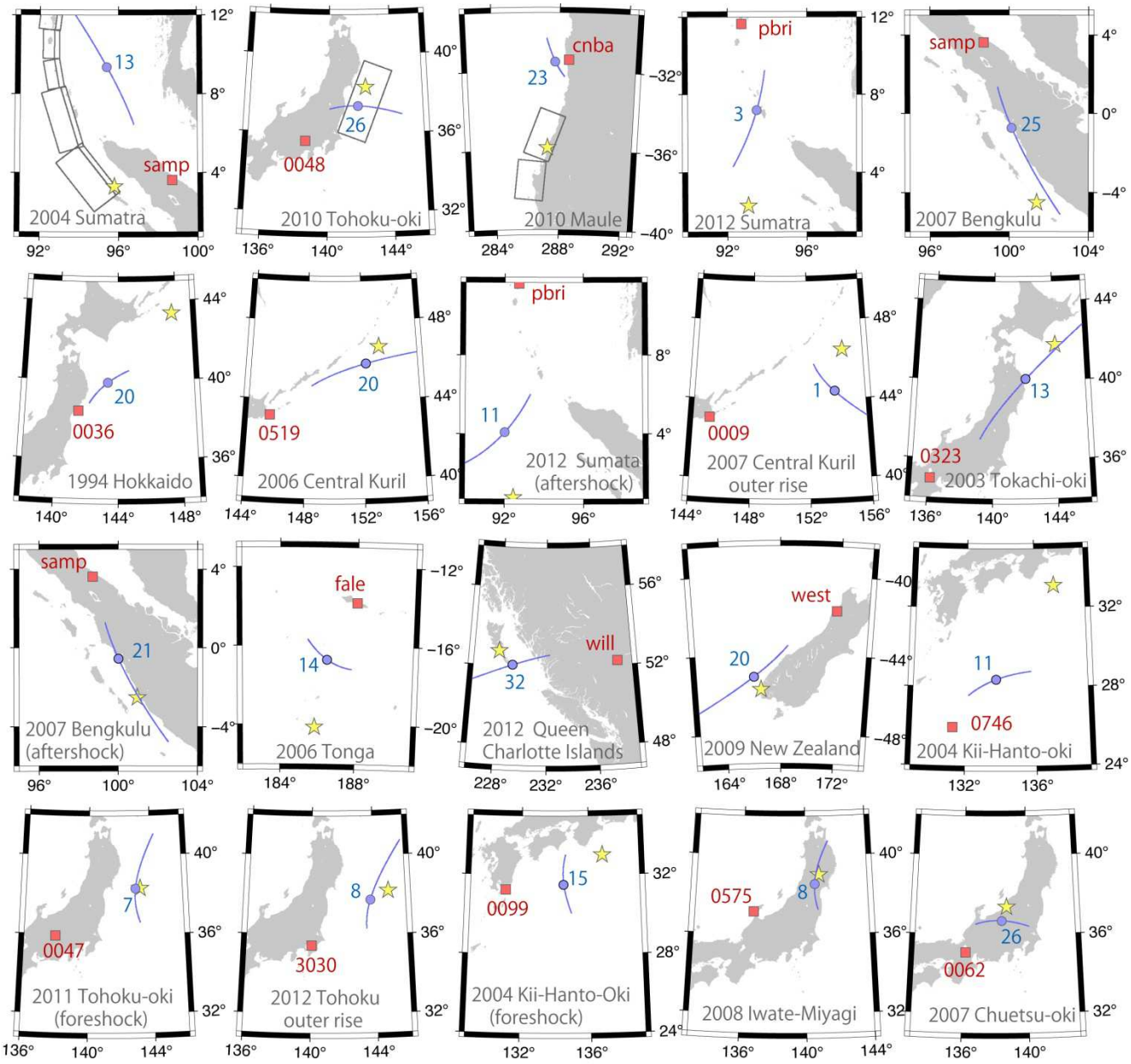


Figure 4.9. Geometry of epicenter (yellow star), SIP at the time of CID occurrence (blue circle), and GPS receivers (red square) for the 20 examples of CID observations given in Fig.4.10. They are displayed in a descending order of magnitudes. Blue curves are SIP trajectories in the time window shown in Fig.4.10. For the three M9-class earthquakes, approximate shapes of faults are shown by rectangles.

The largest factor influencing CID amplitudes would be the earthquake magnitude. In fact, the seismic moment of an M7 event and an M9 event is different by three orders of magnitude. Apart from the magnitude, two important geometric factors would be the distance between SIP and epicenter and the angle between wavefront and LOS(θ in Fig. 4.8). To

isolate magnitude dependence by minimizing the geometric differences, I tried to find the satellite-site pair satisfying the two conditions, i.e. they should show CID with (1) appearance time not later than 15 minutes after earthquakes, and (2) sharp peaks. The first criterion ensures that SIPs are close to the epicenters and geometric decays are not significant. The second condition is the manifestation of the shallow angle penetration of LOS (small θ in Fig.4.8).

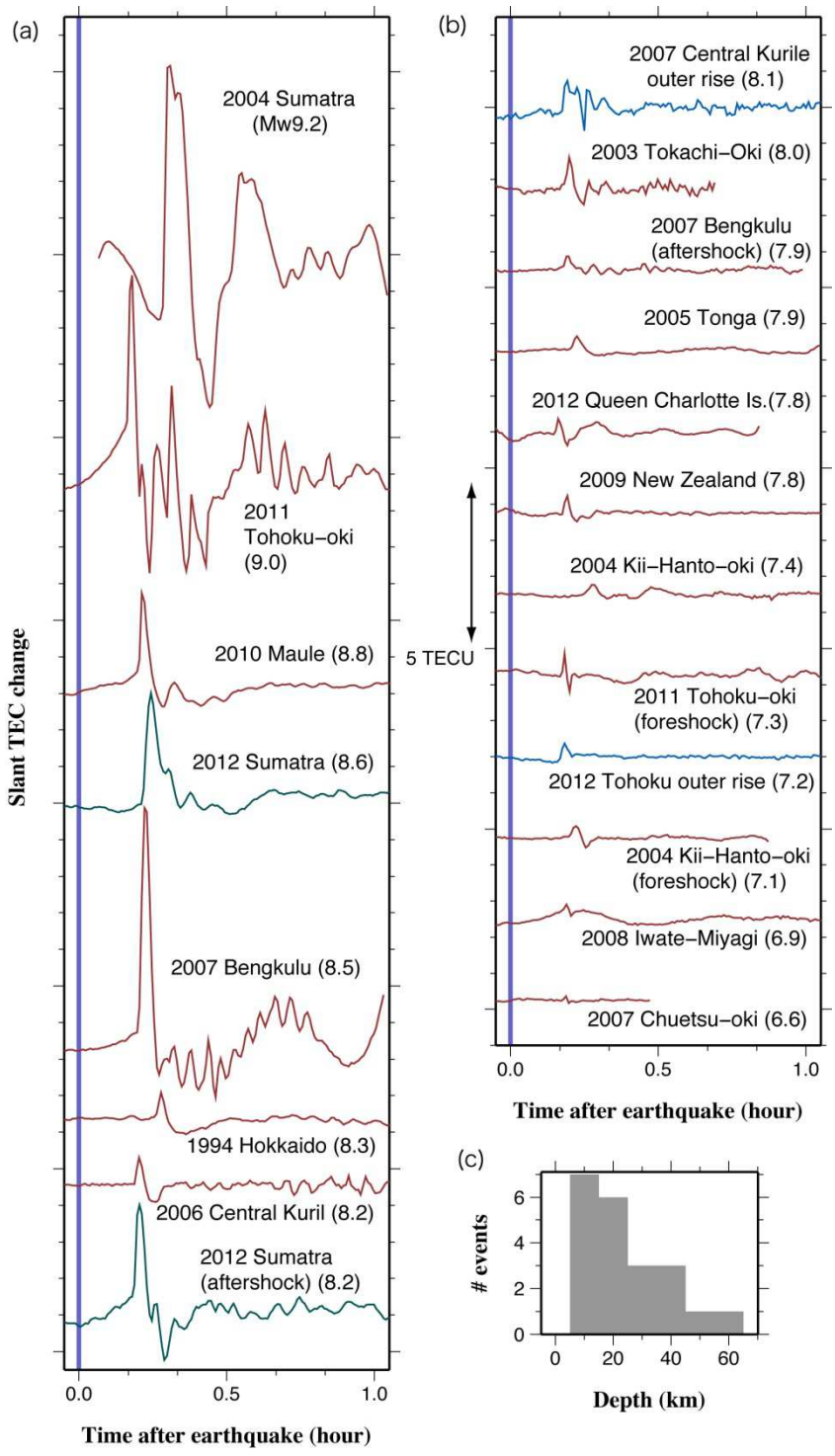


Figure 4.10. TEC time series showing 20 examples of CID observations in the time window from −0.5 to 1.05 hours for earthquakes with magnitudes 9.2-8.2 (a) and 8.1-6.6 (b). Moment magnitudes are shown within the parentheses. Colors of the curves show reverse (red), normal (blue), and strike-slip (green) mechanisms. Distribution of the focal depths is shown as a histogram in (c).

Their TEC time series are shown in Figure 4.10. There a simple high-pass filter (subtraction of the best-fit polynomials with degrees up to six) was applied to raw slant TEC time series. The ideal geometry may not be always realized. For example, earthquakes sometimes occur in the Nankai Trough off the Pacific coast of SW Japan (*e.g.* the 2004 Kii-Hanto-oki earthquakes). Their CIDs are difficult to observe with GEONET because few stations exist to the south of the Nankai Trough. In such a case, I have to use a somewhat blunt peak. I did not include an earthquake for which I did not find a pair showing CID appearing within 15 minutes with a sharp positive peak. For example, I could detect faint CID for the 1999 Chi-chi earthquake, Taiwan, from SW Japan, but it suffered from attenuation due to large distance from the epicenter and high angle between LOS and wavefront. So I did not include it in the discussion. In order to facilitate further investigation, I provide a table in the Table 4.1 and give key quantities, e.g. distance between SIP and the epicenter, distance between SIP and the GPS station.

In the case of the 2003 Tokachi-oki earthquake, Satellites 13 and 24 both satisfies the criteria, but the former showed sharper and larger CIDs than the latter (Fig.2a, b of *Heki and Ping*, 2005). They showed amplitude difference of a factor of ~2. Here I consider that factor 2 uncertainties always exist in amplitude of every CID example of Figure 4.10.

4.4.3. Earthquake magnitudes and CID amplitudes

The CID amplitudes were derived from time series shown in Figure 4.10 by the following procedure, (1) find the peak TEC value, (2) go back in time from the peak by 1.5minutes and read TEC values, (3) calculate the difference between the two TEC values. *Astafyeva et al.*(2013) compared “absolute” CID amplitudes among earthquakes. However, coseismic uplifts excite waves in neutral atmosphere, and it would be therefore more natural to normalize CID amplitudes with the electron densities in the F region. Because the electron

density at a particular height is not always available, I used vertical TEC as a factor to normalize CID amplitudes.

I obtained the background vertical TEC at the time and place where the CIDs were detected using Global Ionospheric Maps (GIM) (*Mannucci et al.*, 1998). In Figure 4.11I compare "relative" CID amplitudes, *i.e.* those normalized with the background vertical TEC. In Figure 4.10, CID of the 2012 North Sumatra aftershock (M_w8.2) show slightly larger amplitude than that of the 2010 Maule earthquake (M_w8.8). However, after normalization with background vertical TEC (51.4 TECU and 6.0 TECU, respectively), the relative amplitude of the latter exceeds the former. For latitude bands with insufficient ground station coverage, GIM sometimes gives unrealistic values. For example, the vertical TEC at the time of the 2009 July 15 New Zealand earthquake (9:22 UT) is ~1.4 TECU according to GIM, but I revised it to ~4.1 TECU by analyzing GPS data of the "west" station following *Astafyeva and Heki* (2011).

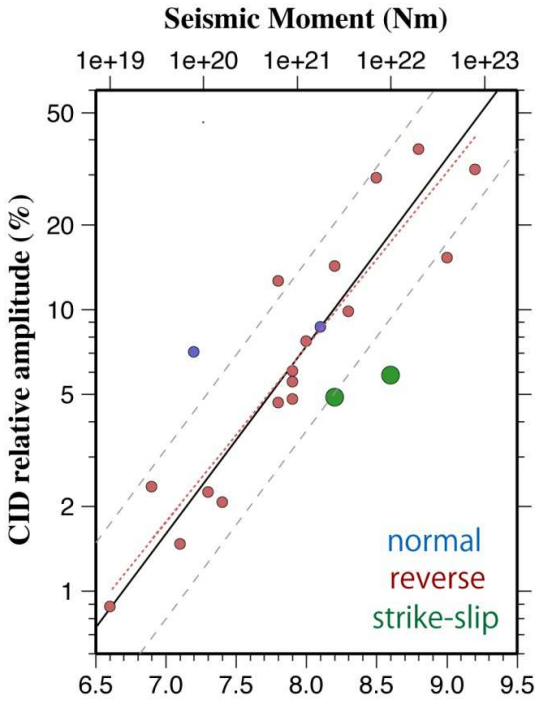


Figure 4.11. Comparison of moment magnitudes of the 21 earthquakes shown in Figs.8, 9, and the Wenchuan earthquake from *Astafyeva et al.*(2013), with their relative CID amplitudes. Colors of the symbols show the mechanisms. The black line indicates the best-fit

line with the fixed slope of 2/3, *i.e.* the difference in 3 of M_w corresponds to the two orders of difference in CID amplitudes. Dashed lines indicate uncertainties of factor two differences coming from non-ideal LOS geometry. The red dotted line indicates the best-fit line with both slope and offset inferred by linear regression for the 17 data of reverse earthquakes.CID amplitudes of strike-slip earthquakes (green) show somewhat smaller values than other earthquakes.

It would be reasonable to assume that the relative CID amplitude may scale with the coseismic crustal uplift of an earthquake. In Figure 4.12,I show that the uplift obeys different scaling laws with earthquake magnitudes for relatively large (M>7) and small (M<7) events. Because CIDs appear only after larger earthquakes, I considered CID amplitudes would obey the same scaling law as the large events, i.e. CID amplitudes increase by two orders of magnitude as M_w increases by three (*i.e.* the slope is 2/3). In Figure 4.11, where I used the logarithmic vertical axis, data are distributed roughly around a line with the slope of 2/3. I express the relationship between the moment magnitude and the relative CID amplitude (unit: percent) as follows,

$$\log_{10}(\text{CID amplitude}) = a\,(M_w - 8.0) + b. \qquad (4.1)$$

The offset *b* is the common logarithm of the relative CID amplitude in percent of an M_w 8 event. In the best-fit line inferred from reverse earthquakes (dotted line in Fig.4.11), the slope *a* was 0.621 with the 1σ uncertainty of 0.064, and *b* was estimated as 0.867 with the 1σ uncertainty of 0.045. Because the slope coincides with 2/3 within 1σ, I fixed *a* to 2/3 (solid line in Fig.10) and estimated *b* as 0.871 with the 1σ uncertainty of 0.044.

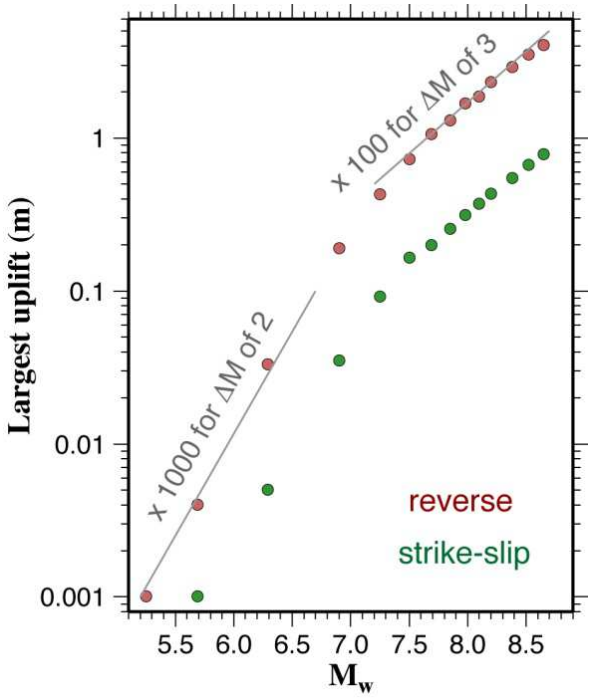


Figure 4.12. Relationship between maximum uplift and moment magnitude for shallow angle thrust (dip angle: 15 degrees, depth: 25 km, rigidity: 50 GPa) earthquakes (red circles). Length of the fault was assumed to be twice as long as width, and the dislocation was given to realize the constant stress drop (3 MPa). They seem to obey two different scaling laws for smaller and larger events. Green circles show those for strike-slip earthquakes (for larger earthquakes, upper edge of the fault was assumed to coincide with the surface).

As discussed in Section 4.5.2, I consider that observed CID amplitudes have factor 2 uncertainties, and I indicate it with two dashed lines. There are two data lying significantly beyond these lines, i.e. the 2012 Tohoku outer rise earthquake (M_w7.2) and the 2012 North Sumatra earthquake (M_w8.6). The former earthquake is composed of two events of comparable magnitude, a reverse faulting deep within the subducting oceanic plate and a shallow normal faulting near the surface. The former contributes little to the coseismic crustal movements, and the shallow epicentral depth of the latter (~6 km, and this is the shallowest in the 21 earthquakes studied here) might be responsible for the large CID.

The latter earthquake (the 2012 North Sumatra earthquake) negatively deviates from the general trend. Another strike-slip earthquake (the aftershock of the 2012 North Sumatra earthquake) also tends to be smaller than the general trend. These deviations are consistent with the smaller vertical crustal movements of strike-slip earthquakes than dip-slip events

(Fig. 4.12). I would need more CID examples of strike-slip earthquakes to discuss statistical significance of their small CIDs. However, strike-slip earthquakes are scarcely large enough to disturb the ionosphere. In fact, the largest strike-slip event in Japan that occurred after the deployment of the dense GPS network is the 1995 January Southern Hyogo Prefecture (Kobe) earthquake (M_w6.9), for which I could not detect CID.

If I could measure the CID amplitude with factor-two uncertainty, the inferred relationship in Figure 10 suggests that I could determine M_w with an uncertainty of ±0.45 about ten minutes after the earthquake. This is useful for early warning in a region where tsunamis arrive at the coast later than acoustic waves arrive at the ionospheric F region, and this is the case for the Pacific coast of NE Japan.

Areal extent of strong CID appearance would be another measure to infer M_w, and this is one of the future issues to be studied. No systematic dependence of CID amplitudes on the focal depth was seen (except the large CID amplitude for the shallowest event). The 2006 May Tonga (~55 km) and the 2013 September Tokachi-oki (~45 km) earthquakes have the deepest epicenters, but their CIDs do not show significant negative deviations from the rest. Depths to the center of the fault might better correlate with CID amplitudes. The correlation between the CID amplitudes and maximum coseismic vertical crustal movements (available in Table 4.1) was less clear than in Figure 10. Other quantities, *e.g.* vertical movements integrated two-dimensionally over the surface, might show clearer correlation.

Table 4.1 Twenty-one earthquakes with clear CIDs discussed in the research.

Year/Month/Day	Earthquake	Mw	Time	--- epicenter --- Long.	Lat.	--- SIP --- Long.	Lat.	CID	Sat.	Stn.	GIM-VTEC	D1	D2	Maximum depth	uplift	Mechanism
			(UT,hour)	(oE)	(oN)	(oE)	(oN)	(TECU)			(TECU)	(km)	(km)	(km)	(m)	
2004/12/26	Sumatra-Andaman	9.2	1.25	95.854	3.316	95.412	9.372	6.59	13	samp	20.95	320	671	30	3.4	R
2011/03/11	Tohoku-oki	9.0	5.90	142.372	38.297	141.868	37.378	4.22	26	0048	27.67	452	111	24	5.0	R
2010/02/27	Maule	8.8	6.80	-72.733	-35.909	-72.268	-31.488	2.24	23	cnba	6.04	514	492	35	3.0	S
2012/04/11	North Sumatra	8.6	8.80	93.063	2.311	93.475	7.185	2.62	3	pbri	44.94	1031	541	22.9	2.1	R
2007/09/12	Sumatra Bengkulu	8.5	11.40	101.374	-4.520	100.122	-0.716	6.15	25	samp	20.99	947	443	34	1.3	R
1994/10/04	Hokkaido-toho-oki	8.3	13.50	147.321	43.773	143.325	39.881	0.68	20	0036	6.89*	770	545	24	2.0	R
2006/11/15	Central Kuril	8.2	11.40	153.230	46.607	152.252	45.836	0.73	20	0519	5.16	716	114	30.3	1.0	R
2012/04/11	North Sumatra (after)	8.2	10.90	92.452	0.773	92.006	4.083	2.51	11	pbri	51.39	1200	369	16	1.2	N
2007/01/13	Central Kuril outer rise	8.1	4.60	154.455	46.272	153.830	44.411	0.63	1	0009	7.27	819	213	10	0.7	N
2003/09/25	Tokachi-oki	8.0	20.00	143.904	41.775	142.098	40.068	0.77	13	0323	9.99	1015	243	45	0.7	R
2007/09/13	Sumatra Bengkulu (after)	7.9	0.00	100.906	-2.506	100.010	-0.549	0.36	21	samp	7.56	720	238	10	0.6	R
2006/05/03	Tonga	7.9	15.44	-174.164	-20.130	-173.530	-16.716	0.35	14	fale	5.79	734	383	55	0.6	R
2008/05/12	Wenchuan	7.9	6.47	103.364	30.986	105**	30**	1.04	22	luzh	18.73	---	191	13	4.7	R
2012/10/28	Queen Charlotte Islands	7.8	3.24	-132.131	52.742	-130.777	52.076	0.16	32	will	8.72	678	118	17.5	2.3	R
2009/07/15	New Zealand	7.8	9.37	166.577	-45.750	166.000	-45.000	0.52	20	west	4.10***	751	94	12	1.5	R
2004/09/05	Kii-hanto-oki	7.4	15.12	136.608	33.062	133.736	28.377	0.30	11	0746	14.50	940	587	44	0.7	R
2011/03/09	Tohoku-oki (fore)	7.3	2.92	142.840	38.440	142.992	38.316	0.61	7	0047	27.18	517	19	8	0.8	R
2012/12/07	Tohoku outer rise	7.2	8.47	144.090	37.889	143.752	37.747	0.50	8	3030	7.13	451	34	6	0.3	N
2004/09/05	Kii-hanto-oki (fore)	7.1	10.20	136.608	33.062	134.503	31.533	0.29	15	0099	20.08	558	261	38	0.3	R
2008/06/13	Iwate-Miyagi	6.9	23.90	140.678	39.122	140.598	38.554	0.23	8	0575	9.91	410	63	8	1.2	R
2007/07/16	Chuetsu-oki	6.6	1.40	138.469	37.576	138.399	36.703	0.12	26	0062	13.41	345	97	17	0.3	R

(fore): foreshock, (after): largest aftershock, Time: approximate time of the CID appearance.
D1:distance between epicenter and GPS station, D2:distance between epicenter and SIP.
Mechanisms are R (reverse), N (normal) or S (strike-slip).
Maximum uplift was calculated either using published fault parameters, or modeling fault parameters after Figure A2.
*GIM from the same day in 2005 (11 years after the earthquake), **approximate SIP coordinates from Afraimovich et al. [2010].
***calculated using data at "west"

4.4.5. Preseismic TEC Anomalies

Possible enhancement of TEC immediately before the 2011 Tohoku-oki earthquake (M_w9.0) above the rupture zone has been reported by *Heki* (2011). In Indonesia, *Cahyadi and Heki* (2013) reported the occurrence of similar TEC anomalies to the north of the epicenter immediately before the 2007 Bengkulu earthquake (M_w8.5). *Kamogawa and Kakinami* (2013) attributed the enhancement to an artifact falsely detected by the combined effect of the highly variable TEC under active geomagnetic condition and the tsunamigenic TEC drop ~10 minutes after the earthquake. In the rebuttal research, *Heki and Enomoto* (2013) examined the time series of vertical TEC and demonstrated that the TEC drop is not a stand-alone phenomenon, as claimed by *Kakinami et al.* (2012), but is a recovery from the enhancement (the underlying physics of the TEC drop was explained by a dynamic process associated with acoustic disturbance of the ionosphere by *Shinagawa et al.* (2013)). *Heki and Enomoto* (2013) suggested that similar TEC anomalies occurred before all the $M_w \geq 8.5$ earthquakes. Here I examine the case of the 2012 North Sumatra earthquake.

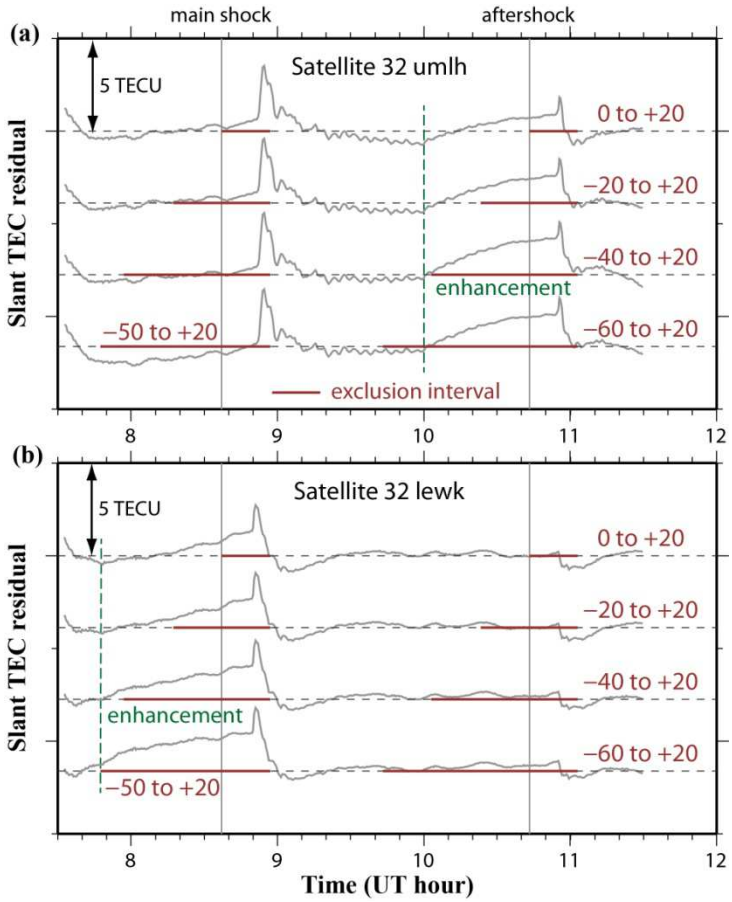


Figure 4.13. Slant TEC anomaly time series taken at the umlh (a) and lewk (b) stations with Satellites 32, the top two time series of Fig.4.2a. Vertical gray lines show the main shock and the largest aftershock of the 2012 North Sumatra earthquake. Reference smooth curves are derived by fitting cubic polynomials of time to vertical TEC changes, with four different exclusion intervals (indicated by horizontal red bars). The ending time of the interval was fixed to 20 minutes after the earthquake. Four starting times were compared, i.e. (1) the earthquake time (0 to +20, same as in Fig.4.2), (2) 20 minutes before the earthquake (-20 to +20), (3) 40 minutes before the earthquake (-40 to +20), and (4) 1 hour before the earthquake (-60 to +20). The case (4) is modified to -50 to +20 minutes for the main shock due to the availability of the data. The umlh and lewk stations show TEC enhancements starting ~40-50 minutes before the aftershockand the main shock (green dashed lines). Figure 4.14 are drawn assuming the case (3).

Reference curves used to plot the slant TEC residual time series in Figure 4.2 were obtained by modelling the change in vertical TEC with a cubic polynomial of time. In estimating such reference curves, we set up the “exclusion interval”, *i.e.*in Figure 4.2 we excluded the 20 minutes interval after the earthquake (0 to 20 minutes) as the part disturbed by CID. Preseismic TEC changes would emerge by moving the start of the exclusion interval

back in time. We performed a simple test in Figure 4.13to change the start of the exclusion interval. We pick up the top two time series in Figure 4.2a, *i.e.* the umlh and lewk stations and Satellite 32, and moved the original start time (the earthquake occurrence time) backward by 20, 40, and 60minutes(50 minutes for the main shock). The end of the exclusion interval is fixed to 20 minutes after the earthquake. As we make the start time earlier, preseismic positive anomalies starting 40-50 minutes before earthquakes emerge in the umlh (aftershock) and lewk (main shock) time series.

Based on the nominal excluding interval of -40 to +20 minutes, we plot map distributions of the anomalies (converted to vertical TEC) at three time epochs in Figure 12. Little anomalies are seen 1 hour before the earthquake (a, d). Positive anomalies are seen 20 minutes before the earthquake (b, e), and they become larger toward the earthquake occurrence time (c, f). The positive preseismic TEC anomalies appeared on the northern side of the epicenters over regions with diameter 100-200 km. This is very similar to the case of the 2007 Bengkulu earthquake (*Cahyadi and Heki*, 2013). The stations umlh and lewk did not show preseismic anomalies before the main shock and the largest aftershock in Figure 11, respectively. This is simply because the SIPs of these stations were outside these regions (their SIPs are marked with black outlines in Fig.4.14).

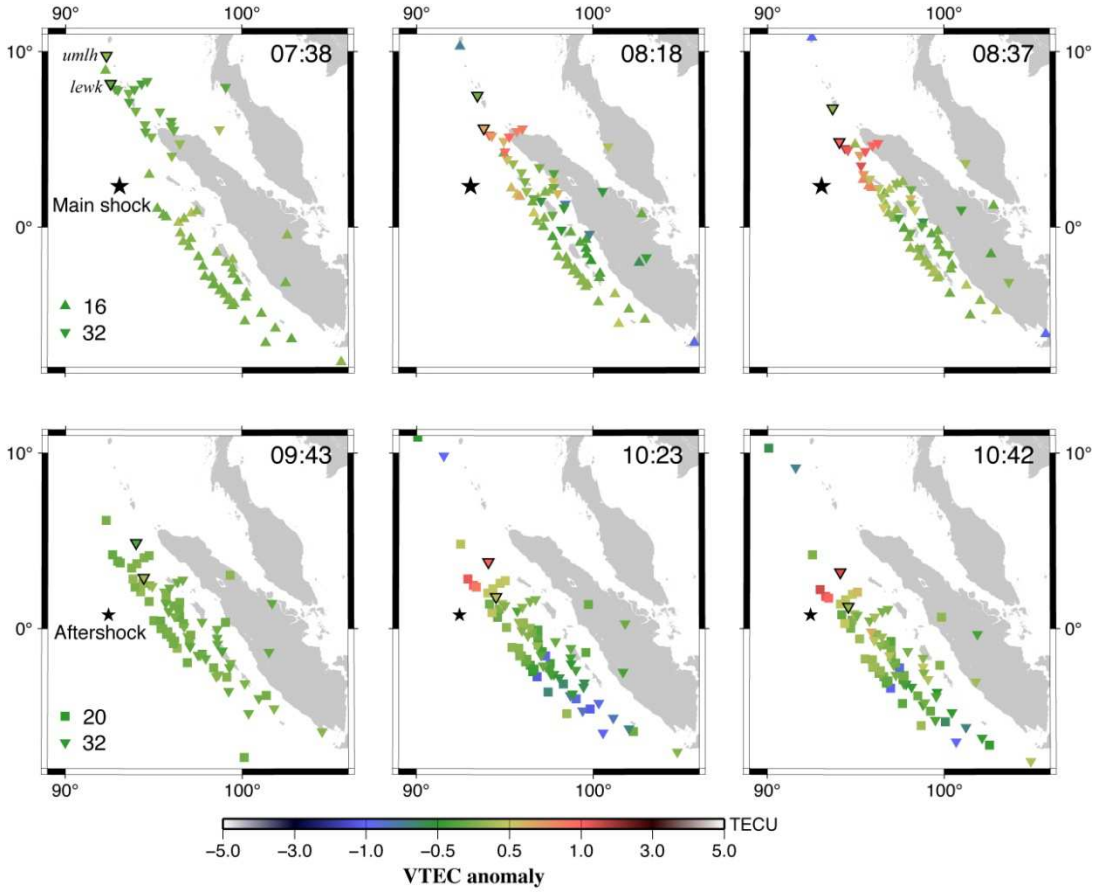


Figure 4.14. Vertical TEC anomalies at three time epochs, i.e. 1 hour (a, d), 20 minutes (b, e), and 1 minute (c,f) before the main shock and the largest aftershock of the 2012 North Sumatra observed at GPS stations with satellites 32 and 16 (a-c), and 20 and 32 (d-f). Satellite 32 SIPs for stations umlh and lewk, used in Fig.4.13, are emphasized with black outlines. TEC anomalies were first calculated as deviations from reference curves (vertical TEC changing as a cubic polynomial of time) and converted to vertical TEC by multiplying with the cosine of the zenith angle of LOS at the height of 300 km.

As discussed in *Heki and Enomoto* (2013), space weather influences may have accidentally caused such anomalies. In Figure 4.15we show B_z, Dst, and K_p over one-month period including the earthquake. The geomagnetic activity on 11 April, 2012 was moderately disturbed, and so we cannot rule out such a possibility. However, all of the M>8.5 earthquakes in this century (2004 Sumatra, 2007 Bengkulu, 2010 Maule, 2011 Tohoku, and 2012 North Sumatra) showed similar preseismic signatures (*Heki and Enomoto*, 2013), and it would be difficult to consider all of those as fortuitous coincidences.

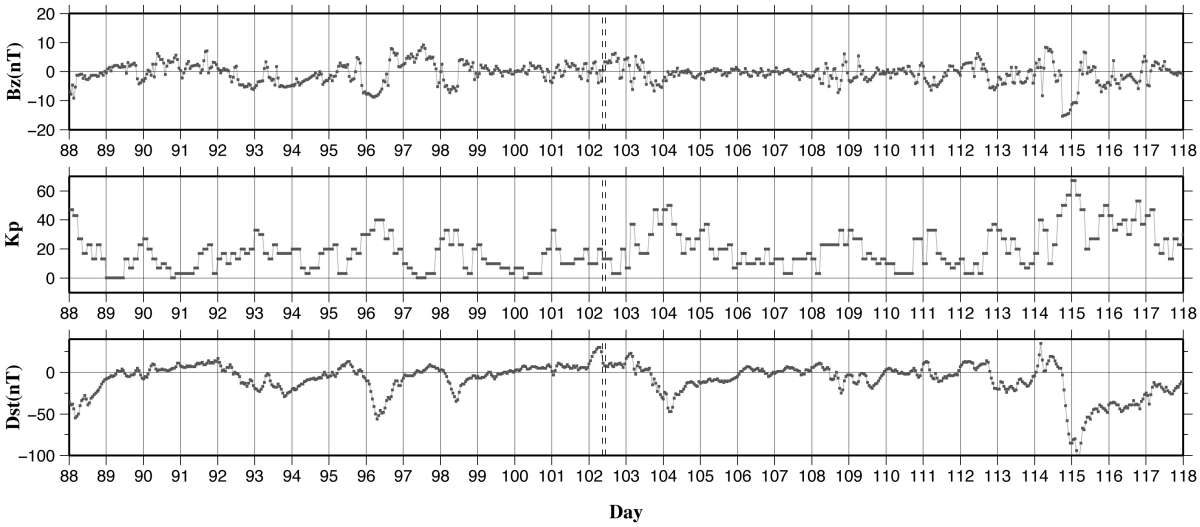


Figure 4.15. Space weather data, i.e. B_z (north-south component of the inter-planetary magnetic field), K_p index, and the Dst index, over one month time windows including the 2012 North Sumatra earthquakes (day 102, vertical dashed lines). Data are taken from NASA omniweb (omniweb.gsfc.nasa.gov).

Chapter 5

Recommendation and Conclusion

5.1 Conclusions

Seismic wave propagate upward in the atmosphere and reach the ionospheric F layer. Then the electron density structure there will be disturbed, which can be observed with GNSS as CID. Such atmospheric waves are classified into three, direct acoustic wave excited by coseismic vertical crustal movements, secondary acoustic wave excited by the propagation of the Raleigh surface wave, and internal gravity wave. My research focused on the first category, for two Indonesian megathrust earthquakes, namely the Bengkulu 2007 and Nias 2005 earthquakes. In addition, I studied two large strike-slip earthquakes that occurred off the North Sumatra in 2012. Comparison between moment magnitudes and amplitudes of CID was performed in order to obtain the relationship between the two quantities. The studies conducted here are summarized as follows;

5.1.1 Ionospheric disturbances of the 2007 Bengkulu and the 2005 Nias earthquakes, Sumatra, observed with a regional GPS network

This research in Chapter 3 provides the first comprehensive study of multiple aspects of CID and preseismic (both long- and short-term) ionospheric anomalies for two recent mega-thrust earthquakes in Indonesia. The studied aspects of CID include propagation speed (the observed velocity suggested its acoustic wave origin), azimuthal asymmetry of propagation, atmospheric resonance, polarity of the initial changes, and comparison of amplitudes between

the mainshock and the largest aftershock.

A clear CID was found in the 2007 Bengkulu earthquake. Its apparent velocity suggested an acoustic wave origin. The earthquake is followed by a large aftershock which occurred~12 hours later. This aftershock also showed CID signatures, and their smaller amplitudes can be explained by the difference in the earthquake magnitudes and the background TEC. These CID started with positive anomalies, similar to other reverse-fault earthquakes. The Rayleigh wave signatures were absent due possibly to the geometric alignment of the GPS network. The directivity (north-south asymmetry of propagation) of CID in the southern hemisphere was not clearly observed due to N-S asymmetry of the network. Resonant oscillations of the atmosphere with a frequency of ~5 mHz were found to follow the CID and last for half an hour.

Short-term preseismic TEC changes similar to the 2011 Tohoku-Oki earthquake were found in the 2007 Bengkulu earthquake. It was confirmed that geomagnetic activity was relatively quiet during the studied period. The behavior of TEC with the same satellite-station combination over 4 months suggests that the occurrences of similar anomalies are infrequent especially during geomagnetic quiescence. Hence it is not likely that space weather is responsible for the observed short-term preseismic TEC changes. This, together with other cases (*Heki,* 2011), suggests that the observed anomaly is relevant to the earthquake. The physical mechanism of the preseismic TEC changes remains unclear in spite of several new studies. Long-term TEC precursors were not found.

Plasma bubble occurred before and after the occurrence time of the 2005 Nias earthquake. Because their signatures were so strong, we could not even discuss the presence or absence of CID and preseismic TEC anomalies. Plasma bubbles were found on the previous and the next days, and are considered to be irrelevant to the earthquake occurrence.

5.1.2 Coseismic ionospheric disturbance of the 2012 North Sumatra earthquakes, large intra-plate strike-slip events

Here I summarize the research described in Chapter 4. There I studied the CIDs of the 2012 North Sumatra earthquake, the largest strike-slip earthquakes ever recorded, and its largest aftershock have been studied. Here I summarize the study as follows.

1) Acoustic wave origin CIDs were observed.
2) Monochromatic TEC oscillations of ~3.7 mHz followed the earthquake and lasted for an hour.
3) Strong northward directivity of the CID propagation was confirmed.
4) CID amplitudes of dip-slip earthquakes obeyed an empirical law such that the amplitude becomes 100 times as large for magnitude difference of three.
5) CID amplitudes of strike-slip earthquakes tend to negatively deviate from the law.
6) Preseismic TEC anomalies of ~1 TECU were found before the mainshock and the largest aftershock.

5.2 Recommendation: early warning system for earthquake and tsunami

In this last section, I summarize the disaster mitigation aspect of my study, and propose a few recommendations. First, I discuss the implication of the preseismic TEC anomalies. Among various earthquake precursor reported so far (*Rikitake*, 1976), electromagnetic phenomena has been the most widely explored e.g. underground electric currents (*Uyeda and Kamogawa*, 2008), propagation anomaly of VLF (*Molchanov and Hayakawa*,1998) and VHF (*Moriya et al.*, 2010), radio waves observation from asatellite (*Němecet al.*, 2008). It has been suggested that many electromagnetic earthquake precursors could be explained with positively charged aerosols (*Tributsch*, 1978).

Heki (2011), *Cahyadi and Heki* (2013), and this PhD thesis used another approach using

GPS-TEC. This approach is applicable for earthquakes with$M_w$of 8.2 or larger, for which TEC enhancementoccurimmediately (40-60 minutes prior to the event) before earthquakes. The method reveals strong temporal and spatial correlation with the earthquakes. This could offer a promising future technique for earthquake prediction after we successfully develop a sophisticated algorithm to discriminate preseismic and space-weather-origin TEC disturbances in real time.

Another approach to study preseismic TEC anomaly is to investigate the anomalous diurnal TEC change amplitudes. These anomalies are considered to occur a few days before earthquakes (*Liu et. al.*,2001; *Liu et al.*,2009).Unfortunately; we could not find such anomalies before the 2007 Bengkulu earthquake.

I also investigated the empirical relationship between CID amplitudes and M_w of earthquakes (*Cahyadi and Heki,GJI,under review*).This may also contribute to the tsunami disaster mitigation because it has a potential of knowing the earthquake $M_w$accurateto 0.45, say 10 – 15 minutes after the earthquake. This is useful for some regions including NE Japan, where tsunami takes 30–45 minutes to reach the Pacific coast. This approach is beneficial also for a part of Indonesia where the tsunami takes more time to reach shores than does the acoustic wave to reach the ionospheric F region.

Bibliography

Afraimovich, E. L., N. P. Perevalova, A. V. Plotnikov, and A. M. Uralov (2001), The shock-acoustic waves generated by earthquakes, *Ann. Geophys.,19*, 395–409.

Afraimovich, E. L., D. Feng, V. V. Kiryushkin, and E. I. Astafyeva (2010), Near-field TEC response to the main shock of the 2008 Wenchuan earthquake, *Earth Planets Space, 62*, 899-904.

Astafyeva, E. and K. Heki (2009), Dependence of waveform of near-field coseismic ionospheric disturbances on focal mechanisms, *Earth Planets Space, 61*, 939-943.

Astafyeva, E. and K. Heki (2011), Vertical TEC over seismically active region during low solar activity, *J. Atm. Terr. Phys., 73*, 1643-1652.

Astafyeva, E., K. Heki, V. Kiryushkin, E. Afraimovich, S. Shalimov (2009), Two-mode long-distance propagation of coseismic ionosphere disturbances, *J. Geophys. Res., 114*, A10307, doi:10.1029/2008JA013853.

Astafyeva, E., P. Lognonné, and L. Rolland (2011), First ionosphere images for the seismic slip of the Tohoku-oki Earthquake, *Geophys. Res. Lett.,38*, L22104, doi:10.1029/2011GL049623.

Astafyeva, E., S.Shalimov, E. Olshanskaya,and P. Lognonné (2013), Ionospheric response to earthquakes of different magnitudes: Larger quakes perturb the ionosphere stronger and longer, *Geophys. Res. Lett., 40*, 1675–1681, doi:10.1002/grl.50398.

Banerjee, P., F. F. Pollitz, and R. Bürgmann (2005), The size and duration of the Sumatra-Andaman Earthquake from far-field static offsets, *Science, 308*, 1769–1772.

Briggs, R. W. et al. (2006), Deformation and slip along the Sunda Megathrust in the great

2005 Nias-Simeulue earthquake, S*cience*, *311*, 1897–1901,doi:10.1126/science.1122602.

Cahyadi, M. N. and K. Heki (2013). Ionospheric disturbances of the 2007 Bengkulu and the 2005 Nias earthquakes, Sumatra, observed with a regional GPS network. *J. Geophys. Res.*, *118*, 1-11, doi:10.1002/jgra.50208.

Calais, E. and J. B. Minster (1995), GPS detection of ionospheric perturbations following the January 17, 1994, Northridge earthquake, *Geophys. Res. Lett.*, *22*, 1045–1048, doi:10.1029/95GL00168.

Choosakul, N., A. Saito, Iyemori, T, and M. Hashizume (2009), Excitation of 4-min periodic ionospheric variations following the great Sumatra-Andaman earthquake in 2004, *J. Geophys. Res.*, *114*, A10313, doi:10.1029/2008JA013915.

Chu, F. D., J.-Y. Liu, H. Takahashi, J. H. A. Sobral, M. J. Taylor, *and* A. F. Medeiros *(*2005*),* The climatology of ionospheric plasma bubbles and irregularities over Brazil, Ann. Geophys, 23, 379–384.

Dautermann, T., E. Calais, J. Haase, and J. Garrison (2007), Investigation of ionospheric electron content variations before earthquakes in southern California, 2003-2004, *J. Geophys. Res.*, *112*, B02106, doi:10.1029/2006JB004447.

Enomoto, Y. (2012), Coupled interaction of earthquake nucleation with deep Earth gases: A possible mechanism for seismo-electromagnetic phenomena, *Geophys. J. Int.*, 191, 1210-1214.

Freund, F. (2000), Time-resolved study of charge generation and propagation in igneous rocks, *J. Geophys. Res.*, *105*, 11001-11020, doi:10.1029/1999JB900423.

Gusman, A. R., Y. Tanioka, T. Kobayashi, H. Latief, and W. Pandoe (2010), Slip distribution of the 2007 Bengkulu earthquake inferred from tsunami waveforms and InSAR data, *J. Geophys. Res.*, *115*, B12316, doi:10.1029/2010JB007565.

Heki, K. and J.-S. Ping (2005), Directivity and apparent velocity of the coseismic ionospheric

disturbances observed with a dense GPS array, *Earth Planet. Sci. Lett., 236*, 845–855.

Heki, K., Y. Otsuka, N. Choosakul, N. Hemmakorn, T. Komolmis, and T. Maruyama (2006), Detection of ruptures of Andaman fault segments in the 2004 great Sumatra earthquake with coseismic ionospheric disturbances, *J. Geophys. Res., 111*, B09313, doi:10.1029/2005JB004202.

Heki, K. (2011), Ionospheric electron enhancement preceding the 2011 Tohoku-Oki earthquake, *Geophys. Res. Lett. 38*, L17312, doi:10.1029/2011GL047908.

Heki, K. and Y. Enomoto (2013), Preseismic ionospheric electron enhancements revisited, *J. Geophys. Res., 118*, 1-9, doi:10.1002/jgra.50578.

IAGA (International Association of Geomagnetism and Aeronomy), Working Group V-MOD (2010), International Geomagentic Reference Field: the eleventh generation, *Geophys. J. Int., 183*, 1216-1230, doi: 10.1111/j.1365-246X.2010.04804.x.

Kakinami, Y., M. Kamogawa, Y. Tanioka, S. Watanabe, A.R. Gusman, J.-Y.Liu, Y. Watanabe, and T. Mogi (2012), Tsunamigenic ionospheric hole, *Geophys. Res. Lett. 39*, L00G27, doi:10.1029/2011GL050159.

Kamogawa, M. and Y. Kakinami (2013), Is an ionospheric electron enhancement preceding the 2011 Tohoku-oki earthquake a precursor?,*J. Geophys. Res., 118*, 1-4, doi:10.1002/jgra.50118.

Kil, H., L. J. Paxton, K.-H. Kim, S. Park, Y. Zhang, and S.J. Oh (2011), Temporal and spatial components in the storm time ionospheric disturbances, *J. Geophys. Res., 116*, A11315, doi:10.1029/2011JA016750.

Kuo, C. L., J.D.Huba, G. Joyce, and L. C. Lee (2011), Ionosphere plasma bubbles and density variation induced by pre-earthquake rock currents and associated surface charges, *J. Geophys. Res., 116*, A10317, doi:10.1029/2011JA016628.

Le, H., J.-Y. Liu, and L. Liu (2011), A statistical analysis of ionospheric anomalies before 736

M6.0+ earthquakes during 2002-2010, *J. Geophys. Res., 116*, A02303, doi:10.1029/2010JA015781.

Li, G., B. Ning, L. Liu, W. Wan, *and* J.-Y. Liu *(*2009*),* Effect of magnetic activity on plasma bubbles over equatorial and low-latitude regions in East Asia, Ann. Geophys., 27, 303–312.

Liu, J.-Y., Y.I. Chen, Y. J. Chuo, and H.F. Tsai (2001), Variations of ionospheric total electron content during the Chi-chi earthquake, *Geophys. Res. Lett., 28*, 1383-1386.

Liu, J. Y. et al. (2009), Seismoionospheric GPS total electron content anomalies observed before the 12 May 2008 Mw7.9 Wenchuan earthquake, *J. Geophys. Res., 114*, A04320, doi:10.1029/2008JA013698.

Mannucci, A. J., B. D. Wilson, D. N. Yuan, C. H. Ho, U. J. Lindqwister, and T. F. Runge (1998), A global mapping technique for GPS-derived ionospheric total electron content measurements, *Radio Sci., 33*, 565–582, doi:10.1029/97RS02707.

Meng, L., J.-P.Ampuero, J. Stock, Z. Duputel, Y. Luo, and V.C. Tsai(2012), Earthquake in a maze: Compressional rupture branching during the 2012 M_w 8.6 Sumatra Earthquake, *Science, 337*, 724-726.

Migoya-Orué, O.Y., S. M. Radicella, P. Coïsson (2009), Low latitude ionospheric effects of major geomagnetic storms observed using TOPEX TEC data, *Ann. Geophys., 27*, 3133–3139.

Mitsui, Y.& Heki, K., 2013.Scaling of early afterslip velocity and possible detectionof tsunami-induced subsidence by GPS measurements immediatelyafter the 2011 Tohoku-Oki earthquake, *Geophys. J. Int.*, 195, 238-248.

Molchanov, O. A. and M. Hayakawa (1998), VLF signal perturbations possibly related to earthquakes, *J. Geophys. Res., 103*, 17,489–17,504,doi:10.1029/98JA00999.

Němec, F., O. Santolík, M. Parrot, and J. J. Berthelier (2008), Spacecraft observations of

electromagnetic perturbations connected with seismic activity, *Geophys. Res. Lett., 35*, L05109, doi:10.1029/2007GL032517

Ngwira, C. M., L.-A.McKinnell, P. J. Cilliers, and A. J. Coster(2012), Ionospheric observations during the geomagnetic storm events on 24–27 July 2004: Long-duration positive storm effects, *J. Geophys. Res.,117,*A00L02,doi:10.1029/2011JA016990.

Nishida, K., N. Kobayashi, and Y. Fukao (2000), Resonant oscillation between the solid earth and the atmosphere, *Science, 287*, 2244-2246.

Nishioka, M., A. Saito, and T. Tsugawa(2007), Occurrence characteristics of plasma bubble derived from global ground-based GPS receiver networks, *J. Geophys. Res., 113*, A05301,doi:10.1029/2007JA012605.

Oh, S. Y., and Y. Yi (2011), Solar magnetic polarity dependency of geomagnetic storm seasonal occurrence, *J. Geophys. Res., 116,* A06101, doi:10.1029/2010JA016362.

Okada, Y. (1992), Internal deformation due to shear and tensile faults in a half-space, *Bull. Seismol. Soc. Am., 82*, 1018-1040.

Ozeki, M. and K. Heki (2010), Ionospheric holes made by ballistic missiles from North Korea detected with a Japanese dense GPS array, *J. Geophys. Res., 115*, A09314, doi:10.1029/2010JA015531.

Rikitake, T. (1976), Earthquake Prediction, Elsevier, Amsterdam, pp. 357.

Rolland, L. M., P. Lognonné, and H. Munekane (2011a), Detection and modeling of Rayleigh wave induced patterns in ionosphere, *J. Geophys. Res., 116,* A05320, doi:10.1029/2010JA016060.

Rolland, L.M., P. Lognonné, E. Astafyeva, E. A. Kherani, N. Kobayashi, M. Mann, and H. Munekane (2011b), The resonant response of the ionosphere imaged after the 2011 off the Pacific coast of Tohoku earthquake, *Earth Planets Space, 63*, 853-857.

Rolland, L. M., M. Vergnolle, J.-M.Nocquet, A. Sladen, J.-X.Dessa, F. Tavakoli, H. R.

Nankali, and F. Cappa (2013), Discriminating the tectonic and non-tectonic contributions in the ionospheric signature of the 2011, M_w7.1, dip-slip Van earthquake, Eastern Turkey, *Geophys. Res. Lett., 40*, 2518–2522, doi:10.1002/grl.50544.

Saito, A. et al. (2011), Acoustic resonance and plasma depletion detected by GPS total electron content observation after the 2011 off the Pacific coast of Tohoku Earthquake, *Earth Planets Space, 63*, 863–867.

Sardón, E., A. Rius, and N. Zarraoa (1994), Estimation of the transmitter and receiver differential biases and the ionospheric total electron content from global positioning system observation, *Radio Sci., 29*, 577–586.

Shinagawa, H., T. Tsugawa, M. Matsumura, T. Iyemori, A. Saito, T. Maruyama, H. Jin, M. Nishioka, and Y. Otsuka (2013), Two-dimensional simulation of ionospheric variation in the vicinity of the epicenter of the Tohoku-oki earthquake on 11 March 2011, *Geophys. Res. Lett., 40*, 5009-5013, doi:10.1002/2013GL057627.

Simons, W. J. et al. (2007), A decade of GPS in Southeast Asia: Resolving Sundaland motion and boundaries, *J. Geophys. Res., 112*, B06420, doi:10.1029/2005JB003868.

Tributch, H (1978) : Do aerosol anomalies precede earthquakes?, Nature, vol.276, pp.606-608.

Tsugawa, T, A. Saito, Y. Otsuka, M. Nishioka, T. Maruyama, H. Kato, T. Nagatsuma, and K.T. Murata (2011), Ionospheric disturbances detected by GPS total electron content observation after the 2011 off-the-Pacifc coast of Tohoku Earthquake, *Earth Planets Space, 63*, 875-879.

Uyeda, S. and M. Kamogawa (2008), The prediction on two large earthquakes in Greece, E*os Trans. AGU, 89*(39), doi:10.1029/2008EO390002.

Yao, Y.B., P. Chen, S. Zhang, J.J. Chen, F. Yan, and W.F. Peng (2012), Analysis of pre-earthquake ionospheric anomalies before the global M=7.0+ earthquakes in 2010, *Nat.*

Hazards Earth Syst. Sci., *12*, 575-585.

Yue, H., T. Lay, and K. D. Koper (2012), En échelon and orthogonal fault ruptures of the 11 April 2012 great intraplate earthquakes, *Nature*, *490*, 245-249.